# Design and Analysis of a Stage-Based Electrospray Propulsion System for CubeSats

by

Oliver Jia-Richards

S.B., Massachusetts Institute of Technology (2018)

Submitted to the Department of Aeronautics and Astronautics
in partial fulfillment of the requirements for the degree of

Master of Science in Aeronautics and Astronautics

at the

MASSACHUSETTS INSTITUTE OF TECHNOLOGY

June 2019



Author .....
Department of Aeronautics and Astronautics
May 20, 2019

Certified by .....
Paulo Lozano
M. Alemán-Velasco Professor of Aeronautics and Astronautics
Thesis Supervisor

Accepted by .....
Sertac Karaman
Associate Professor of Aeronautics and Astonautics
Chair, Graduate Program Committee

# Design and Analysis of a Stage-Based Electrospray Propulsion System for CubeSats

by

Oliver Jia-Richards

Submitted to the Department of Aeronautics and Astronautics
on May 20, 2019, in partial fulfillment of the
requirements for the degree of
Master of Science in Aeronautics and Astronautics

## Abstract

The standardization of small spacecraft through CubeSats has allowed for more affordable space exploration. This progress in affordability has been limited to Earth orbit due in part to the lack of high $\Delta$V propulsion systems that are compatible with the small form factor. The ion Electrospray Propulsion System developed at the Space Propulsion Laboratory at the Massachusetts Institute of Technology is a promising technology foundation for a compact, high $\Delta$V propulsion system. However, the $\Delta$V output of the propulsion system is limited by the lifetime of individual electrospray thrusters. This thesis presents the design and analysis of a stage-based concept for the ion Electrospray Propulsion System where the propulsion system is composed of a stack of electrospray thruster arrays.

The stage-based propulsion system bypasses the lifetime limit of individual electrospray thrusters in order to increase the lifetime of the entire propulsion system. In effect, propulsion capabilities for CubeSats can be advanced without the need for technological developments. With the current performance metrics of the ion Electrospray Propulsion System, deep-space missions with an initial spacecraft form factor of a 3U CubeSat are feasible with current propulsion technology. Mechanisms required for the stage-based system are designed and demonstrated in a vacuum environment. In addition, analytical methodologies for the analysis of stage-based propulsion systems are developed to assist in preliminary mission design as well as provide the framework for autonomous decision making. Finally, applications of a stage-based propulsion system for missions to near-Earth asteroids are explored as well as analytical guidance for the escape trajectory.

Thesis Supervisor: Paulo Lozano
Title: M. Alemán-Velasco Professor of Aeronautics and Astronautics

# Acknowledgments

Thank you to everyone who has supported me throughout this work. In particular, thank you Paulo for providing me ample opportunity and guidance to develop as an aerospace engineer and trusting me enough to let me work in the Space Propulsion Lab, first as an undergraduate researcher and now as a graduate student. Thank you as well to Emma for always being by my side whether it be writing this thesis, traveling, or watching the Leafs. You have, without a doubt, made my life better and more enjoyable.

Funding for this research was provided by the NASA Space Technology Mission Directorate through the Small Spacecraft Technology Program under grant 80NSSC18M0045 and through a NASA Space Technology Research Fellowship under grant 80NSSC18K1186.

# Contents

# List of Figures

# List of Tables

# Chapter 1

# Introduction

The standardization of small spacecraft through CubeSats has allowed for more affordable space exploration. However, this progress in affordability has often been limited to Earth orbit, with the recent launch of Mars Cube One [1] representing the first deep-space mission performed with CubeSats. There are several other missions that could take advantage of the CubeSat form factor. In particular, missions to near-Earth asteroids lend themselves to the use of CubeSats. Our current understanding of these asteroids in terms of composition and characteristics is limited and the paradigm of using a single large spacecraft restricts the number of visits to once every few years. By using fleets of CubeSats, all of which could be launched on the same launch vehicle, the frequency of asteroid visits could be dramatically increased all while significantly decreasing the cost per visit.

However, there are a number of technical challenges that are preventing such missions from being performed including the miniaturization of hardware, autonomy, and guidance, navigation, and controls systems. This work aims towards an independent deep-space CubeSat mission from the propulsion standpoint. Specifically, given the current propulsion technology available, can a propulsion system compatible with the CubeSat form factor be developed that can propel CubeSats from Earth orbit into deep-space and to a near-Earth asteroid?

As will be covered in Section 4.1, a mission to a near-Earth asteroid from geostationary orbit around Earth will require at least 3 km/s of $\Delta$V when accounting

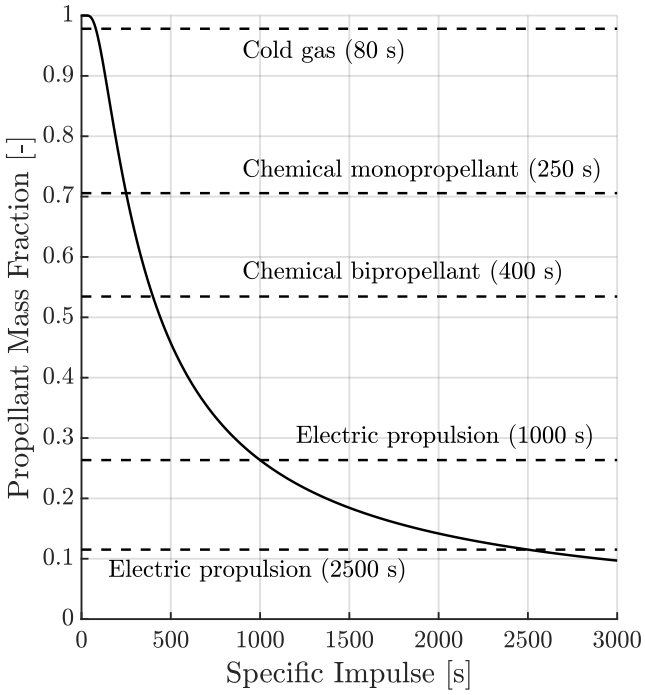


Figure 1-1: Propellant mass fraction for 3 km/s $\Delta$V mission

for low-thrust losses. Figure 1-1 shows the propellant mass fraction for a 3 km/s $\Delta$V mission for various specific impulses with typical specific impulses for different propulsion systems marked. Cold gas and chemical monopropellant based propulsion systems are clearly prohibitive for such a mission even if the low-thrust losses were removed. Chemical bipropellant propulsion systems require a fuel mass fraction of 0.53. This is not necessarily a prohibitively high propellant mass fraction given a sufficiently large spacecraft. However, for a 3U CubeSat which has a baseline wet mass of 4 kg, this leaves only 1.88 kg of mass to fit all other aspects of the spacecraft including the nozzle, fuel tanks, and propellant management systems for the propulsion system, likely preventing the mission from being feasible. Therefore, a CubeSat compatible propulsion system capable of producing 3 km/s of $\Delta$V will have to be based in electric propulsion technology.

Within electric propulsion, electrospray propulsion holds many advantages that help to reduce the dry mass and volume of the system. Figure 1-2 shows the $\Delta$V capabilities of various 3U CubeSat compatible propulsion systems versus their wet

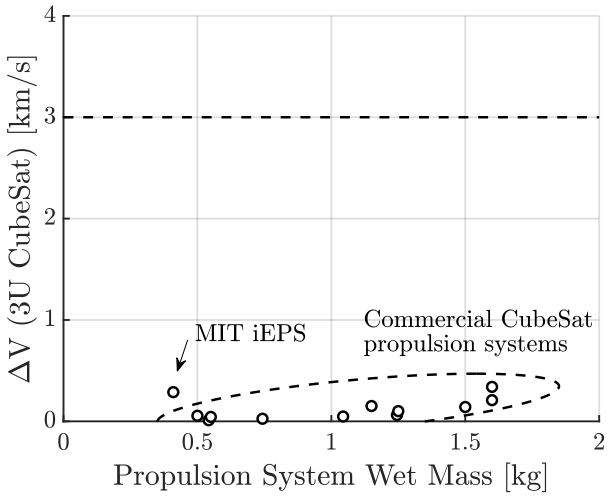


Figure 1-2: Comparison of ΔV versus wet mass for 3U CubeSat propulsion systems

mass. We can see that all systems fall woefully short of the 3 km/s ΔV requirement with the best system producing 340 m/s of ΔV.

Separate from commercial options, the ion Electrospray Propulsion System (iEPS) developed in the Space Propulsion Laboratory at the Massachusetts Institute of Technology produces relatively high ΔV (second highest of the propulsion systems surveyed) with the lowest wet mass. In addition the system occupies a relatively low volume, around 0.5U, for the thrusters, fuel tanks, and power processing unit. The low mass and volume of iEPS is a result of the underlying electrospray propulsion technology and ionic liquid propellant.

## 1.1 Overview of Electrospray Propulsion

Electrospray thrusters produce thrust through electrostatic acceleration of ions. Ions are evaporated from an ionic liquid propellant by overcoming the surface tension of the liquid with an applied electric field. The ionic liquid propellant is a molten salt at room temperature that is non-reactive, readily available, and has low toxicity. Electrospray thrusters and their ionic liquid propellants hold three main advantages that make them an excellent choice for propulsion of small spacecraft such as CubeSats. Firstly, the ionic liquid is "pre-ionized" and does not need an ionization chamber.

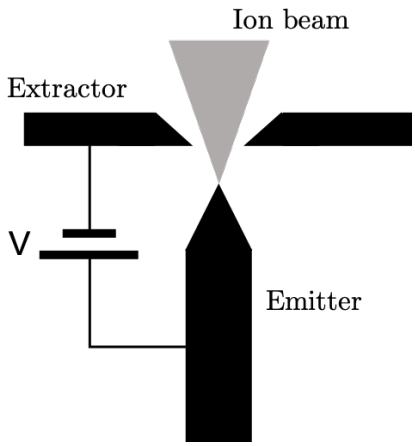


Figure 1-3: Diagram of electrospray emitter and extractor

Second, ionic liquids have near-zero vapor pressure due to the ionic bonds between molecules and therefore do not need any form of pressurized containment. Lastly, propellant is fed to the thruster by passive capillary forces through a porous liner embedded into the fuel tank thereby eliminating the need for any pumping systems. These three advantages allow electrospray thrusters to be incredibly compact and suitable for the CubeSat form factor.

To produce a strong enough electric field to evaporate the ions, the ionic liquid is fed to a sharp emitter tip. A voltage is applied to the ionic liquid with respect to an extractor grid. The sharp tip of the emitter allows for a strong electric field to develop that causes a liquid instability and the development of a sharp liquid meniscus that accentuates the electric field further to the point that ions can be evaporated from the liquid [2]. A diagram of a single emitter and extractor is shown in Figure 1-3. The thrust produced by a single emitter extractor pair is only on the order of 10s of nano-Newtons. Therefore, multiple emitters are arranged in an array to produce a single thruster. Since a single emitter is on the 100 $\mu$m scale, arrays of 100s of emitters can be manufactured on a 1 cm scale.

In addition to the inherent advantages of ionic liquid propellants, the operation of electrospray thrusters can also reduce mass and complexity relative to other propulsion systems. Since the ionic liquid is composed of both positively and negatively charged ions, by changing the polarity of the voltage applied between the emitter

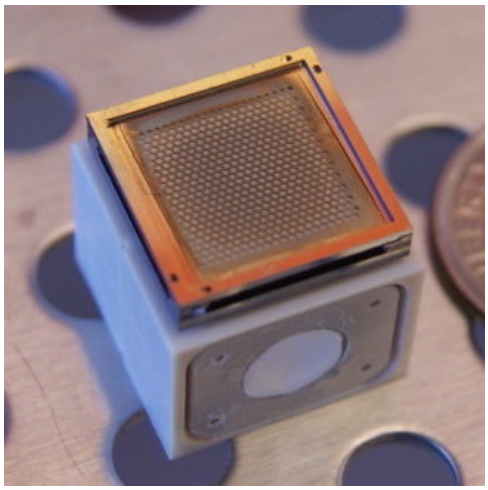

Figure 1-4: iEPS thruster mounted on a single thruster fuel tank

tip and extractor, the thruster will either evaporate and accelerate negative ions or positive ions. To prevent spacecraft charging, thrusters are operated in pairs with one thruster firing positive ions and the other thruster firing negative ions. This paired operation eliminates the need for a neutralizer further reducing the mass and size of the propulsion system.

### 1.1.1 ion Electrospray Propulsion System

For this work we will consider the ion Electrospray Propulsion System (iEPS) under development in the Space Propulsion Laboratory (SPL) at the Massachusetts Institute of Technology. Each iEPS thruster consists of an array of 480 emitter tips made from porous glass. The emitter array is housed in a 13 x 12 x 2.4 mm silicon frame with a gold coated silicon extractor grid. Figure 1-4 shows an iEPS thruster mounted on a single thruster fuel tank. Due to the passive propellant feed system, the same iEPS thruster can be mounted on a variety of fuel tanks as long as a porous material connection exists between the ionic liquid and emitter array. Figure 1-5 shows a scaled up configuration where four iEPS thrusters are mounted on the same fuel tank thereby maximizing the density of emitter tips while maintaining structural integrity during launch from Earth.

Each iEPS thruster can produce thrust in the range of 2 - 20 $\mu$N with a specific

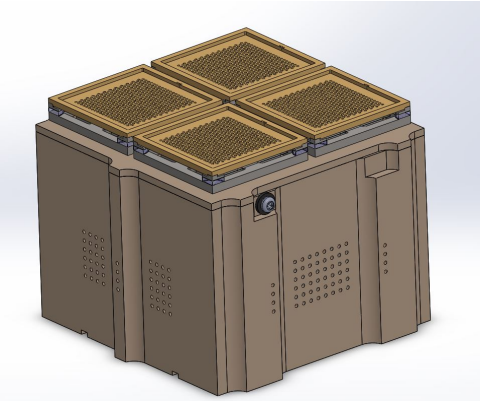

Figure 1-5: Four iEPS thrusters mounted on the same fuel tank

Table 1.1: Performance regimes of iEPS thrusters

| | Minimum | Target |
|---|---|---|
| Max thrust | 20 $\mu$N | 80 $\mu$N |
| Specific impulse | 1000 s | 2500 s |
| Lifetime | 500 hr | 1000 hr |

impulse close to 1000s when using EMI-$BF_4$ as the ionic liquid propellant [3]. However, the thrust and specific impulse are heavily dependent on the ionic liquid used as well as the material of the emitter array. Ongoing research at the SPL is investigating different materials for the emitter array that can contribute to an increased thrust, specific impulse, and thruster lifetime [4]. Two regimes of thruster performance are considered throughout this work. The first represents the current demonstrated performance which is the minimum expected performance of the thrusters during implementation. The second represents the target performance which is based on expected near term developments. The performance metrics for both the minimum and target performance regimes are summarized in Table 1.1.

A single iEPS thruster on its own does not produce enough thrust to be useful for main propulsion of a CubeSat mission. While the low thrust has other applications, such as for high precision attitude control [5], for main propulsion the thrust is increased by using arrays of thrusters. Tanks with four thrusters each, as shown in Figure 1-5, are arranged on a 1U CubeSat face. A 1U CubeSat face can hold up to nine of these clusters in a 3 x 3 square pattern for a total of 36 thrusters. For this

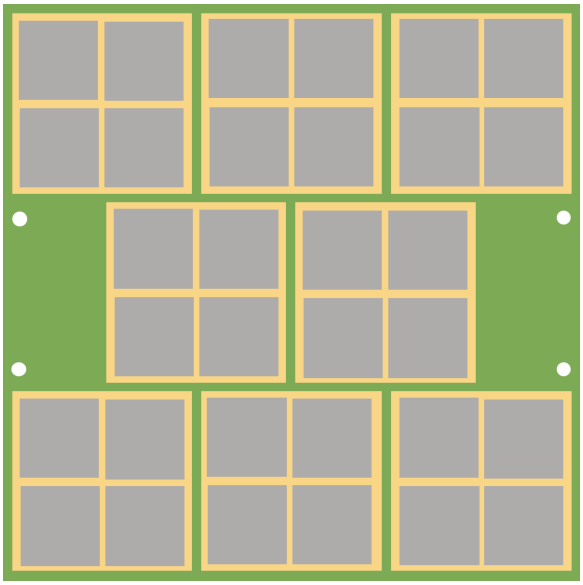

Figure 1-6: Configuration of iEPS thrusters on a 3U CubeSat compatible stage.

work, we will consider a configuration where a thruster in the center row is omitted to provide space for the staging electronics, which will be introduced in Section 1.2, and mounting on either side of the thrusters as shown in Figure 1-6.

This configuration, with 32 thrusters, can produce 0.64 mN of thrust in the minimum performance case and 2.56 mN of thrust in the target performance case. While this thrust is still relatively small, the low mass of the CubeSat form factor means that the net acceleration is comparable to that of other electric propulsion based missions such as Dawn [6].

### 1.1.2 Lifetime Limitations of Electrospray Thrusters

While electrospray thrusters are highly compatible with the CubeSat form factor due to their mechanical simplicity and small size, the $\Delta V$ that can be produced by an electrospray thruster based system is limited by the operational lifetime of the thrusters themselves. The primary life-limiting mechanism for electrospray thrusters is accumulation of propellant on the extractor grid [7]. The beam of ions which is extracted from the emitter tip leaves in a conical shape with observed half-angles of 60 degrees [3]. The beam can therefore impact the extractor grid and allow propellant to

accumulate or backspray onto the emitter array. Misalignments between the emitter tips and extractor grid during thruster manufacturing can accentuate the impingment of the ion beam onto the extractor grid and increase the rate at which propellant accumulates. If enough propellant accumulates, an ionic liquid connection can be formed between the emitter and extractor causing an electrical short and rendering the thruster inoperable. It is believed that propellant accumulation caused an electrical short of one of the electrospray thrusters on the ESA LISA Pathfinder mission [8].

While ion beam impingement with the extractor grid is the primary lifetime limitation of electrospray thrusters, there are many other effects that can contribute to a reduced lifetime. Models as well as experimental techniques to analyze the various lifetime limitations are developed in [7] and [9] and, as mentioned previously, efforts are being made to increase the lifetime of current iEPS thrusters. However, in the near term future, even if the target performance metrics for iEPS thrusters are met the thrusters will not have sufficient lifetime to produce enough $\Delta$V to conduct deep-space missions. In addition, even if the lifetime of the thrusters were infinite, a stage-based approach provides multiple other benefits such as propulsion system redundancy or the potential for new avenues of mission optimization.

## 1.2 Staging Concept

To increase the $\Delta$V output of an electrospray thruster propulsion system, the lifetime limitation has to be overcome. While the lifetime of electrospray thrusters will increase as the technology matures, increasing the lifetime to the point where 3 km/s of $\Delta$V could be produced would take a substantial amount of development. Therefore, in order to enable deep-space, and more generally high $\Delta$V, missions with CubeSats, an alternative method needs to be developed that bypasses the lifetime limit of an individual electrospray thruster in order to increase the overall lifetime of the propulsion system.

A staging concept is proposed where the propulsion system consists of a series of stages of electrospray thruster arrays. Figure 1-7 shows a concept image of the

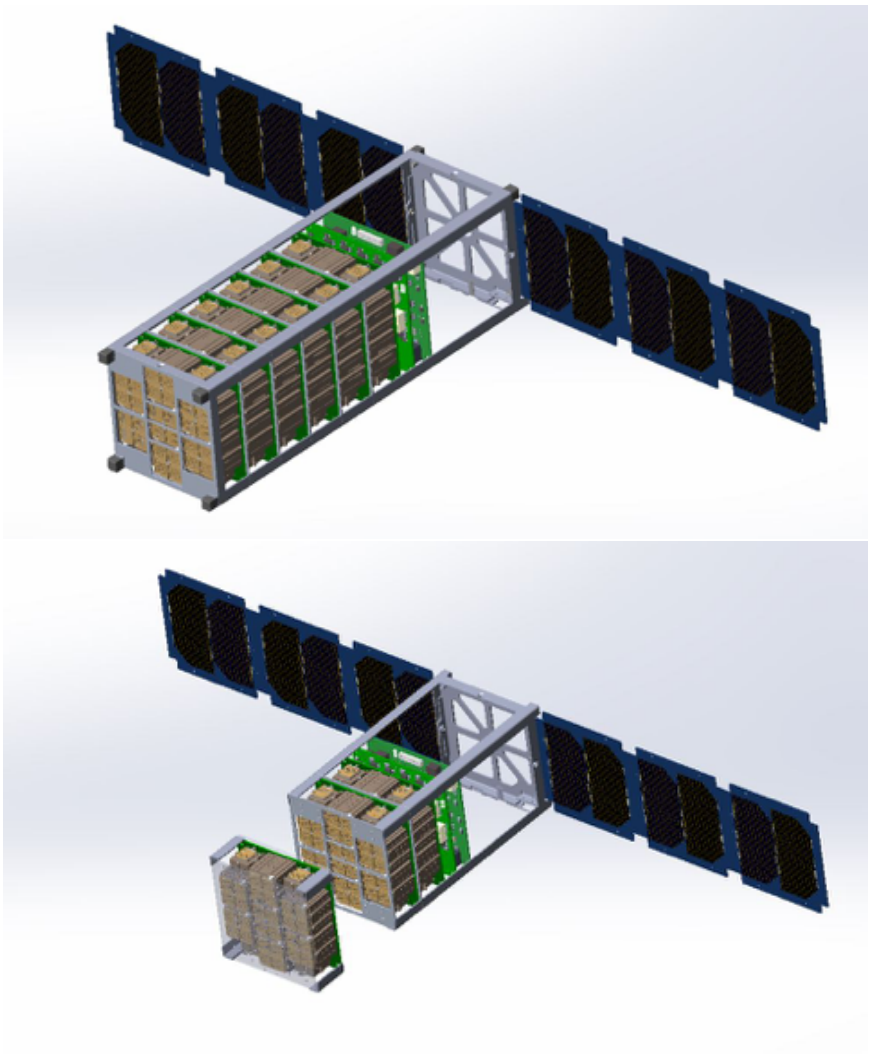

Figure 1-7: Concept image of staging on a 3U CubeSat [10]

staging system on a 3U CubeSat. As an array of electrospray thrusters reaches its lifetime limit, it is ejected from the spacecraft exposing a new array of thrusters in order to continue the mission. With such a system, the lifetime limit of an individual electrospray thruster is bypassed and the lifetime of the overall propulsion system can be arbitrarily increased by increasing the number of stages.

In terms of the $\Delta$V production, Figure 1-8 shows the $\Delta$V versus wet mass for a stage-based system with one to nine stages. We can see that a nine stage system can provide enough $\Delta$V to complete the mission and has mass low enough that the system is compatible with the CubeSat form factor. As will be shown in Section 3.2.4, the volume of the nine stage propulsion system is 2.1U leaving enough mass and volume

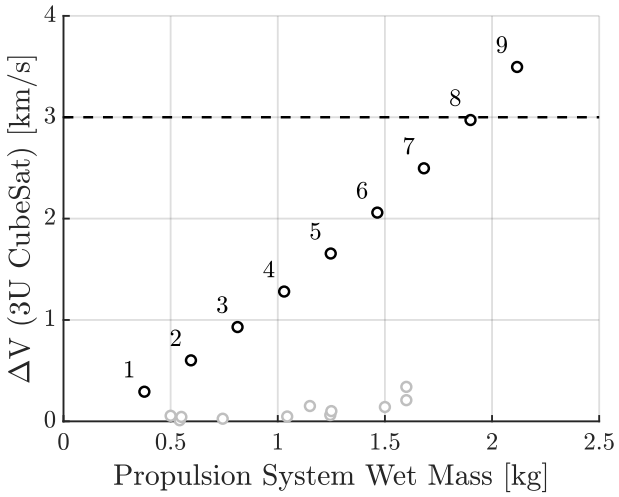


Figure 1-8: $\Delta$V versus wet mass for a 3U CubeSat compatible stage-based system

for a small, but capable, mission.

The remainder of this thesis is dedicated to the design, analysis, and application of a stage-based electrospray propulsion system. Chapter 2 covers the design of the mechanisms for a stage-based propulsion system as well as their testing in a vacuum environment and integration with actual thrusters for a full laboratory demonstration of a stage-based propulsion system. Chapter 3 analyzes a stage-based system from an analytical approach and develops methodologies for preliminary propulsion system and mission analysis with stage-based systems and the framework for autonomous decision making on small spacecraft with stage-based propulsion systems. Chapter 4 looks at the application of stage-based propulsion systems for missions to near-Earth asteroids as well as extensions of analytical methodologies for analytical guidance of spacecraft performing orbit transfers and escape missions enabling complex missions to be performed with computationally simple reference trajectories.

# Chapter 2

# Design

Two approaches could be used to increase the total lifetime of the propulsion system. Either the lifetime of individual thrusters could be increased, or an alternative system could be developed that bypasses the lifetime limit of the thrusters. Near-term developments at the SPL aim to increase the lifetime of individual thrusters through improvements in materials and manufacturing techniques. However, those developments only expect to increase the lifetime by a factor of 2 or 3, still less than the required firing time to enable deep-space missions from geostationary orbit. In addition, even if the lifetime of the thrusters were infinite, a stage-based approach opens up new avenues for mission optimization similar to the optimization of launch vehicles. Therefore, a staging concept is proposed with sequential stages of thruster arrays. One set of thrusters is fired until the lifetime limit before being ejected from the spacecraft and exposing a new set of thrusters. Through staging, the lifetime limit of individual thrusters is bypassed in order to increase the overall lifetime of the propulsion system. Figure 1-7 shows a concept image of a stage-based system and a CubeSat staging a set of thrusters mid-flight.

Development of a staging concept also provides two additional benefits. Firstly, stages can be used to provide redundancy for the propulsion system. Second, as thrusters are fired they might, after some time, decay and their performance decreases. Current efforts to minimize the effect of this decay involve increasing the input voltage to the thruster [11]. However, increasing the input voltage further accelerates thruster

decay and requires more power. By staging thrusters, a new, fresh set of thrusters will be used thereby avoiding the effects of thruster degradation.

Normally, this staging concept would not be feasible for most propulsion systems. However, the compact nature of iEPS thrusters and the lack of need for ionization chambers, pressurized propellant containment, and propellant feed systems means that the contribution of a single thruster array to the overall spacecraft mass and volume is small relative to other spacecraft systems. A complete array of thrusters compatible with a 3U CubeSat with enough fuel for 500 hours of firing only occupies approximately 0.2U (200 $cm^3$) of volume and weights 220 grams.

To develop the stage-based propulsion system, two mechanisms are required. The first is the staging mechanism itself which holds together successive stages during flight and separates the outermost stage at the time of staging. The second is a routing mechanism that passively routes control signals to the active stage. All thruster stages will use the same control electronics. Therefore, it is necessary to route the control signals to the correct stage. By performing the routing mechanically and passively, the control electronics can remain "stage-blind" and no electrical addressing of individual stages will be required. Both mechanisms are designed, prototyped, and demonstrated in a vacuum environment with iEPS thrusters to demonstrate a stage-based propulsion system.

## 2.1 Staging Mechanism Design

The staging mechanism is based on a fuse wire approach. Successive stages are held together with a thin stainless steel wire. At the time of staging, a high current (10 A) provided by a high power density ($\leq$ 200 m$\Omega$ ESR) ultra-capacitor is run through the wire, heating it up until it melts. After the wire melts and the stages are separated, a compression spring is used to eject the stage from the spacecraft. The wire is housed in a ceramic casing and attaches to standard 4-40 standoffs allowing for easy integration to existing iEPS electronics boards.

Figure 2-1 shows a diagram of the ceramic casing. The full staging mechanism is

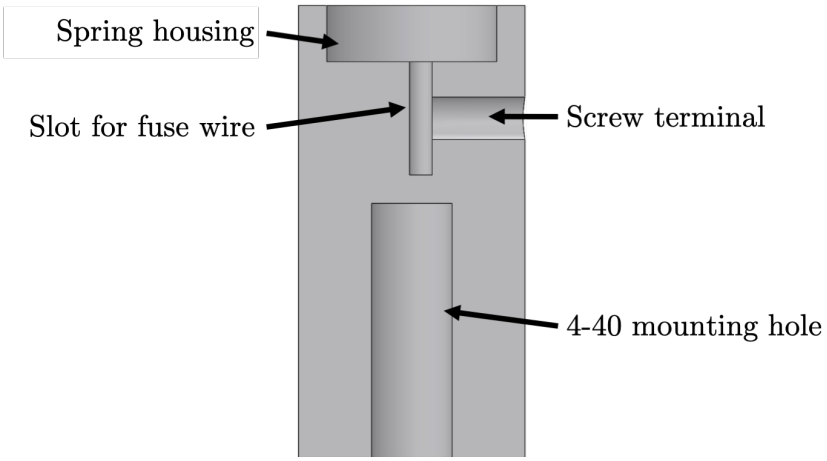


Figure 2-1: Diagram of ceramic casing for staging mechanism

composed of two ceramic casings both with their spring housings facing inwards. A 0-80 screw terminal is used to hold the stainless steel wire under tension due to the compressed spring and to provide electric contacts for the capacitor. The slot for the fuse wire is slightly off center such that when the fuse wire is held in the slot, the wire itself is centered in the ceramic casing. A 4-40 threaded hole is included at the back of the casing for mounting. Figure 2-2 shows the staging mechanism in operation. The entire fusing procedure takes approximately 100 ms. A gap between the ceramic casings is intentionally added during this test in order to provide visibility to the fuse wire. During normal operation, the ceramic casings are flush.

Similar approaches have been explored previously for miniature release mechanisms for small satellites. A nichrome burn-wire mechanism is explored in [12] where a nichrome wire is heated up in order to cut through a Vectran tie down cable. The release mechanism in this research differs from [12] in that the wire itself is melted to activate release rather than used to cut through a second wire therefore simplifying the mechanism design.

Multiple miniature release mechanisms are explored in [13] including a fuse wire based mechanism. The fuse wire mechanism in [13] is based on a beryllium-copper wire and has the wire loop through a retainer mechanism. The mechanism in [13] uses five unique components and requires the fuse wire to be etched in order to control the fusing location. The mechanism developed in this research keeps the fuse wire

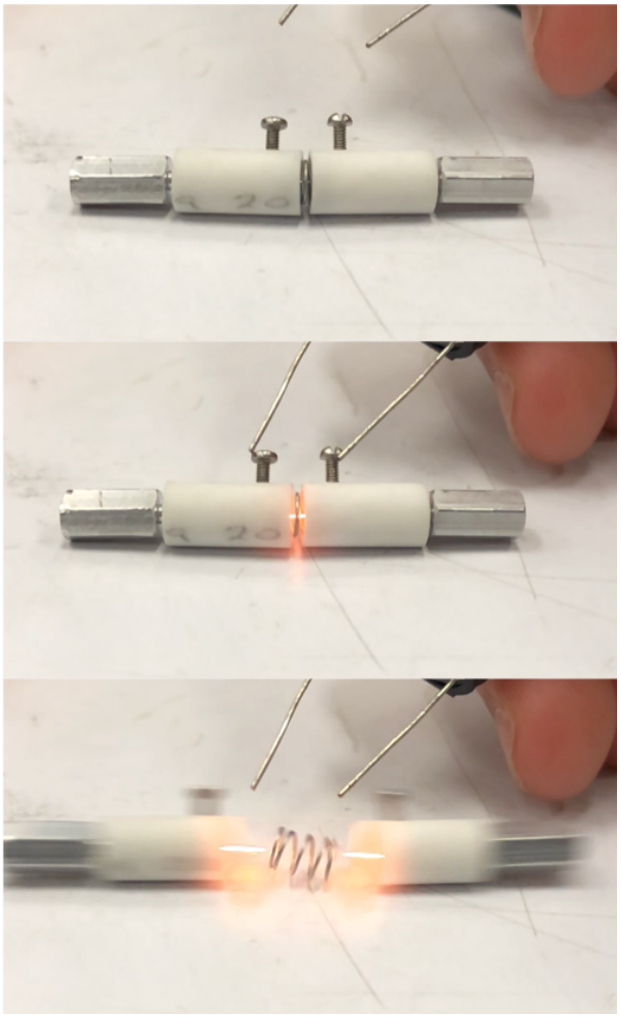

Figure 2-2: Demonstration of staging mechanism in air

straight and uses four unique components, only one of which, the ceramic casing, requires fabrication. By keeping the wire straight and securing it between two screw terminals, no wire etching is required as the wire can fuse in any location and still release the two stages.

### 2.1.1 Fuse Wire Material Selection

Material selection for the fuse wire consists of balancing mechanical and thermal properties. Desirable mechanical properties are low density and high tensile strength while desirable thermal properties are low specific heat capacity and low melting point. These properties can be combined to form a fusing metric, $\Gamma$, which is a function of the wire's initial temperature and defined as

$$\Gamma(T_0) \equiv \frac{\rho \; c \; (T_\mathrm{m} - T_0)}{\sigma} \tag{2.1}$$

where $\rho$ is the wire's density, $c$ is the specific heat capacity, $T_\mathrm{m}$ is the melting point, $T_0$ is the initial wire temperature, and $\sigma$ is the ultimate tensile strength. The fusing metric is also equal to the ratio of the required energy to fuse the wire, $E_\mathrm{f}$, to the maximum load the wire can carry, $F$, and the length of the wire, $l$

$$\Gamma \equiv \frac{E_\mathrm{f}}{F \; l} \tag{2.2}$$

For a given maximum load and wire length, set by the form factor of the spacecraft and staging mechanism, the fusing metric gives the minimum energy required for fusing before losses. Materials with a lower fusing metric are therefore more desirable.

Figure 2-3 shows the ultimate tensile strength versus the fusing energy per unit volume for various materials starting from an initial temperature of 0° C. Lines originating from the origin represent lines of constant fusing metric with lines with a larger slope correspond to lower fusing metrics. The line for $\Gamma = 10$ is shown for reference. Per this analysis, good material choices are the stronger aluminum and beryllium-copper alloys. In addition, pure tin is a particularly good choice with a

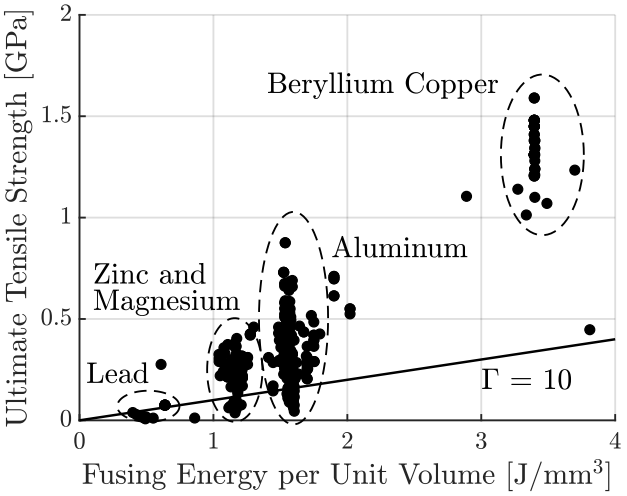


Figure 2-3: Fusing metric for various metals

fusing metric of 1.3.

Beyond mechanical and thermal properties, the electrical properties of the material determine its ability to be integrated into the spacecraft system. While pure tin has a low fusing metric, its low conductivity prevents its use given current capacitor capabilities. A 6.35 mm long pure tin wire capable of holding 40 N of force has a resistance an order of magnitude lower than the internal resistance of commercially available high power density capacitors (∼200 mΩ ESR). This discrepancy in resistance prevents power dissipation in the wire and therefore prevents fusing. Figure 2-4 shows the available energy output from a capacitor with energy capacity of 50 J and internal resistance of 200 mΩ. Required energies for fusing for materials shown in Figure 2-3 as well as total wire resistances are shown for 6.35 mm long wires capable of holding 40 N of load (equivalent to 4 wires each holding 10 N of load). We can see that most materials have very low resistances (∼5 mΩ) due to their low resistivity and therefore do not dissipate enough energy for fusing.

For this work, stainless steel 304 (SS304) is used as the fuse wire material. Although SS304 has a poor fusing metric (∼11) we can see from Figure 2-4 that its relatively high resistivity means that more of the capacitor energy is dissipated in the wire compared to most other materials considered in this study thereby allowing for wire fusing with sufficient safety margin. In addition, SS304 is readily available

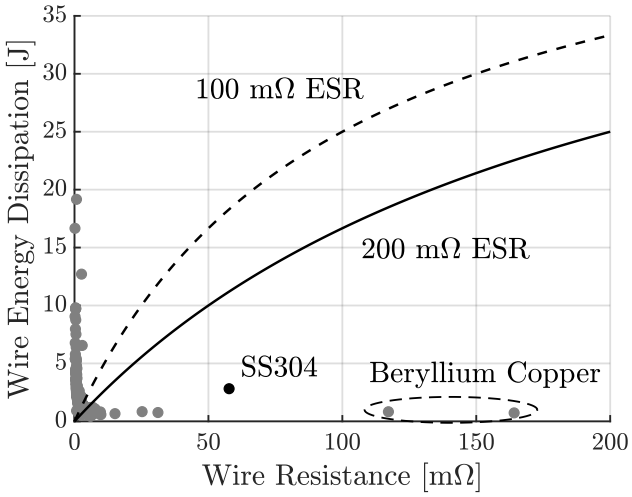


Figure 2-4: Effect of capacitor internal resistance on available energy for fusing given system properties

which allows for rapid prototyping. As capacitors with lower internal resistances are developed, materials such as tin which offer better fusing metrics can be used. Figure 2-4 also shows the available energy for fusing if the internal resistance of the capacitor is reduced by half to 100 mΩ.

Select beryllium-copper alloys are the only materials surveyed that have lower required fusing energy and higher wire resistance than SS304. However, given that SS304 is more readily available and can be fused with the capacitor considered in this study, SS304 is used for all tests in the in this work. Future work will consider using beryllium-copper alloys as the fuse wire material.

The fuse wire itself is 6.35 mm long and has a diameter of 0.203 mm (0.008 in). Each fuse wire can therefore hold ∼16 N of load. Given the fusing metric of SS304 ∼11, the estimated energy to fuse the wire is 1.15 J. As the melting point of SS304 is high (1400° C) the effect of initial wire temperature is minimal and so a reference of 0° C is used.

### 2.1.2 Vibration Analysis

With the addition of the staging mechanism, successive stages are only held together by 2-4 thin metal wires thereby influencing the vibration characteristics of the space-

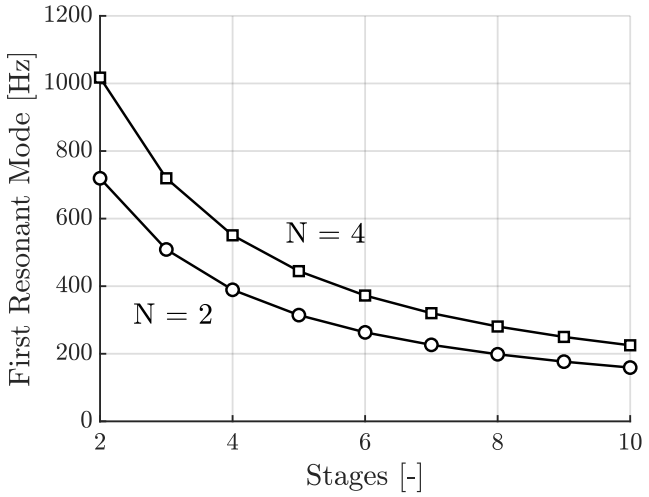


Figure 2-5: First resonant mode versus number of stages with 2 or 4 SS304 staging mechanisms per stage

craft during launch. While the entire spacecraft structure could be constrained, in the worst-case scenario the entire vibrational load will have to be absorbed by the fuse wires.

The stack of stages is approximated by stacked spring-mass systems where the spring constant, $k$, is approximated as

$$k = N\frac{A\ E}{L} \tag{2.3}$$

where $N$ is the number of staging mechanisms per stage, $A$ is the wire cross-sectional area, $L$ is the relaxed wire length, and $E$ is the Young's modulus of the wire material, SS304 in this case. Figure 2-5 shows the first resonant mode of the staging stack versus number of stages for both 2 and 4 SS304 staging mechanisms per stage. In all cases, the first resonant mode is greater than 100 Hz and will therefore avoid dynamic coupling between the low frequency dynamics of the launch vehicle and the stages.

In actuality, the first resonant modes will be higher than in this analysis. The spring-mass approximation allows for compression of the fusing wire. On the staging mechanisms, compression of the fusing wire is constrained by the stiffer machinable ceramic casing. Future work will involve experimental measurement of the resonant

modes of the staging mechanisms as well as their response to random vibration.

## 2.2 Routing Mechanism Design

The routing mechanism is a custom made, normally closed, momentary push button switch. When a preceding stage is present, the mechanism is opened preventing control signals from entering the stage. When the preceding stage is ejected, the mechanism is closed and the stage becomes active. After the thrusters on the stage reach the end of their lifetime, the stage is ejected, automatically activating the next stage. With this mechanism the control electronics remain "stage blind" and do not need to track which stage is active. This greatly simplifies the electronics design as existing iEPS electronics boards can continue to be used without needing to add extra electronics for addressing of individual stages. It also allows for greater flexibility when adding or removing stages as the number of stages does not impact the electronics boards.

Figure 2-6 shows a proof of concept of the routing mechanism concept with an early routing mechanism prototype. We can see that without any actuation, the contacts between the two ends of the routing mechanism are connected and the multimeter reads a finite resistance. When the mechanism is actuated, through pushing down the button, the connection between the contacts is broken and the multimeter is overloaded as it cannot read a finite resistance. When integrated into a stage-based propulsion system, each stage will physically actuate the routing mechanism for the stage below it. The button will be pressed down by the stage board such that when the above stage is present the routing mechanism is inactive (connection between contacts broken) and when the above stage leaves, the routing mechanism becomes active (contacts are connected).

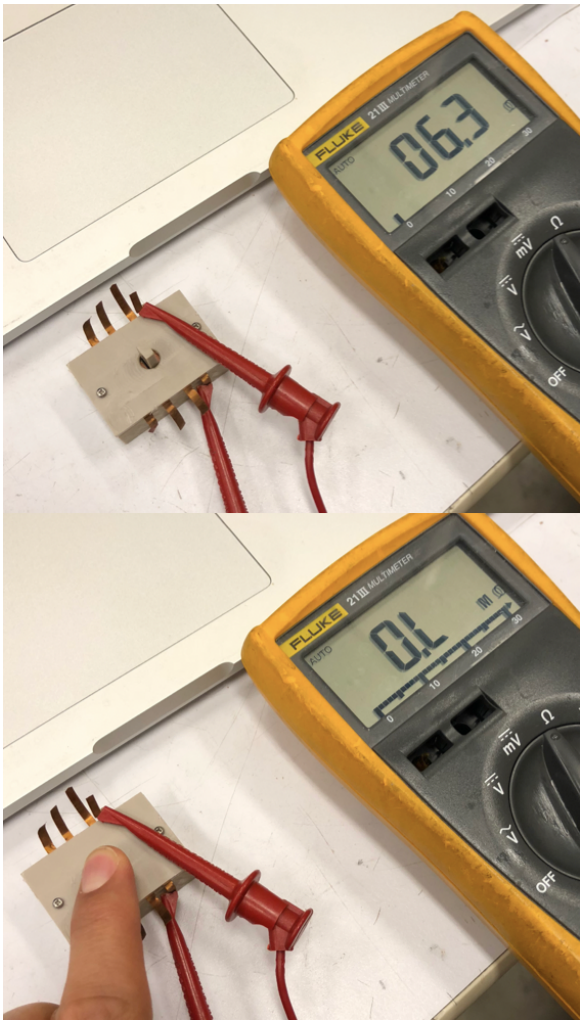


Figure 2-6: Proof of concept with early routing mechanism prototype

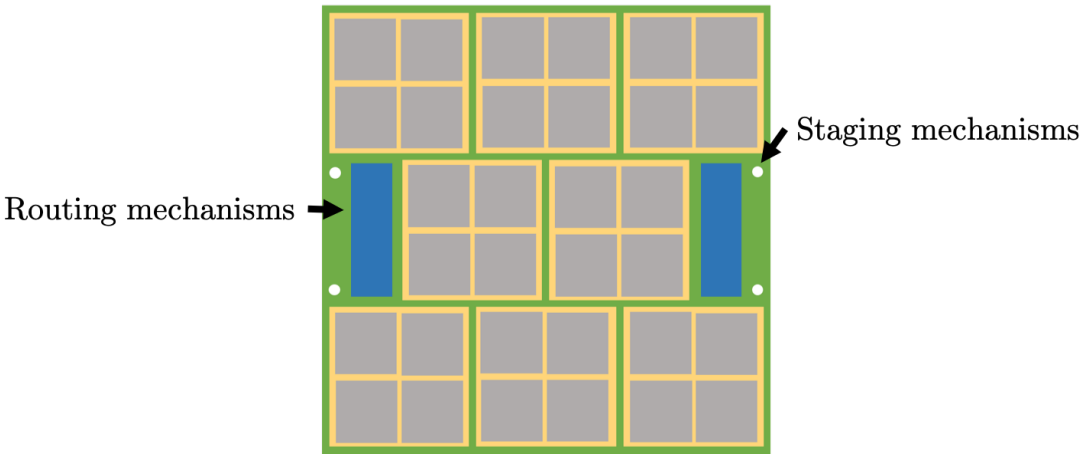


Figure 2-7: Stage configuration with staging and routing mechanisms

## 2.3 Stage Configuration

Both the staging and routing mechanisms can be easily integrated onto the proposed stage configuration in Figure 1-6. The staging mechanisms simply replace the 4-40 standoffs used for mounting and the routing mechanisms can be added in the spaces next to the center row of thrusters. Figure 2-7 shows the thruster configuration with the routing mechanisms included and with the mounting holes replaced with staging mechanisms. All control electronics required for thruster firing and staging mechanism activation will be mounted on separate electronics boards below the stage stack and have their signals routed to the active stage through the routing mechanisms.

## 2.4 Mechanism Testing

Testing of the stage-based system is conducted first in air and then in vacuum. Figure 2-8 shows the test setup for an in-air demonstration of the staging and routing mechanisms with dummy stages. Two staging mechanisms are used for the test and are fused with a PBL-4.0/5.4 passively balanced ultracapacitor from Tecate Group. The control electronics first charge the capacitor to at least 4.4 V before fusing the staging mechanisms. An LED is included on each stage to represent electrical connections for thrusters with a common power connection run through the routing mechanism. We can see that in the initial setup, the LED on the first stage is lit since it is the

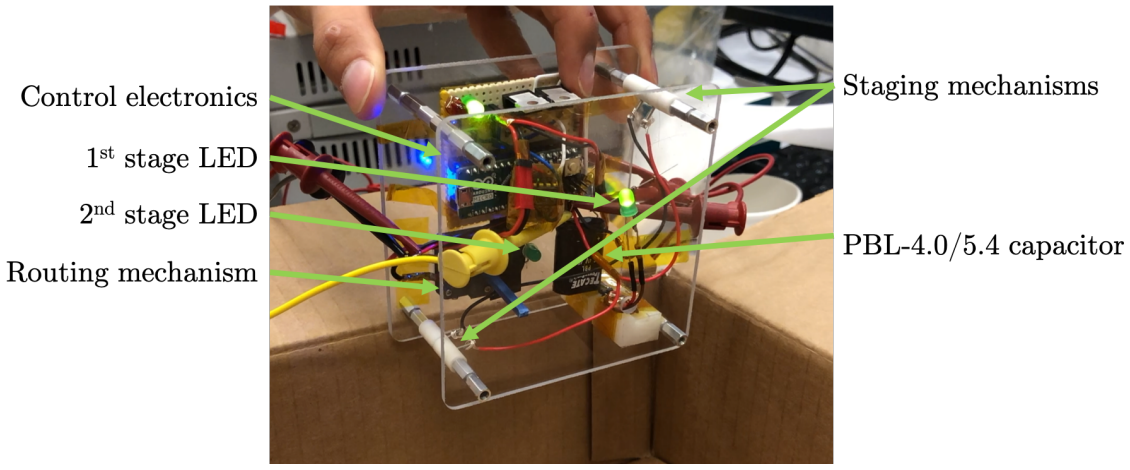


Figure 2-8: Test setup for in-air demonstration of staging and routing mechanisms

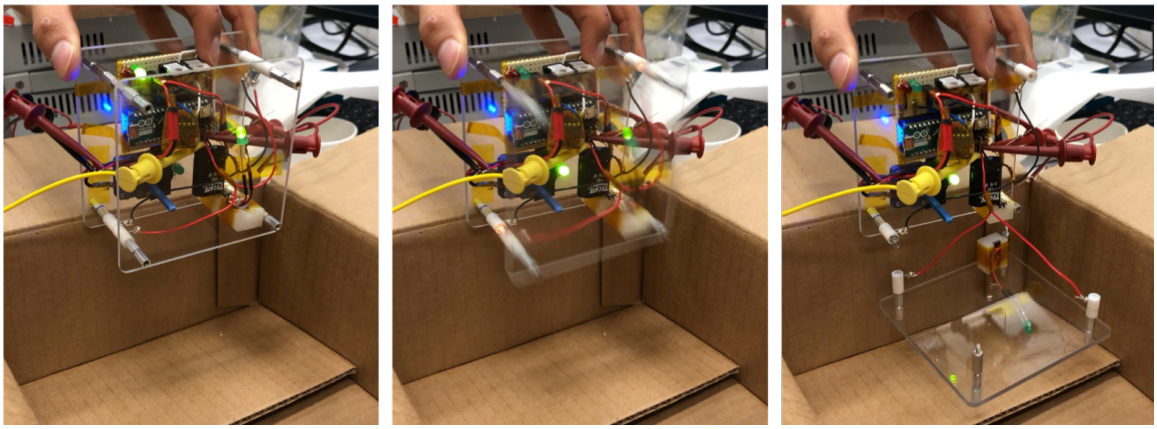

Figure 2-9: Demonstration of staging and routing mechanisms with dummy stages in air with LED's representing thrusters

active stage while the LED on the second stage is not lit.

Figure 2-9 shows the in-air demonstration. In the first image, the system is in the initial configuration as shown in Figure 2-8. In the second image, the staging mechanisms are activated. We can see the glow from the fuse wires as the first stage is ejected. In addition, the LED on the second stage is now lit as the contacts on the routing mechanism are closed when the first stage is ejected. In the final image, the first stage is fully ejected and the second stage is now active. The LED on the second stage remains lit, representing the second array of thrusters now firing.

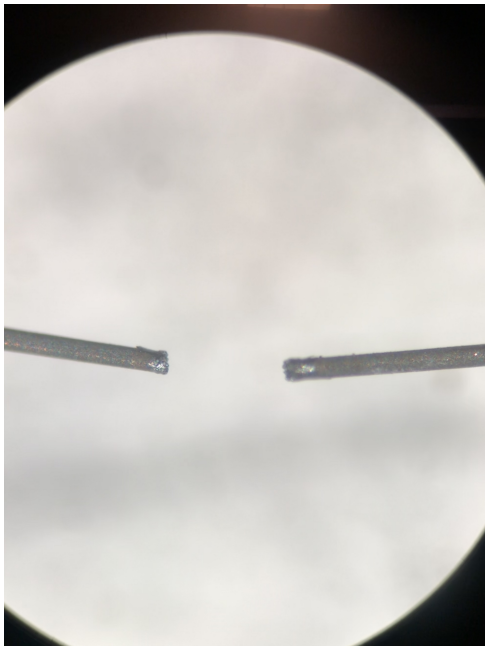

Figure 2-10: Fuse wire after staging mechanism operation in air

### 2.4.1 Vacuum Testing

To mature the stage-based propulsion system technology, the staging system needs to be tested in a vacuum environment. Since the routing mechanism operation is entirely mechanical, there is no expected difference in operation in air versus vacuum. However, the behavior of the fusing mechanism might have minor differences. Figure 2-10 shows the fuse wire after staging mechanism operation in air. We can see that the wire has oxidized around the fusing point due to the high heat and the break in the wire looks more like the wire snapped rather than melting.

The test setup for testing the staging mechanism in a vacuum chamber is shown in Figure 2-11. The same PBL-4.0/5.4 ultracapacitor from Tecate Group is used and a relay controls whether or not the capacitor is charging or the staging mechanism is fusing. No spring is included in the staging mechanism during this test to prevent debris in the vacuum chamber. Figure 2-12 shows the staging mechanism operating in vacuum at $\mu$Torr levels. The green LED in the first image indicates that the capacitor is charging while the yellow LED in the second image indicates that the staging mechanism is being fused. We can see the fuse wire in the staging mechanism

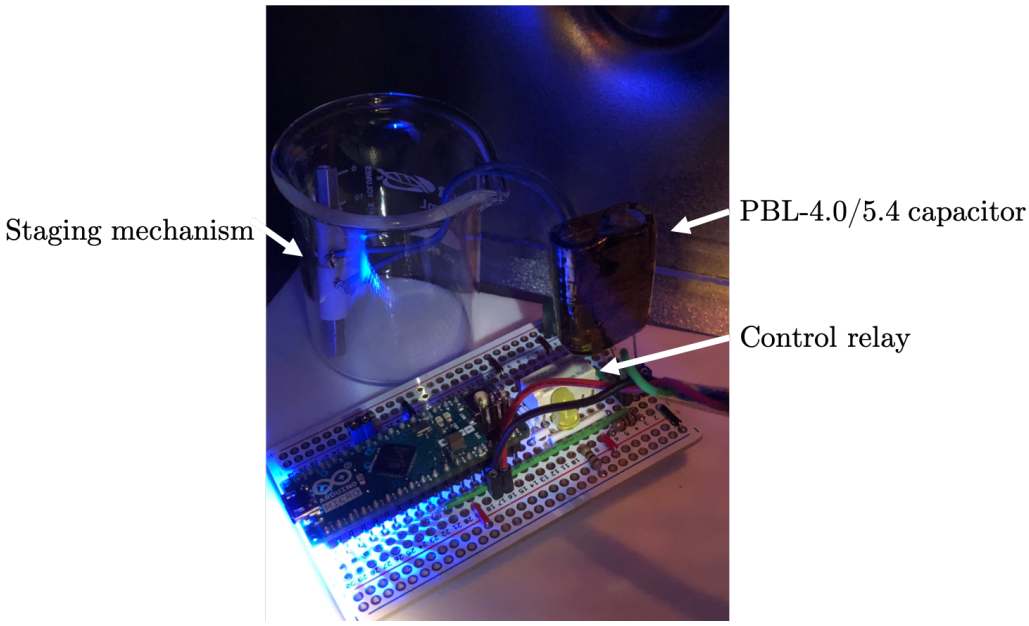


Figure 2-11: Test setup for vacuum testing of staging mechanism

glowing during operation as expected.

Figure 2-13 shows the capacitor output voltage throughout the test. We can see that the capacitor charges to 4.4 V in just over 19 minutes, requiring an average power input from the spacecraft bus of only 0.05 W. After the capacitor voltage reaches 4.4 V, the electrical connection from the power supply to the capacitor is broken and the capacitor is electrically connected to the staging mechanism to initiate fusing. Figure 2-14 shows the portion of the voltage plot in Figure 2-13 corresponding to fusing. We can see a drop in output voltage due to the equivalent series resistance of the capacitor. The fuse wire fuses in approximately 100 ms after which the capacitor output voltage recovers to its final value of 4.2 V. Energy wise, 4 J of energy are used during the fusing which is split between the fuse wire and the internal resistance of the capacitor. Figure 2-15 shows the fuse wire after staging mechanism operation in vacuum. In contrast to the fuse wire that was operated in air in Figure 2-10 we can see that no oxidation occurred, due to the lack of air, and that both sides of the fuse wire have clearly melted at the fuse point in order to cause the separation of the staging mechanism.

The staging and routing mechanisms can also be tested together in a combined

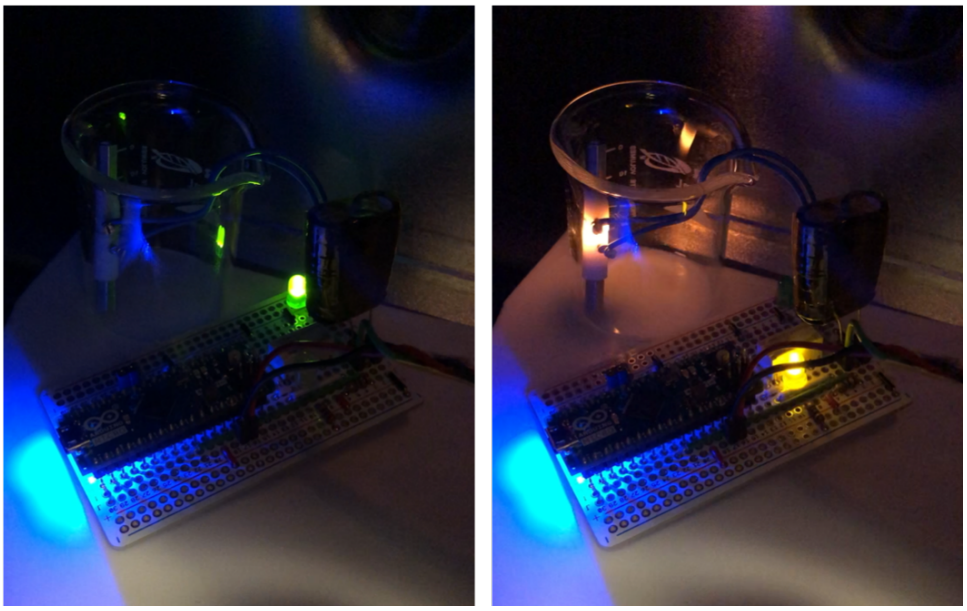

Figure 2-12: Demonstration of staging mechanism fusing in vacuum

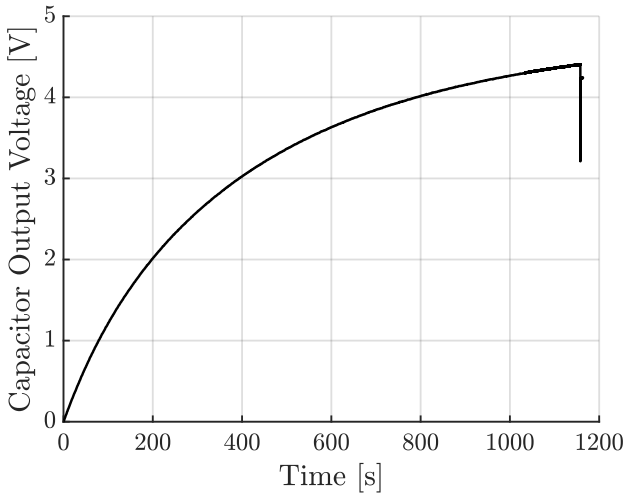


Figure 2-13: Capacitor output voltage during staging mechanism test in vacuum

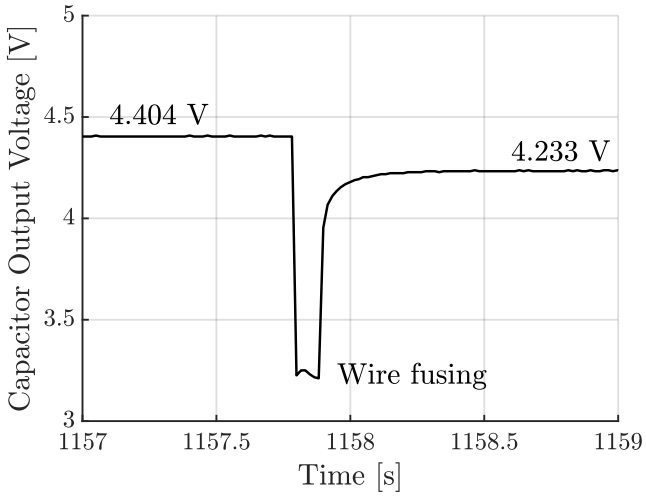


Figure 2-14: Capacitor output voltage during staging mechanism fusing in vacuum

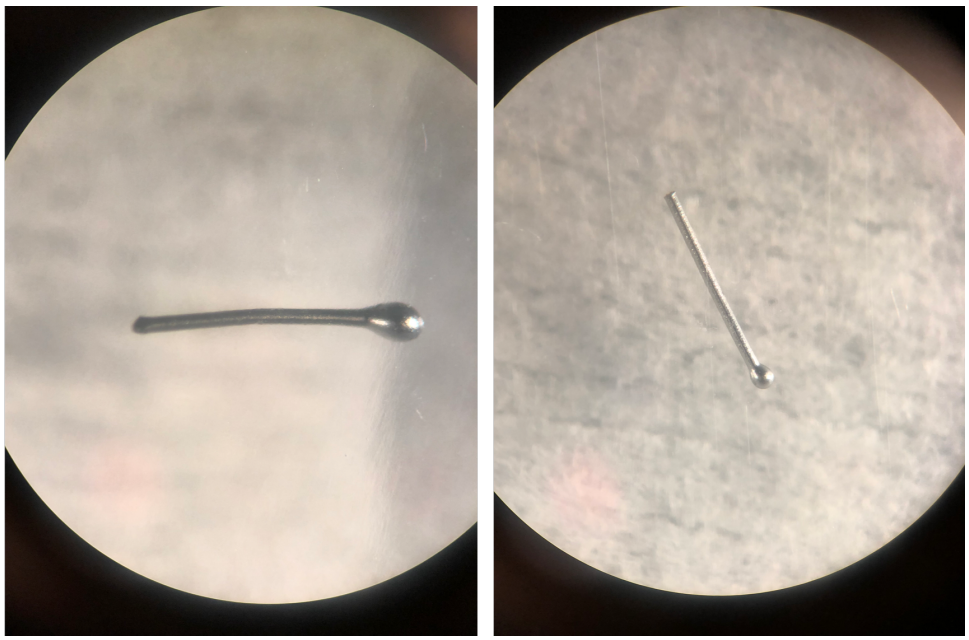

Figure 2-15: Fuse wire after staging mechanism operation in vacuum

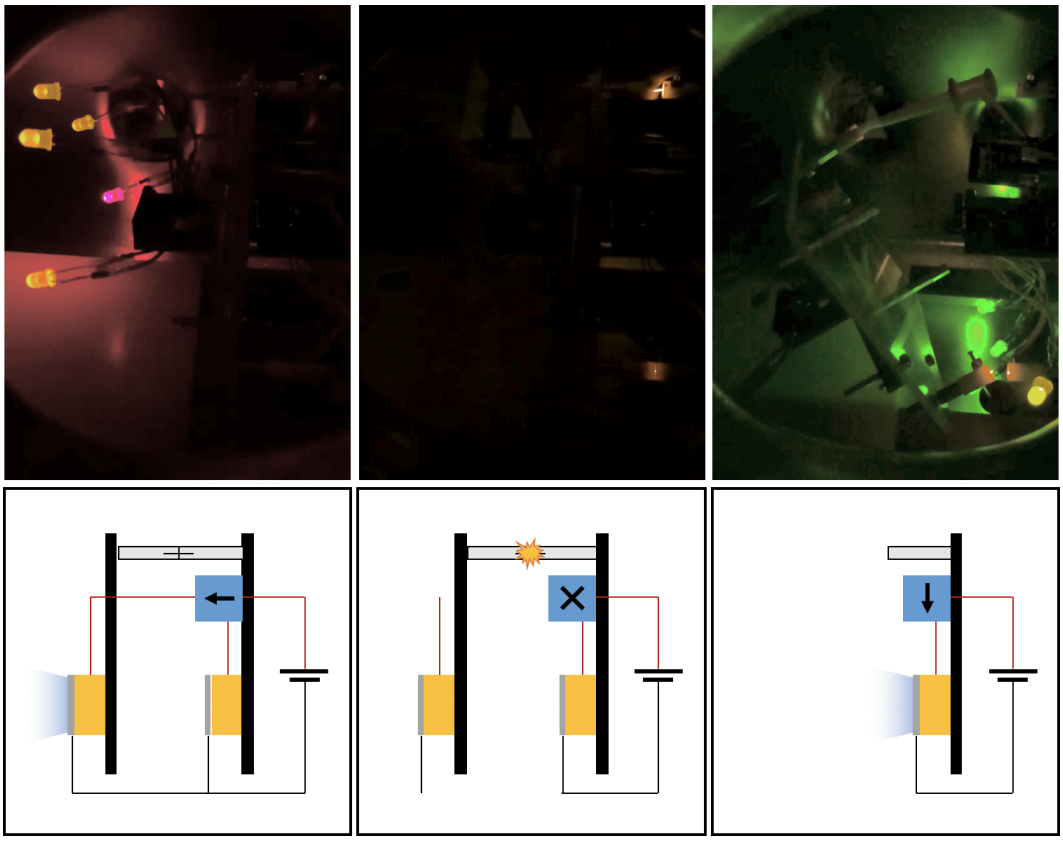

Figure 2-16: Demonstration of staging and routing mechanism with dummy stages in vacuum with LEDs representing thrusters

test with dummy stages similar to the in-air test in Figure 2-9. Figure 2-16 shows the combined test in vacuum at $\mu$Torr levels with LEDs as electrical placeholders for thrusters. The lighting in the chamber was dark throughout the test in order to properly see the visual cues, such as when the staging mechanism was activated. Therefore, a diagram is provided below the test sequence showing what is happening in the chamber throughout the test on an electrically equivalent thruster system.

The test used a two stage system with a common power supply for both stages. Initially, when both stages are present, the power for the LEDs is routed past the second stage and up to the first stage. We can see, in the first image, that the LEDs for the first stage are lit in this initial configuration and that the thruster on the first stage is firing in the supplemental diagram. After the first stage reaches its lifetime limit the staging mechanisms are activated. The electrical connection to the first stage is cut, visually demonstrated by the LEDs on the first stage no longer

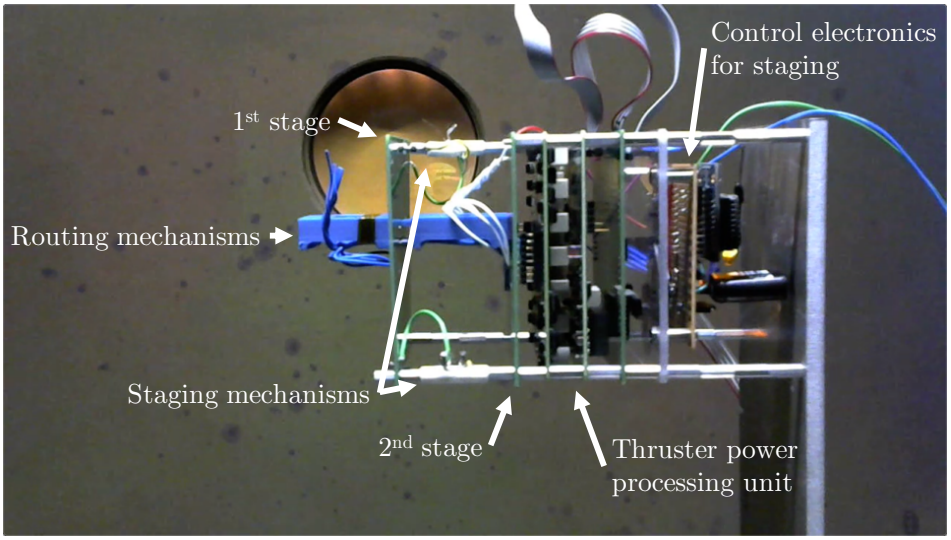


Figure 2-17: Test setup for stage-based propulsion system demonstration

lit up, and the electrical connections to the second stage are still not closed. The staging mechanism fuse wires are glowing as the mechanisms are activated in order to initiate staging. After staging has been completed, the first stage is ejected from the spacecraft activating the routing mechanism on the second stage and closing the associated electrical connections. The LEDs on the second stage are now lit representing the second stage thrusters now firing.

### 2.4.2 Fully Integrated Test

Figure 2-17 shows the test setup for testing of the staging and routing mechanisms with electrospray thrusters. The test used the already existing iEPS power processing unit with custom control electronics for the staging as well as custom thruster boards to hold two thrusters and to accommodate the routing mechanisms. During the test, aluminum foil was wrapped around the thruster power processing unit and staging control electronics in order to prevent potential charging due to reflection of emitted ions from the vacuum chamber walls. Figure 2-18 shows the thrusters mounted on one of the thruster boards prior to testing.

Figure 2-19 shows the voltage and current output when firing the first stage. We can see that emission was achieved in the ~900 V range. The thrusters were

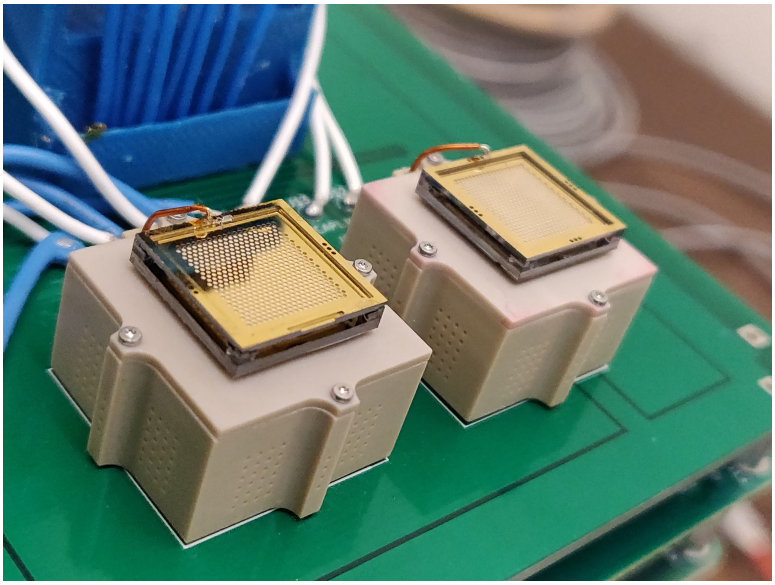

Figure 2-18: Thrusters mounted in custom electronics board

operated at 1000 V for three 30 second polarity cycles. We can see a significant asymmetry in the current levels between the two thrusters and also when the thruster polarities are switched. The thrusters were operated at a higher-than-intended current level. However, due to the high current level, Figure 2-20 shows a visible plume from the thrusters confirming that the thrusters were actually firing during the test. Unfortunately, the thrusters were left not firing over night and developed an electrical short by the morning. It is suspected that the short was due to gravity pulling the ionic liquid towards the edge of the emitter array and creating an electronic connection between the emitter array and extractor grid.

Since the first stage was deemed inoperable, it was staged from the propulsion system. Figure 2-21 shows the staging sequence. Initially, both stages are still attached to the propulsion system. The staging mechanisms are then activated and the first stage is ejected from the system. After staging, the propulsion system is left with only the second stage and is ready to continue thruster firing.

Figure 2-22 shows the voltage and current output when firing the second stage. The vast majority of the perceived noise in the output is due to switches in the thruster polarity. Unfortunately, only one of the two thrusters on the second stage successfully fired. The unfired thruster initially showed no signs of firing when a voltage was

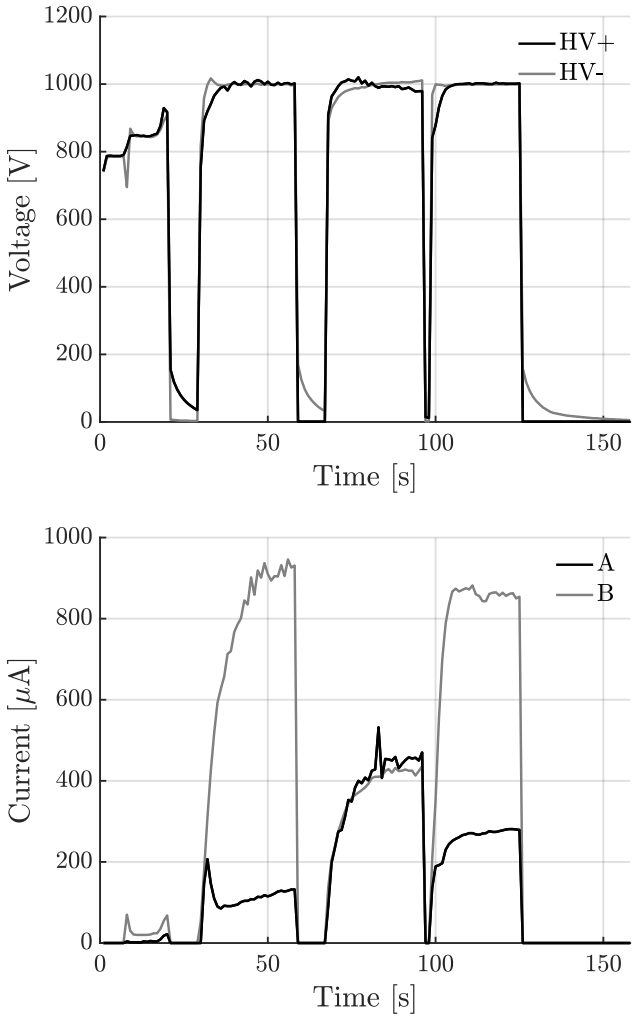


Figure 2-19: Voltage and current for first stage firing

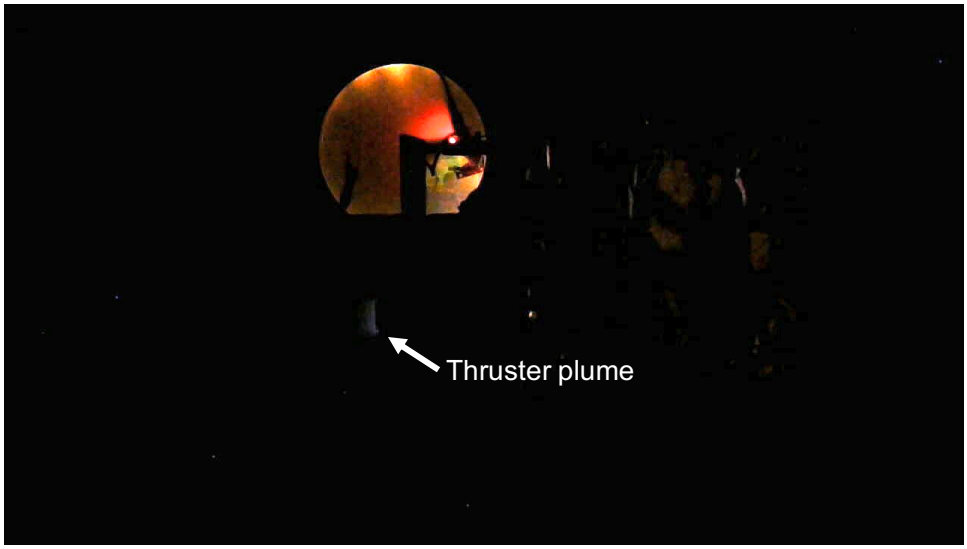


Figure 2-20: Thruster plume from first stage firing

applied before developing an electrical short rendering it inoperable. However, the thruster that did fire fired as expected in terms of output current. An emitted current of 150 $\mu$A was achieved and maintained for almost ten hours. Approximately ten hours into the test, a voltage trip caused the PPU to stop applying voltage to the thruster causing the thruster to sit not firing over night and developing an electrical short similar to what happened with the first stage.

This test serves as the first demonstration of a stage-based electrospray propulsion system. Electrospray thrusters on two different stages were fired and the first stage was successfully ejected from the propulsion system. While thrusters were rendered inoperable throughout the test, the causes do not appear to be associated with the stage-based propulsion system. In addition, all thrusters used for this test were test units and not engineering or flight units so unexpected behavior, such as premature shorting, was to be expected. Further refinement of both the staging and routing mechanisms is required to make the system flight ready. However, the mechanical feasibility of such a propulsion system has been demonstrated.

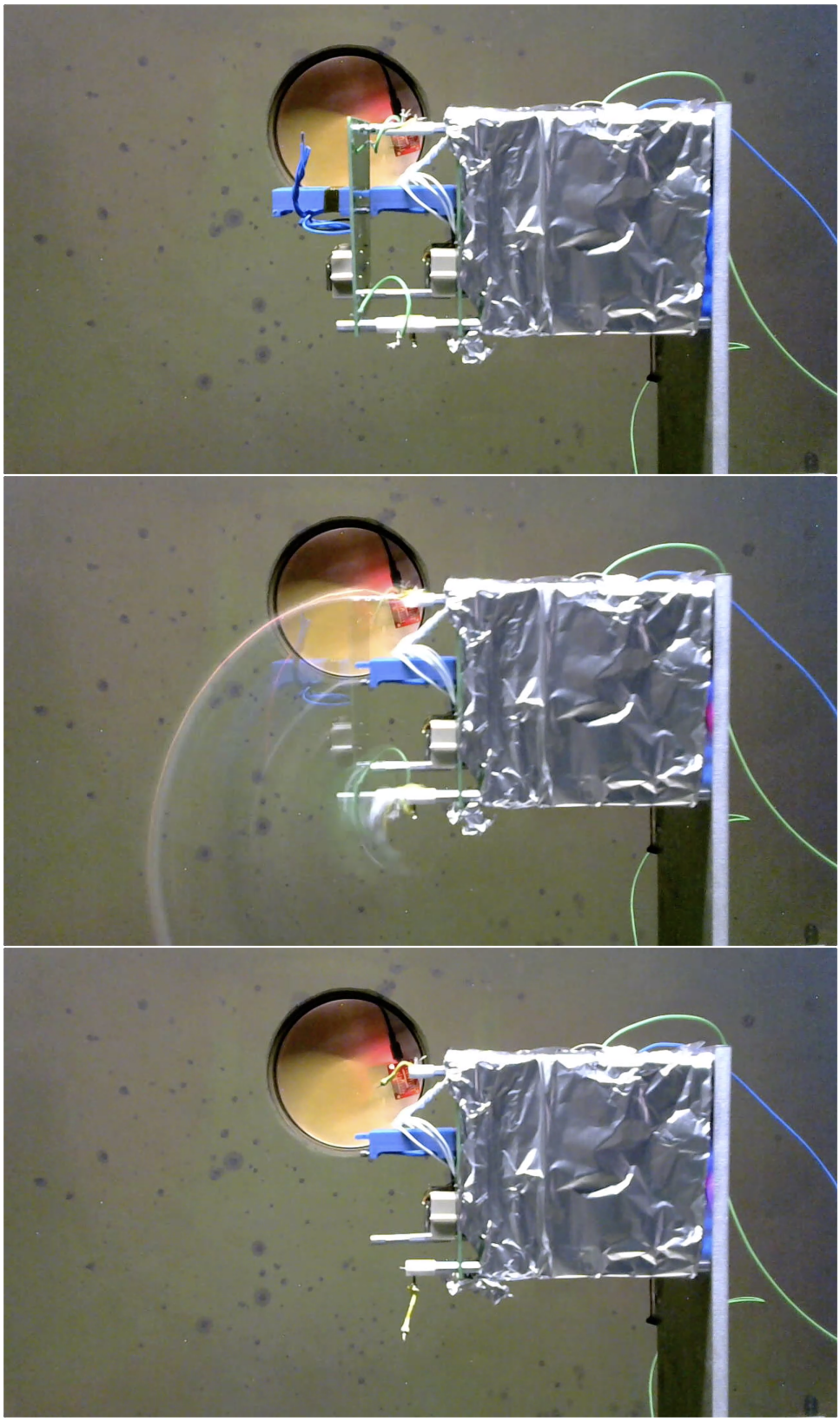

Figure 2-21: Demonstration of a stage-based electrospray propulsion system.

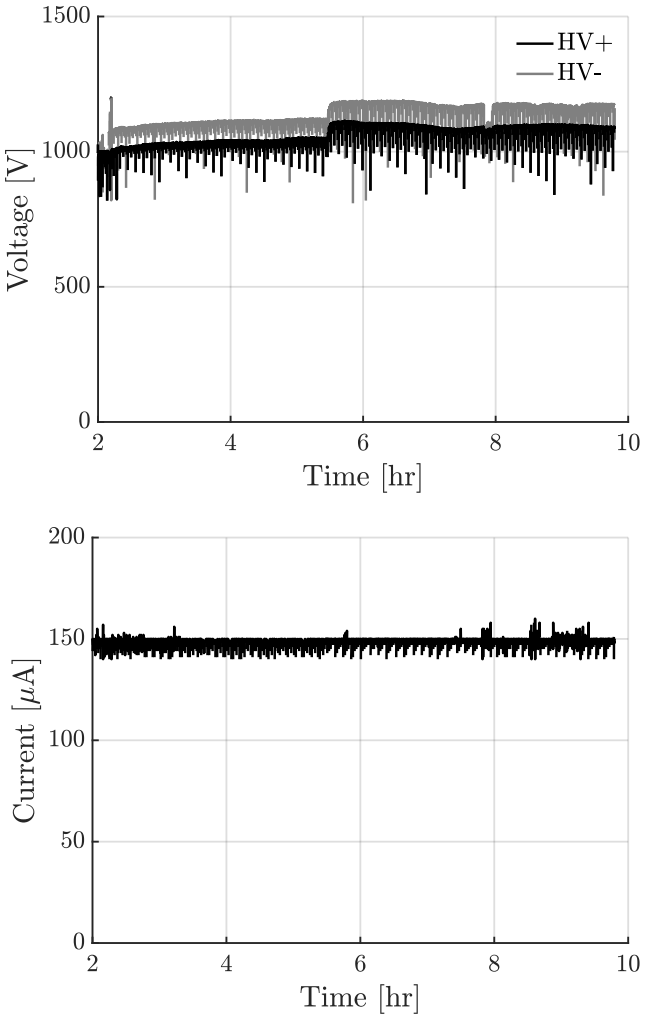


Figure 2-22: Voltage and current during second stage firing

# Chapter 3

# Analysis

## 3.1 Un-staged Escape Trajectory

Before analyzing trajectories with stage-based propulsion systems, it is worth analyzing trajectories of un-staged propulsion systems to first determine what control law and thrust program to use during escape. Specifically, there are two questions we aim to answer with this analysis:

- What control law should be used (what direction to apply thrust)?
- Should coast arcs be added to the trajectory to improve payload mass?

To determine the control law to use, three control laws are considered: angular pointing, velocity pointing, and free pointing. Angular pointing and velocity pointing mean that the thrust is constrained to be applied in the angular and velocity directions respectively. In free pointing, the thrust direction is left free and is optimized with the GPOPS-II general purpose optimal control software [14]. Of the three options, angular pointing and velocity pointing are considerably simpler control laws in regards to implementation on a small satellite. Angular pointing provides the additional benefit of maintaining a face of the satellite pointed at Earth which can be useful for navigation purposes. We will find that velocity pointing and free pointing do not provide any significant advantages over angular pointing in terms of escape time. Therefore, angular pointing will be the control law of choice.

The addition of coast arcs in the trajectory allows for a tradeoff between payload mass delivered to escape and escape time. Optimal control with calculus of variations is used to determine when to add coast arcs into the trajectory in order to maximize the payload mass delivered to escape for a given escape time. Calculus of variations allows the problem to be reduced from an optimization of a continuous time variable, the thrust input, down to an optimization over a few scalar values. However, the result of the optimization will give that adding coast arcs to the trajectory only provides marginal increases in the payload mass while requiring significant increases in escape time. Therefore, the final control law will be angular pointing with no coast arcs (continuous thrust).

### 3.1.1 Comparison of Control Laws

Three control laws are considered for the escape trajectory: angular pointing, velocity pointing, and free pointing. In all cases, thrust is applied continuously throughout the trajectory, then the three control laws are then compared based on the firing time required to achieve escape from geostationary orbit. Angular pointing and velocity pointing are easily evaluated by propagating the trajectory with their respective control law. For free pointing, the GPOPS-II general purpose optimal control software [14] is required in order to optimize the direction of thrust to minimize the required firing time.

Figure 3-1 shows the ratio of firing time for escape for the velocity pointing and free pointing control laws versus the angular pointing control law for various thrusts normalized by the iEPS minimum performance value. We can see that the velocity pointing and free pointing control laws provide marginal improvements in escape time compared to angular pointing with a maximum decrease in escape time of $\sim$1.35%. In addition, we can see that there is almost no difference between the velocity pointing and free pointing results.

The marginal difference between angular pointing and velocity pointing is due to the nature of the low-thrust escape spiral. Figure 3-2 shows the escape spiral for the minimum performance iEPS thrust along with the orbit of the Moon for scale. We can

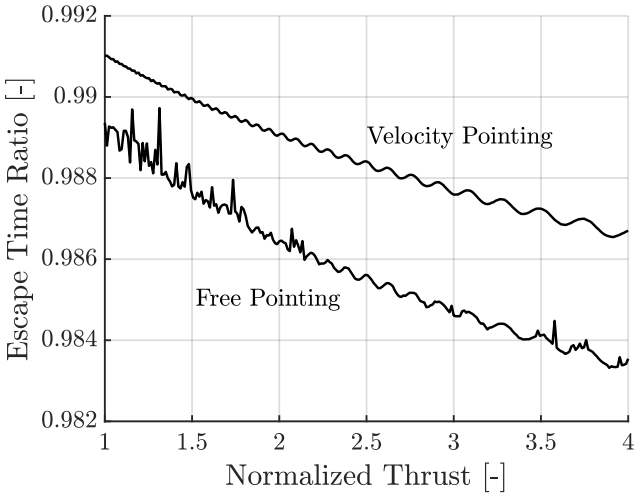


Figure 3-1: Ratio of required firing time for escape for velocity pointing and free pointing control laws versus angular pointing control law

see that except for the last revolution of the spacecraft around the Earth, the orbit is approximately circular. Therefore, there is little difference between the velocity pointing and angular pointing control laws. We can see this more clearly in Figure 3-3 where the angular difference between the velocity direction and angular direction is plotted over time. For the vast majority of the trajectory the two directions are nearly aligned with an angular difference of only $\sim$4.5 degrees after 75% of the trajectory has been completed.

The small difference between the velocity pointing and free pointing control laws is also not surprising. If we consider the specific power input of the propulsion system to the spacecraft

$$\frac{d\epsilon}{dt} = \frac{1}{m}\vec{F} \cdot \vec{v} \tag{3.1}$$

where $\epsilon$ is the specific energy of the orbit, $m$ is the mass of the spacecraft, $\vec{F}$ is the thrust vector, and $\vec{v}$ is the velocity vector, then we can see that the instantaneous change in the specific energy of the orbit is maximized if the thrust vector is aligned with the velocity vector. If the goal of the mission is to achieve escape ($\epsilon \to 0$) then the intuitive control law would be to align the thrust and velocity vectors - velocity

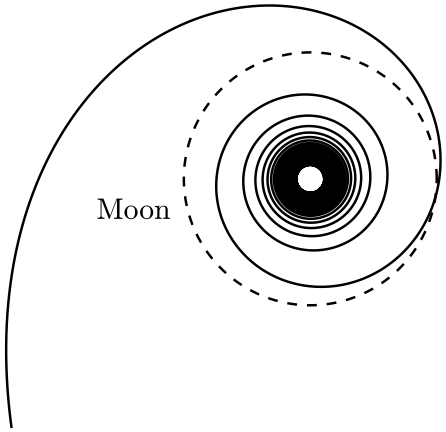


Figure 3-2: Low-thrust escape spiral from Earth without staging

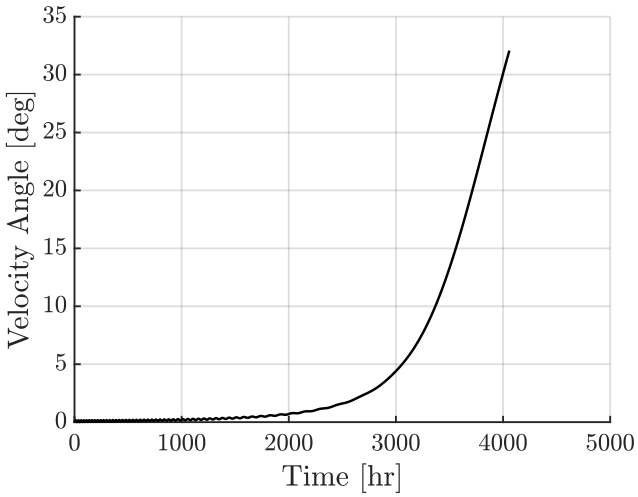


Figure 3-3: Angular difference between velocity direction and angular direction

pointing. The free pointing optimization can only make marginal improvements to the velocity pointing control law by sacrificing the instantaneous change in specific energy to slightly improve the change in specific energy at a later time in the trajectory.

Implementation wise, the free pointing control law is more complex than either the velocity pointing or angular pointing control laws and is susceptible to modeling errors. Both the velocity pointing and angular pointing control laws are simple to implement assuming knowledge of the spacecraft velocity vector. However, the angular pointing control law has the additional bonus that a face of the spacecraft will always be pointed towards Earth throughout the escape trajectory. This can be advantageous for communications and autonomous navigation. The spacecraft's radial position can be estimated by taking measurements of the angular diameter of the Earth during escape. In addition, the angular position of the spacecraft can be estimated by combining measurements from a star tracker and the position of the Earth in the spacecraft's camera. Therefore, while the velocity pointing control law does have a lower escape time than the angular pointing control law, angular pointing will be the default control law for future analysis.

### 3.1.2 Optimization with Calculus of Variations

In Section 3.1.1 angular pointing was selected as the control law but the analysis assumed constant thrust applied throughout the trajectory. Here, we are interested in optimizing our trajectory to minimize propellant mass usage by allowing for varying thrust throughout the trajectory. The goal of this analysis is to determine the tradeoff between escape time and propellant mass - can we save a significant portion of propellant mass by taking a little longer to reach escape? It is worth noting that this problem is a restricted form of Primer Vector Theory which is covered in [15].

Formally, the problem can be expressed as

$$\min_{F(t)} J = \text{propellant mass} = \int_0^{t_f} \frac{F(t)}{c} dt \tag{3.2}$$

subject to the dynamics

$$\dot{r} = v_r \tag{3.3}$$

$$\dot{\theta} = v_\theta / r \tag{3.4}$$

$$\dot{v}_r = v_\theta^2 / r - \mu / r^2 \tag{3.5}$$

$$\dot{v}_\theta = -v_r v_\theta / r + F/m \tag{3.6}$$

$$\dot{m} = -F/c \tag{3.7}$$

saturation limits for the input thrust

$$0 \leq F \leq F_{\max} \tag{3.8}$$

and the final condition that the spacecraft must achieve escape

$$\frac{1}{2}\left(v_r^2 + v_\theta^2\right) - \frac{\mu}{r} \geq 0 \tag{3.9}$$

We can solve this problem with optimal control using calculus of variations. A good reference for the derivation of the necessary conditions for optimal control is [16]. Here, we will advance the results of the derivation and form the Hamiltonian function by combining our cost function with our dynamics adjoined with costate variables $\lambda$

$$H = \frac{F}{c} + \lambda_r \dot{r} + \lambda_\theta \dot{\theta} + \lambda_{v_r} \dot{v}_r + \lambda_{v_\theta} \dot{v}_\theta + \lambda_m \dot{m} \tag{3.10}$$

where the time dependences of all variables has been dropped for clarity. Substituting in the dynamics and rearranging the equation we end up with

$$H = \left(\frac{1 - \lambda_m}{c} + \frac{\lambda_{v_\theta}}{m}\right) F + \lambda_r v_r + \lambda_\theta \frac{v_\theta}{r} + \lambda_{v_r}\left(\frac{v_\theta^2}{r} - \frac{\mu}{r^2}\right) - \lambda_{v_\theta} \frac{v_r v_\theta}{r} \tag{3.11}$$

The optimal control is the one that minimizes this Hamiltonian function. However, we can see that the Hamiltonian is linear in the control input. Therefore, we invoke

Pontryagin's minimum principle to say that the control thrust must be at one of the two saturation limits. Specifically, defining the switching function

$$S = \frac{1 - \lambda_m}{c} + \frac{\lambda_{v_\theta}}{m} \tag{3.12}$$

then the optimal control thrust is

$$F = \begin{cases} 0 & S > 0 \\ F_{\max} & S < 0 \end{cases} \tag{3.13}$$

We note that Pontryagin's minimum principle does not define what the control input should be when $S = 0$. However, this is only an issue if $S = 0$ for finite time which, in practice, does not occur for our problem.

To determine the optimal control for all time we simply track the value of the switching function over time turning on the thruster whenever the switching function is negative and turning it off when the switching function is positive. To do this, we need to know the values of the costates through time. Optimal control theory also gives us the dynamics of the costate variables as

$$\dot{\lambda}_i = -\frac{\partial H}{\partial x_i} \tag{3.14}$$

where $\lambda_i$ is the costate corresponding to state $x_i$. For our problem, this gives

$$\dot{\lambda}_r = \lambda_\theta v_\theta / r^2 + \lambda_{v_r} v_\theta^2 / r^2 - \lambda_{v_\theta} v_r v_\theta / r^2 + 2\lambda_{v_r} \mu / r^3 \tag{3.15}$$

$$\dot{\lambda}_\theta = 0 \tag{3.16}$$

$$\dot{\lambda}_{v_r} = \lambda_{v_\theta} v_\theta / r - \lambda_r \tag{3.17}$$

$$\dot{\lambda}_{v_\theta} = \lambda_{v_\theta} v_r / r - \lambda_\theta / r - 2\lambda_{v_r} v_\theta / r \tag{3.18}$$

$$\dot{\lambda}_m = \lambda_{v_\theta} F / m^2 \tag{3.19}$$

We can simplify the costate dynamics by noting that since the terminal conditions do not depend on $\theta$ and $\dot{\lambda}_\theta = 0$ then we know that $\lambda_\theta = 0$ for all time. Therefore, the

reduced costate dynamics are

$$\dot{\lambda}_r = \lambda_{v_r} v_\theta^2/r^2 - \lambda_{v_\theta} v_r v_\theta/r^2 + 2\lambda_{v_r}\mu/r^3 \tag{3.20}$$

$$\dot{\lambda}_{v_r} = \lambda_{v_\theta} v_\theta/r - \lambda_r \tag{3.21}$$

$$\dot{\lambda}_{v_\theta} = \lambda_{v_\theta} v_r/r - 2\lambda_{v_r} v_\theta/r \tag{3.22}$$

$$\dot{\lambda}_m = \lambda_{v_\theta} F/m^2 \tag{3.23}$$

Now, all we need to implement the optimal control law are the initial costate values. Unfortunately, optimal control theory does not tell us what the initial costate values should be. However, we have managed to reduce our continuous time optimization of the control thrust over the entire trajectory to an optimization over the initial costate values - four decision variables - which dramatically reduces the complexity of the problem.

To solve the problem and find the tradeoff between escape time and propellant mass we pose the problem as a multi-objective optimization. Find the range of initial costate values with the objectives

$$\begin{aligned} \text{minimize} \quad & f_1 = \text{propellant mass} \\ & f_2 = \text{escape time} \end{aligned}$$

such that the spacecraft achieves escape. The Pareto front can be found with a genetic algorithm. Deb [17] provides a good reference on using genetic algorithms for multi-objective optimization. Figure 3-4 shows the resulting Pareto front for a minimum performance iEPS system on a 3U CubeSat starting from geostationary orbit. The points on the plot represent the result of the genetic algorithm while the black line is a second order exponential fit of the data. We can see that the tradeoff is quite poor - going from a 200 day trajectory to a 300 day trajectory only increases the payload mass by 60 grams meaning that we increase the payload mass by 0.6 grams per day that we sacrifice.

The optimization using initial costate values also means that individual data

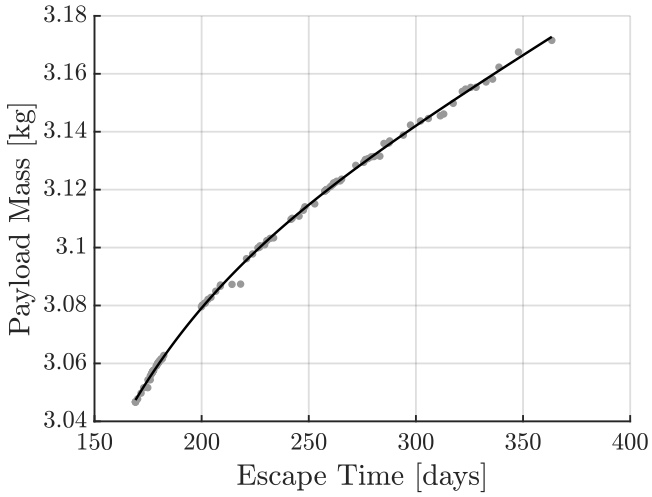


Figure 3-4: Pareto front for tradeoff in payload mass and escape time

points along the Pareto front can be simulated to see the trajectory. Figure 3-5 shows the trajectory, control thrust, and switching function for a 180 day escape trajectory along the Pareto front. Sections of the trajectory in black correspond to thruster firing while sections of the trajectory in red correspond to coasting. We can see based on the trajectory and control thrust that only a single coast arc is used. The time at which the thruster is turned off also corresponds to the time which the switching function is positive, as expected.

Figures 3-6 and 3-7 show Pareto dominant trajectories, control thrusts, and switching functions for 205 and 365 day escape trajectories. We can see that as more and more coast arcs are added, the coast arcs are concentrated around where the orbital radius of the spacecraft is highest and therefore the orbital velocity is lowest - as expected. For the cases in Figures 3-5 and 3-6 we can see that the vast majority of thrusting is done during the initial spiral up from geostationary orbit with coast arcs being added to the final revolutions of the orbit. This helps to explain why the tradeoff between payload mass and escape time is so poor. During the initial spiral, the orbit of the spacecraft is very close to being circular and therefore there is no advantage to coasting. It's only towards the end of the trajectory when the orbit becomes slightly elliptical that the spacecraft can coast to take advantage of the Oberth effect and increase the payload mass.

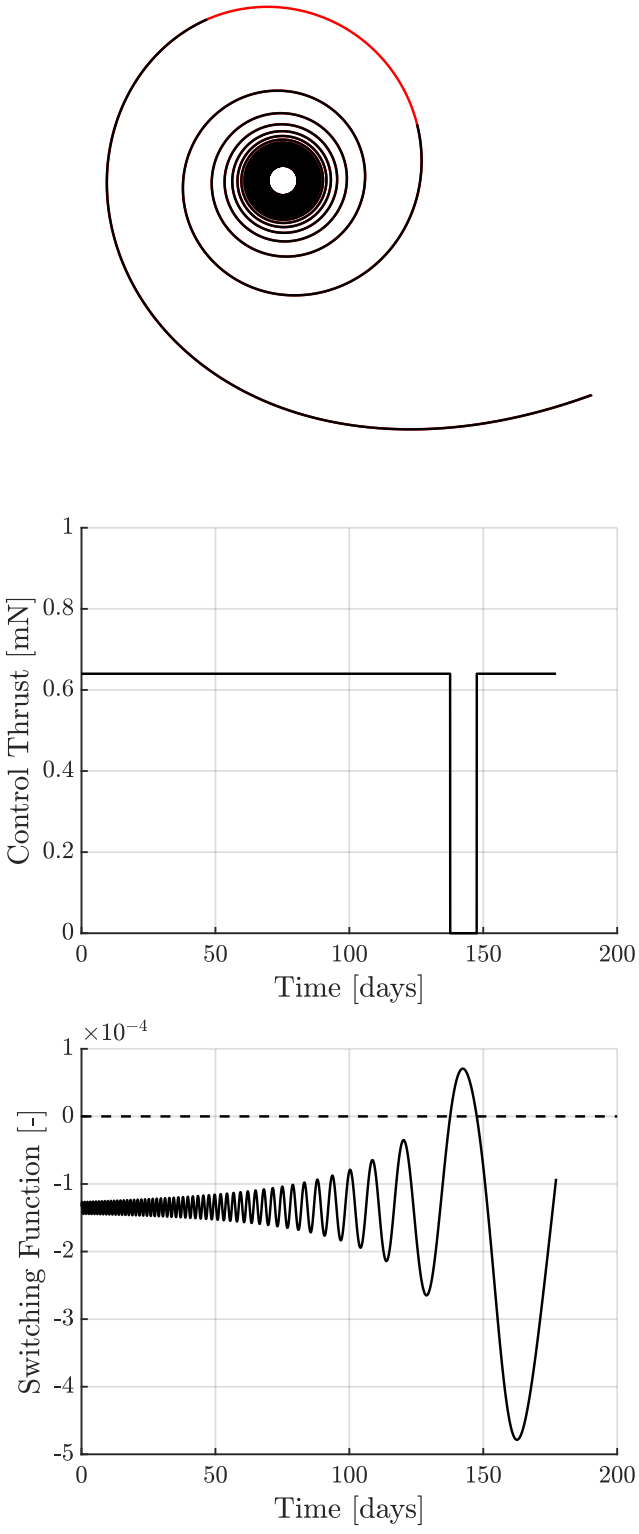


Figure 3-5: Trajectory, control thrust, and switching function for a 180 day escape trajectory along the Pareto front

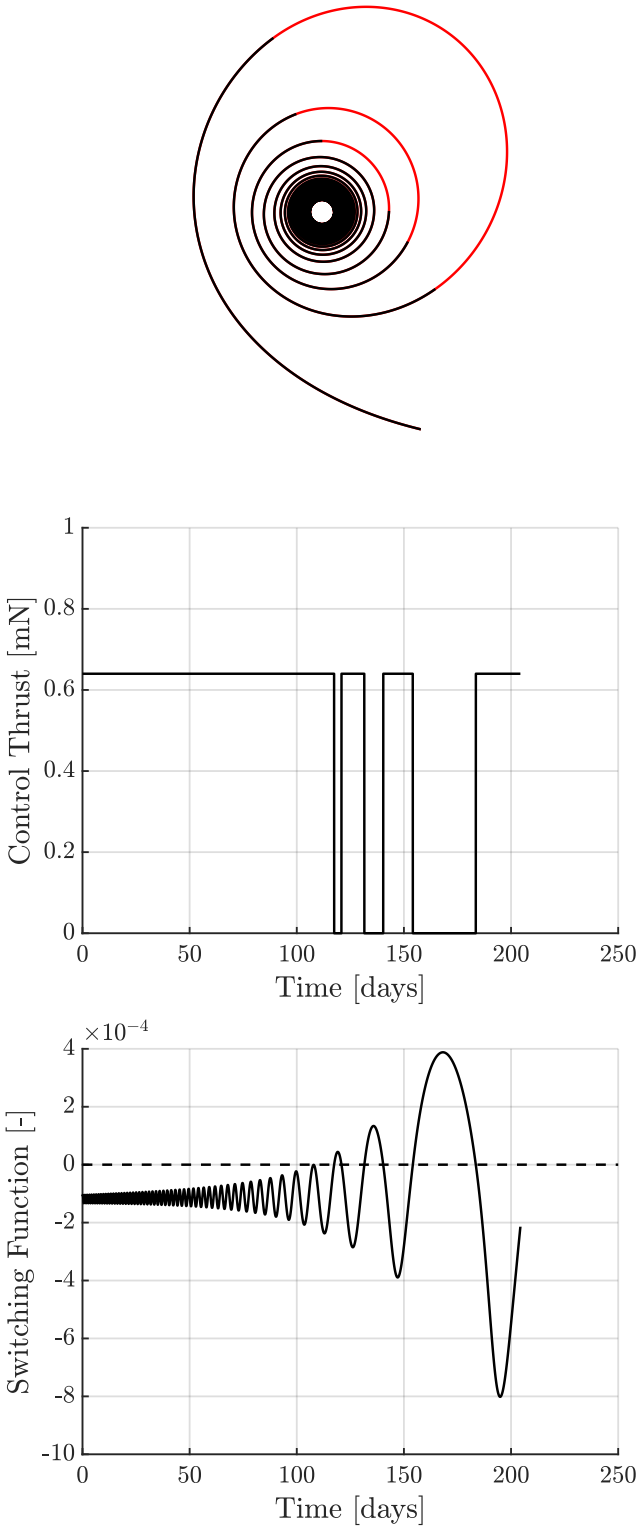


Figure 3-6: Trajectory, control thrust, and switching function for a 205 day escape trajectory along the Pareto front

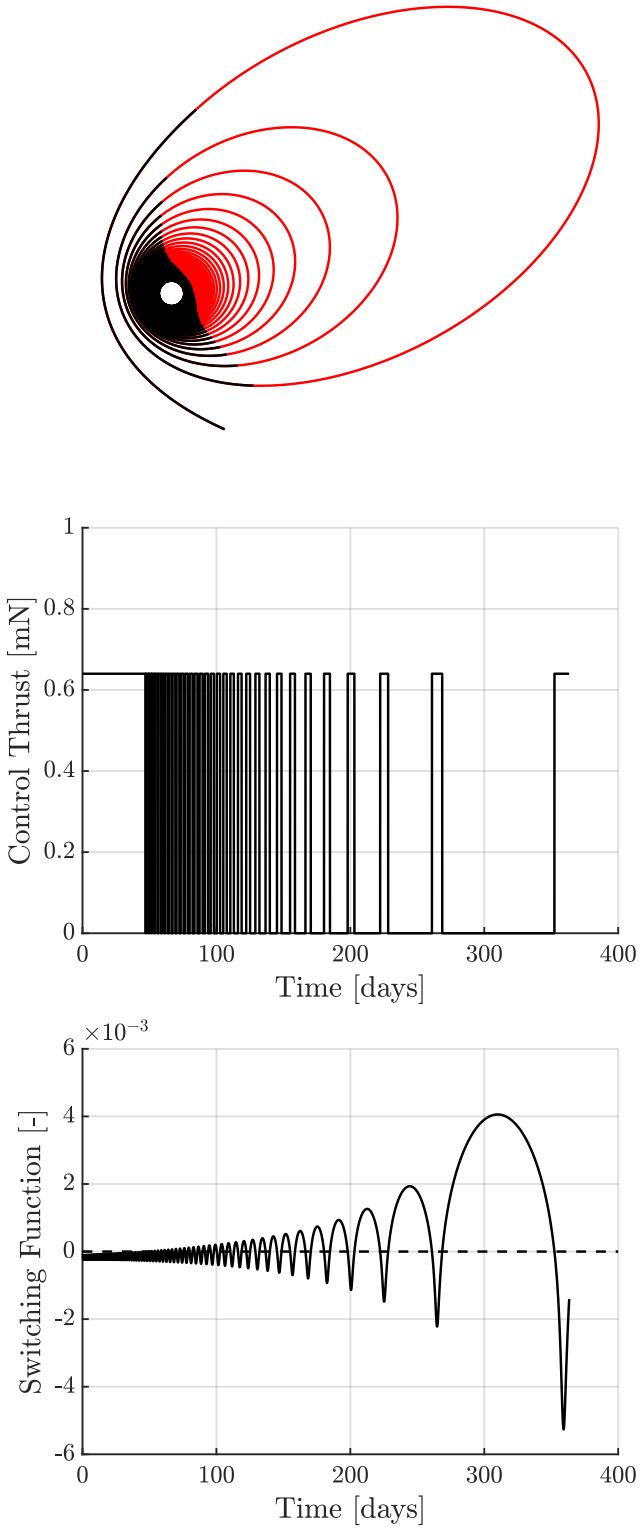


Figure 3-7: Trajectory, control thrust, and switching function for a 365 day escape trajectory along the Pareto front

This effect can also be seen in Figure 3-7. Even though coast arcs are introduced lower in the trajectory, we can see that the orbits are still fairly circular. This means that the escape time is being significantly increased due to the added coasting but the payload mass is only marginally improved since the orbit is almost circular.

Based on this analysis and the analysis in Section 3.1.1 optimizations which aim to increase the payload mass delivered to escape do not provide significant results. Therefore, for these low-thrust escape trajectories the path forward is to use an angular pointing control law, due to its simplicity, and continuous thrust with no coasting. Using such a control law dramatically decreases the complexity of designing escape trajectories. This allows us to develop good analytical approximations of the escape trajectory which can be used in analytical analyses of stage-based propulsion systems as in Section 3.2.7 or as reference trajectories for guidance during circular orbit transfers or escape as in Section 4.2.

## 3.2 Analytical Analysis of Stage-Based Systems

To analyze the impact of using a stage-based propulsion system, an analytical approach is taken. The analytical approach allows us to view the dependencies of the stage-based propulsion system performance on the parameters of the individual stages. In addition, we can provide the framework to move towards autonomous decision making on satellites with stage-based propulsion systems by providing a computationally simple method for determining propulsion system performance.

The goal of the analytical approach is to develop equations that can answer key questions about the propulsion system. Namely,

- How many stages are required for a given mission?
- What are the dependencies on propulsion system parameters?
- What is the mass and volume of the propulsion system?
- How do un-staged and staged propulsion systems compare?

- What is the probability of mission success?

The answers to these questions all stem from an approximation of the $\Delta$V of the propulsion system. We will find that we can provide a tight approximation of the true $\Delta$V of the propulsion system both in cases where mass flow is neglected and where mass flow is accounted for. In addition, the approximation of $\Delta$V will be conservative, meaning that any results derived from the approximation will bound the true result. These analytical approximations of the results can then be used in preliminary propulsion system and mission design, focusing of propulsion system technology developments, and online autonomous decision making.

### 3.2.1 $\Delta$V Approximation

Ignoring fuel mass depletion, the $\Delta$V for a stage-based propulsion system is given by

$$\Delta \mathrm{V} = \sum_{i=1}^{N} \frac{FL}{m_0 - (i-1)m_\mathrm{S}} \tag{3.24}$$

where $F$ is the propulsion system thrust, $L$ is the lifetime of each stage, $m_0$ is the initial spacecraft wet mass, and $m_\mathrm{S}$ is the dry mass for a single stage. This sum does not have an analytical solution. However, we can approximate its value by assuming that the impulse of each stage ($FL$) is applied to the average mass of the spacecraft.

$$\bar{m} = m_0 - \frac{1}{2}(N-1)m_\mathrm{S} \tag{3.25}$$

This approximation eliminates the summing index from the sum itself and allows for a simple approximation of the $\Delta$V for the whole system

$$\Delta \mathrm{V} \approx \sum_{i=1}^{N} \frac{FL}{m_0 - \frac{1}{2}(N-1)m_\mathrm{S}} = \frac{NFL}{m_0 - \frac{1}{2}(N-1)m_\mathrm{S}} \tag{3.26}$$

Figure 3-8 shows the percent error in the $\Delta$V approximation versus number of stages when compared to an exact calculation of the sum using minimum performance iEPS characteristics for a 3U CubeSat. We can see that the error is very small

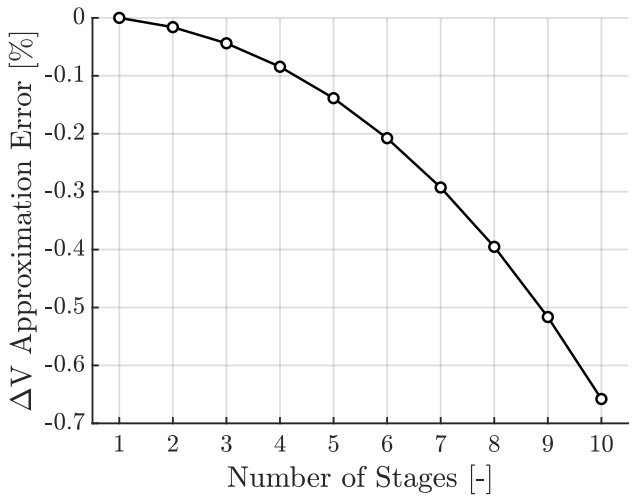


Figure 3-8: Percent error in $\Delta$V approximation versus number of stages

($< 1\%$) even for a large number of stages. Also of note is that the approximation underestimates the $\Delta$V of the system. This is important as it means that results derived from the approximation such as the number of stages required to complete a mission will be conservative estimates and bound the actual value.

The error in the sum approximation will be driven by the ratio of the dry mass of a stage, $m_{\mathrm{S}}$, to the spacecraft's initial mass, $m_0$, and is independent of propulsion system characteristics. This is not surprising as we assumed that the thrust and lifetime of each stage is identical and the variables can be pulled out of the summation. We can see this more formally by examining the ratio of incremental $\Delta$V for the analytical approximation and exact solution for a specific stage. The $\Delta$V produced by stage $i$ in the approximation is given by

$$\delta\Delta\mathrm{V}_a = \frac{FL}{m_0 - \frac{1}{2}(N-1)m_{\mathrm{S}}} \tag{3.27}$$

while the exact $\Delta$V is given by

$$\delta\Delta\mathrm{V}_e = \frac{FL}{m_0 - (i-1)m_{\mathrm{S}}} \tag{3.28}$$

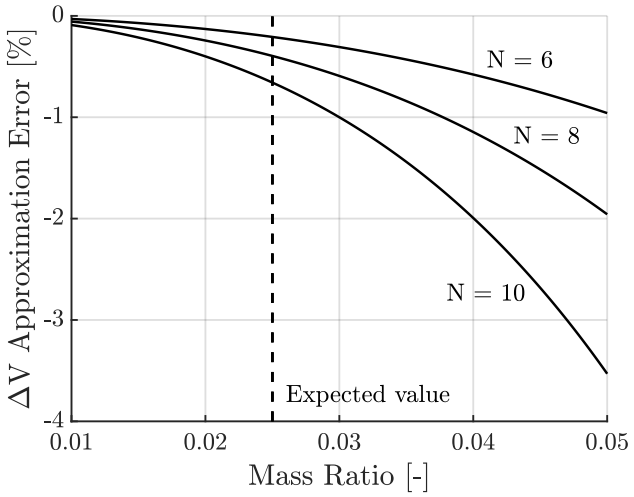


Figure 3-9: Effect of mass ratio on stage approximation error

The incremental $\Delta$V ratio can therefore be calculated as

$$\frac{\delta \Delta \mathrm{V}_a}{\delta \Delta \mathrm{V}_e} = \frac{m_0 - (i-1)m_\mathrm{S}}{m_0 - \frac{1}{2}(N-1)m_\mathrm{S}} \tag{3.29}$$

Defining the mass ratio, $\rho$, as $\rho = m_\mathrm{S}/m_0$ then the incremental ratio is

$$\frac{\delta \Delta \mathrm{V}_a}{\delta \Delta \mathrm{V}_e} = \frac{1 - (i-1)\rho}{1 - \frac{1}{2}(N-1)\rho} \tag{3.30}$$

which we can see is driven by $\rho$ for a given propulsion system. Expected values of $\rho$ for the stage-based electrospray propulsion system are $\sim 0.025$ indicating that the ratio is close to one for a modest number of stages and that the error in the approximation is small. Figure 3-9 shows the percent error in the $\Delta$V approximation versus mass ratio. We can see that increasing mass ratio or the number of stages increases the error in the approximation. However, for the expected mass ratio ($\sim 0.025$) and number of stages ($< 10$) for the stage-based electrospray propulsion system the error is always lower than 1% indicating that the approximation well captures the performance of the stage-based system.

We can extend the mass averaging technique to also account for the effects of fuel mass depletion. Assuming that each stage is identical in terms of thrust, exhaust

velocity, and lifetime, then the total fuel mass used by the system is

$$m_f = N\frac{FL}{c} \tag{3.31}$$

where $c$ is the exhaust velocity ($I_{\text{sp}}g$). Including the fuel mass in the mass average simply introduces a third term

$$\bar{m} = m_0 - \frac{1}{2}(N-1)m_{\text{S}} - \frac{1}{2}N\frac{FL}{c} \tag{3.32}$$

and allows us to approximate the system $\Delta$V accounting for fuel mass flow as

$$\Delta\text{V} \approx \frac{NFL}{m_0 - \frac{1}{2}(N-1)m_{\text{S}} - \frac{1}{2}N\frac{FL}{c}} \tag{3.33}$$

This result is consistent with our previous approximation for when fuel mass flow is negligible as we can see that in the limit of $c \to \infty$ then

$$\frac{1}{2}N\frac{FL}{c} \to 0 \tag{3.34}$$

returning us to the $\Delta$V approximation where fuel mass flow was ignored.

Figure 3-10 shows the percent error in the $\Delta$V approximation versus number of stages when accounting for fuel mass flow. We can see that the percent error is greater than in the negligible fuel mass flow case. This is to be expected as we are introducing another source of error in our mass averaging. Unlike in the negligible fuel mass flow case, characteristics of the propulsion system now impact the approximation error. The error introduced by fuel mass flow will be directly proportional to the fuel mass used. As the fuel mass is decreased, primarily through increasing the exhaust velocity, we expect the error to return to that of the negligible fuel mass flow case.

Despite the increased error when accounting for fuel mass flow, the $\Delta$V approximation is still quite close to the exact solution and, importantly, still is a conservative estimate of the $\Delta$V of the propulsion system. Therefore, the $\Delta$V approximation still captures the performance of the stage-based system and provides conservative esti-

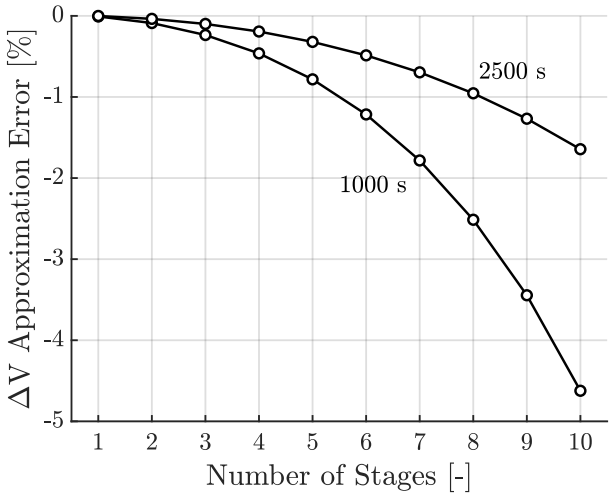


Figure 3-10: Percent error in $\Delta$V approximation versus number of stages when accounting for fuel mass flow

mates of system requirements during preliminary propulsion system design.

### 3.2.2 Approximation of Required Number of Stages

Perhaps the main figure of merit for a stage-based propulsion system is how many stages are required to complete a mission. More stages implies a larger and more massive propulsion system and can also greatly increase its complexity. Leveraging the $\Delta$V approximation from Section 3.2.1 we can analytically approximate the number of stages required to complete a mission, defined by its $\Delta$V, given propulsion and staging system parameters.

Rearranging Equation 3.33 to solve for $N$, the number of stages, gives

$$N \approx \frac{m_0 + \frac{1}{2}m_\mathrm{S}}{\frac{1}{2}m_\mathrm{S} + \frac{FL}{\Delta\mathrm{V}} + \frac{1}{2}\frac{FL}{c}} \tag{3.35}$$

In the case that fuel mass flow is negligible ($c \to \infty$) then the approximation can be reduced to

$$N \approx \frac{m_0 + \frac{1}{2}m_\mathrm{S}}{\frac{1}{2}m_\mathrm{S} + \frac{FL}{\Delta\mathrm{V}}} \tag{3.36}$$

The analytical formulation reveals the dependencies on propulsion system parameters. There are some dependencies that we expect such as increasing the thrust and/or lifetime of each stage will reduce the number of stages required to complete the mission. Perhaps counterintuitively, the dependency on exhaust velocity is such that greater exhaust velocities (usually associated with "better" propulsion system parameters) actually increases the required number of stages. This is an effect that can be seen through the mass averaging technique - a smaller exhaust velocity means more fuel mass resulting in a lower average spacecraft mass. However, this reduction of stages does not necessarily imply a reduction in propulsion system mass and volume as will be examined in Section 3.2.4.

The approximation for number of stages does permit non-integer values. In this case the last stage in the staging system is only used to some fraction of its lifetime limit. This can be useful as a safety margin where we have extra $\Delta$V we can apply to our spacecraft in the case that something goes wrong during the mission. In practice, this means that the value of $N$ that is returned from Equations 3.35 or 3.36 need to be rounded up to the next highest integer value to determine how many stages are added to the propulsion system.

Figure 3-11 shows a comparison of analytical and numerical calculations of the required number of stages for a 3U CubeSat with a minimum performance iEPS propulsion system for various $\Delta$V requirements. We can see that the analytical solution almost exactly predicts the true required number of stages. Figure 3-12 shows the same comparison of analytical and numerical calculations of the required number of stages while also accounting for the effect of fuel mass flow. We can see that the analytical solution predicts the true required number of stages quite well and begins to differ near the discrete jumps in required number of stages for higher $\Delta$V requirements. For mission design purposes, the analytical solution acts as a tight bound on the required number of stages required to complete the mission. As the exhaust velocity of the propulsion system is increased and fuel mass flow becomes more and more negligible, the bound on the required number of stages will become tighter and tighter and we will approach the negligible fuel mass solution.

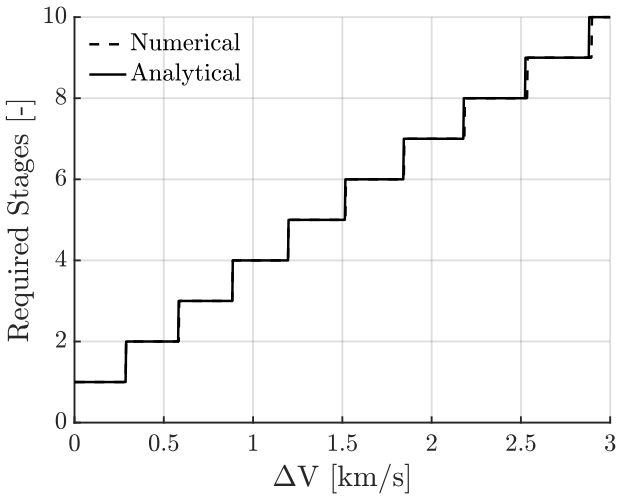


Figure 3-11: Comparison of analytical and numerical calculations of required number of stages neglecting fuel mass flow

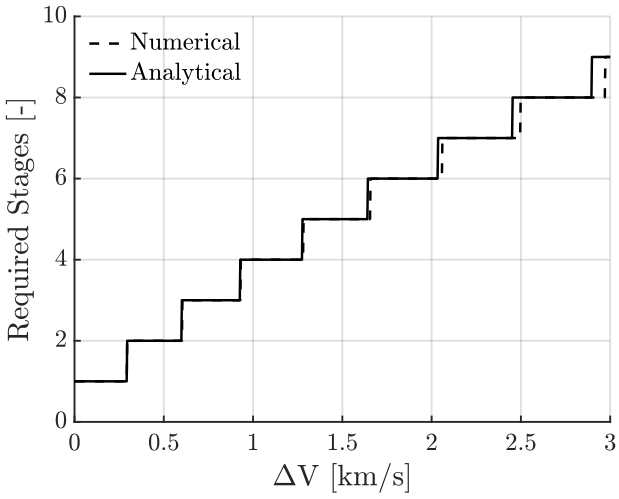


Figure 3-12: Comparison of analytical and numerical calculations of required number of stages accounting for fuel mass flow

### 3.2.3 Tradeoff in Propulsion System Parameters

While the purpose of a stage-based propulsion system is to help improve propulsion capabilities without waiting for developments in propulsion technology, we can use the analytical analysis of stage-based systems to help guide where to focus efforts in improvements for the underlying propulsion technology. Based on Equation 3.35 the thrust and lifetime of the propulsion system are the main drivers of the required number of stages and there is a weak dependence on the exhaust velocity.

For electrospray thrusters, improvements in thrust are considerably easier to achieve than improvements in lifetime. In fact, it is theoretically possible to achieve the target thrust values with the current iteration of the iEPS thrusters, but it is unclear what effect that might have on the lifetime. Therefore, knowledge of the tradeoff between thrust and lifetime for a stage-based system is valuable information and can be solved for explicitly with the analytical approximations developed above.

Starting with the approximation of the required number of stages in Equation 3.35, we can rearrange the equation to solve for thrust as a function of stage lifetime

$$F = \frac{\Delta \mathrm{V}}{NL}\left(\frac{m_0 - \frac{1}{2}(N-1)m_{\mathrm{S}}}{1+\frac{1}{2}\frac{\Delta \mathrm{V}}{c}}\right) \tag{3.37}$$

From this equation we know explicitly that for a constant number of stages

$$F \propto \frac{1}{L} \qquad \text{or} \qquad FL = \text{const.} \tag{3.38}$$

Figure 3-13 shows the required number of stages to achieve 2.5 km/s $\Delta$V with an iEPS propulsion system on a 3U CubeSat when varying thrust and stage lifetime while holding exhaust velocity constant. Both the thrust and lifetime are varied from their minimum performance value to their target performance value and normalized by the minimum performance value. The regions between lines correspond to thrust and lifetime values that lead to a given number of required stages. The analytical solution is plotted with Equation 3.37 while the numerical solution is found by posing the problem as a multi-objective optimization and solving with a genetic algorithm.

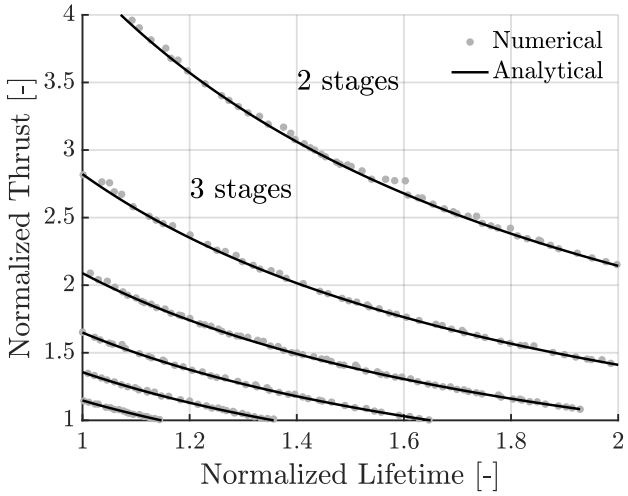


Figure 3-13: Tradeoff in required number of stages between thrust and stage lifetime neglecting fuel mass flow

For the optimization, the objectives are to minimize the required thrust and stage lifetime of the propulsion system to achieve the target $\Delta$V while holding the number of stages constant. We can see that the analytical and numerical solutions agree with no visually discernible difference between the two solutions.

Figure 3-14 shows the same scenario except accounting for fuel mass flow. The exhaust velocity of the propulsion system was held constant at the target performance value. There is still no visually discernible difference between the analytical and numerical solutions. In fact, discernible differences between the solutions only start to occur at $\Delta$V requirements of 7.5 km/s and greater. Therefore, the analytical solution provides a tight approximation of the tradeoff between thrust and lifetime for a large range of mission scenarios.

### 3.2.4 Approximation of Propulsion System Mass and Volume

With an approximation for the required number of stages, the mass and volume of the stage-based propulsion system can be estimated. The propulsion system mass is easy to estimate. The wet mass of each stage is simply the sum of the propellant

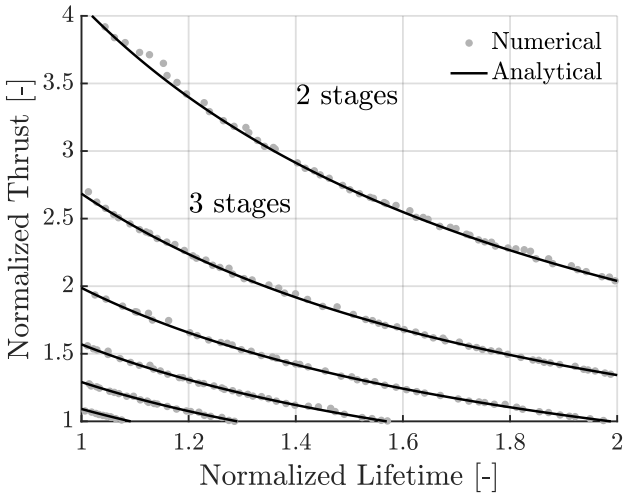


Figure 3-14: Tradeoff in required number of stages between thrust and stage lifetime accounting for fuel mass flow

mass and the dry mass

$$m_{\text{wet}} = \frac{FL}{c} + m_{\text{S}} \tag{3.39}$$

The mass of the whole propulsion system is then just the wet mass of each stage multiplied by the number of stages plus the mass of the power processing unit which is approximately 160 grams for an iEPS based system.

$$m_{\text{system}} = N\left(\frac{FL}{c} + m_{\text{S}}\right) + m_{\text{PPU}} \tag{3.40}$$

The volume of the stage-based system is trickier to estimate and is specific to the type of underlying propulsion system. To simplify the problem it is assumed that the propulsion system has a given base area, $A_{\text{system}}$, and we just need to estimate the height of the system. For a 3U system the base area will be 100 cm$^2$ (the area of one of the 10cm x 10cm faces). The height, and subsequently the volume, can then be estimated based on the type of thruster used.

For an iEPS based system we know that a stage sized for a 3U CubeSat will contain eight fuel tanks each with four thruster heads as shown in Figure 1-6. The

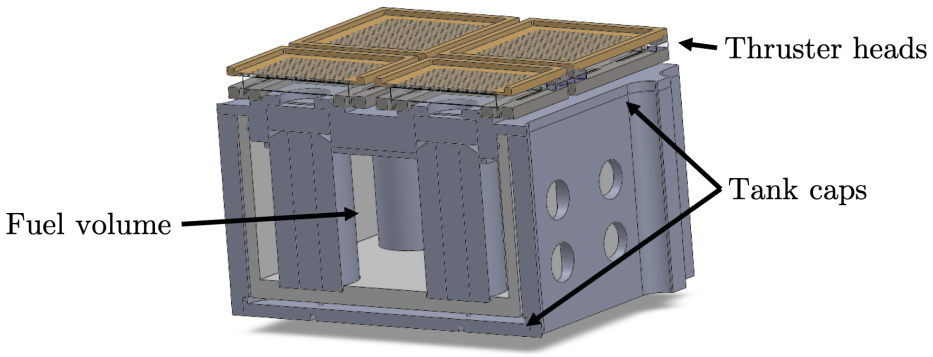


Figure 3-15: Diagram of different components contributing to the height of a thruster

height of the stage can then be calculated as

$$h_{\mathrm{S}} = h_{\text{stage board}} + 2h_{\text{tank cap}} + h_{\text{thruster head}} + h_{\text{fuel}} \tag{3.41}$$

The height of the stage board is simply the height of a typical PCB, about 1.6 mm. Tank caps represent pieces of PEEK that cap the top and bottom of the fuel tanks and are approximately 2.5 mm each. The thruster head contains the emitter chip and extractor grid and is approximately 2.5 mm. Figure 3-15 shows the different components of the thruster that contribute to the overall height.

The only value that will change from mission to mission is the height of the fuel. Given the mass of fuel used by each stage

$$m_{\text{fuel}} = \frac{FL}{c} \tag{3.42}$$

the amount of fuel in each fuel tank can be calculated as

$$m_{\text{fuel, tank}} = \frac{1}{M}\frac{FL}{c} \tag{3.43}$$

where $M$ is the number of fuel tanks on each stage, eight in our case. The volume of

fuel in each tank can then be calculated based on the density, $\rho$, of the ionic liquid used

$$V_{\text{fuel, tank}} = \frac{1}{\rho M}\frac{FL}{c} \tag{3.44}$$

A typical density for an ionic liquid propellant is around 1.5 g/cc. Finally, the height of the fuel in the tank can be calculated based on the cross-sectional area of the tank allotted to fuel, $A_{\text{fuel}}$

$$h_{\text{fuel}} = \frac{1}{\rho M A_{\text{fuel}}}\frac{FL}{c} \tag{3.45}$$

For the four thruster head tanks used in the iEPS system, the cross-sectional area for fuel is approximately 9 $\text{cm}^2$.

The height of the whole propulsion system is then the height of each stage multiplied by the number of stages plus the height of the power processing unit, 3 cm for an iEPS based system

$$h_{\text{system}} = N\left(h_{\text{stage board}} + 2h_{\text{tank cap}} + h_{\text{thruster head}} + \frac{1}{\rho M A_{\text{fuel}}}\frac{FL}{c}\right) + h_{\text{PPU}} \tag{3.46}$$

which can be used to calculate the volume of the propulsion system as

$$V_{\text{system}} = h_{\text{system}} A_{\text{system}} \tag{3.47}$$

where $A_{\text{system}}$ is the base area.

Figure 3-16 shows the mass and volume of the stage-based propulsion system compatible with a 3U form factor for various number of stages where the underlying propulsion is assumed to be minimum performance iEPS thrusters. We can see that for a large number of stages (8-10) the mass and volume are fairly constraining but not so far as to prevent missions from being possible. A nine stage system which would enable deep-space missions to near-Earth asteroids allows for a 1.9 kg payload with a volume of 0.9U, close to the size and weight of an overweight 1U CubeSat. As

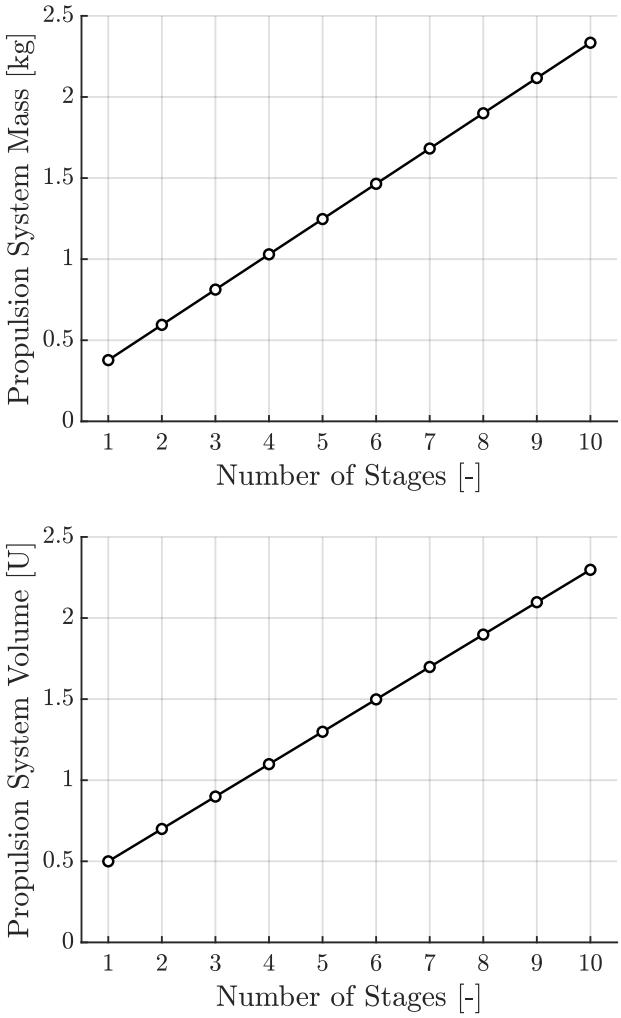


Figure 3-16: Mass and volume of a stage-based propulsion system compatible with the 3U CubeSat form factor based on minimum performance iEPS thrusters

the underlying propulsion technology matures, less stages will be required for a given mission which will reduce the mass and volume of the propulsion system.

### 3.2.5 Comparison of Un-staged and Staged Firing Times

The $\Delta$V approximation can also be used to compare the amount of firing time required to complete a mission for a stage-based propulsion system versus a more traditional, un-staged, system. Stage-based propulsion systems are used to enable missions which cannot be done with current propulsion technology. However, they also influence the resulting trajectory and this influence needs to be considered when designing

missions. Here, we are interested in comparing the firing times for staged versus un-staged missions in order to understand how the mission time is impacted by the use of a stage-based propulsion system.

Neglecting fuel mass flow, the firing time for an un-staged trajectory, $T_{\mathrm{u}}$, is

$$T_{\mathrm{u}} = \frac{\Delta \mathrm{V}}{F/m_0} \tag{3.48}$$

The firing time for a staged trajectory is

$$T_{\mathrm{s}} = NL \tag{3.49}$$

where $N$ is the number of stages and $L$ is the lifetime of each stage. We can use our approximation for the required number of stages in Equation 3.36 to write the firing time in terms of the $\Delta$V and propulsion system parameters as

$$T_{\mathrm{s}} = \frac{m_0 + \frac{1}{2}m_{\mathrm{S}}}{\frac{1}{2}m_{\mathrm{S}} + \frac{FL}{\Delta \mathrm{V}}} L \tag{3.50}$$

The ratio of firing time for a stage-based propulsion system versus an un-staged propulsion system, $\tau$, is therefore

$$\tau = \frac{T_{\mathrm{s}}}{T_{\mathrm{u}}} = \frac{1 + \frac{1}{2}\frac{m_{\mathrm{S}}}{m_0}}{1 + \frac{1}{2}\frac{\Delta \mathrm{V} m_{\mathrm{S}}}{FL}} \tag{3.51}$$

A similar, less compact, equation can be developed for accounting for mass flow. With mass flow, the firing time for an un-staged trajectory is

$$T_{\mathrm{u}} = \frac{m_0 c}{F}\left(1 - e^{-\Delta \mathrm{V}/c}\right) \tag{3.52}$$

The firing time for the staged trajectory can be estimated with the required number of stages from Equation 3.35 as

$$T_{\mathrm{s}} = NL = \frac{m_0 + \frac{1}{2}m_{\mathrm{S}}}{\frac{1}{2}m_{\mathrm{S}} + \frac{FL}{\Delta \mathrm{V}} + \frac{1}{2}\frac{FL}{c}} L \tag{3.53}$$

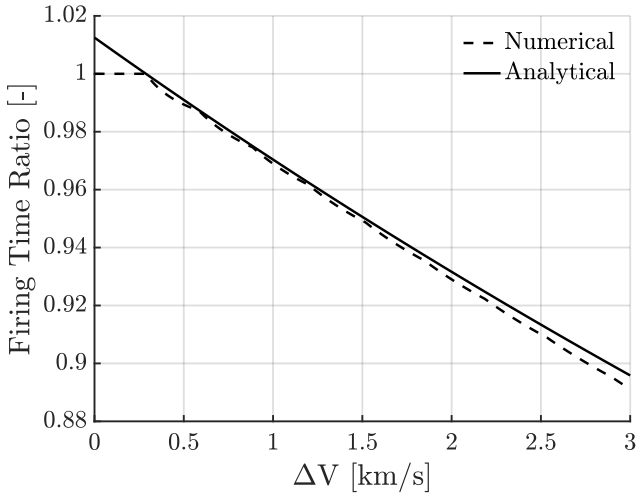


Figure 3-17: Ratio of firing times for staged to un-staged propulsion systems neglecting fuel mass flow

Calculating the firing time ratio, $\tau$, in this case gives

$$\tau = \frac{1}{1 - e^{-\Delta V/c}} \left( \frac{1 + \frac{1}{2}\frac{m_S}{m_0}}{\frac{1}{2} + \frac{1}{2}\frac{m_S c}{FL} + \frac{c}{\Delta V}} \right) \tag{3.54}$$

Figure 3-17 shows the ratio of firing times for staged to un-staged propulsion systems when neglecting fuel mass flow. The spacecraft was a 3U CubeSat carrying a minimum performance iEPS propulsion system. We can see that the analytical solution predicts the true numerical ratio quite well with a $\sim$0.5% error at 3 km/s of $\Delta$V which is in line with our predicted $\Delta$V error from Section 3.2.1. Figure 3-18 shows the same situation but while accounting for fuel mass flow. We can see that the deviation between the analytical and numerical solutions is larger than in the negligible fuel mass flow case. However, the error is still only $\sim$1% at 3 km/s of $\Delta$V which is lower than the expected $\Delta$V error that we saw in Section 3.2.1.

In both cases, neglecting or accounting for fuel mass flow, we notice that at low $\Delta$V requirements ($<$ 300 m/s), the analytical solution predicts that the stage propulsion system actually requires more firing time than the un-staged system. This is an artifact from the mass averaging technique when estimating the $\Delta$V of the staged propulsion system in Section 3.2.1. The mass averaging technique treats the stage-

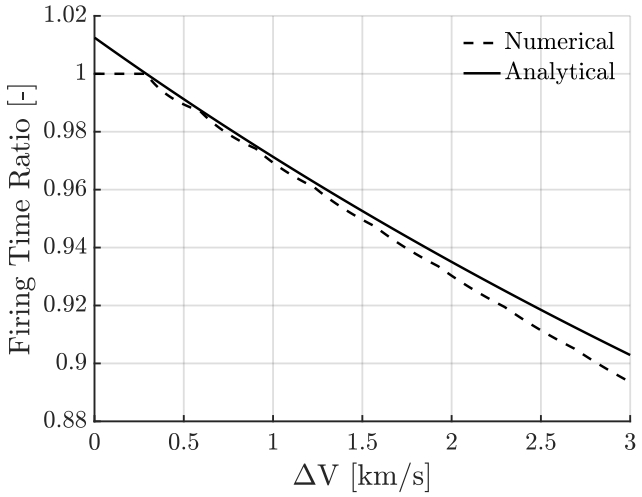


Figure 3-18: Ratio of firing times for staged to un-staged propulsion systems accounting for fuel mass flow

based system as an un-staged system that acts on the average mass of the spacecraft

$$\bar{m} = m_0 - \frac{1}{2}(N-1)m_S \tag{3.55}$$

In the situation that $N < 1$, which occurs when the mission can be completed in only a fraction of the lifetime of a single stage, we notice that the mass average is actually greater than the initial mass of the spacecraft, $m_0$. This causes the subsequent approximations of firing time to be artificially inflated when, in reality, they should exactly equal the un-staged system's firing times.

### 3.2.6 Mission Success Probability

Throughout the previous analysis it was assumed that the lifetime of a stage was known exactly. However, this is not true to reality - the lifetime of a propulsion system, and therefore of a stage, can have a significant degree of uncertainty. When the lifetime of the stages is uncertain, then the $\Delta V$ produced by the propulsion system will also be impacted. If the lifetimes are distributed by any symmetric distribution around the predicted lifetime and we size the propulsion system based on Equation 3.35, then we only have a 50% probability that the propulsion system will actually

produce the $\Delta$V required to complete the mission. Therefore, we are interested in calculating the distribution of $\Delta$V based on distributions in the lifetime of the stages.

Returning to the $\Delta$V of the propulsion system before the mass average approximation, the $\Delta$V of a stage-based propulsion system is

$$\Delta \mathrm{V} = F \sum_{i=1}^{N} \frac{t_i}{m_0 - (i-1)m_{\mathrm{S}}} \tag{3.56}$$

Assuming that the firing times of each stage will be symmetrically distributed about a single mean value, then we can still use the mass averaging technique except the mass average here is the averaged time averaged mass.

$$\bar{m} = m_0 - \frac{1}{2}(N-1)m_{\mathrm{S}} \tag{3.57}$$

While this approximation will be close to the true time averaged mass of the spacecraft, care will have to be taken when the distribution of the stage lifetimes is very wide and the firing times between stages varies significantly. With the time averaged mass then the sum becomes only dependent on the firing times of the stages

$$\Delta \mathrm{V} = \frac{F}{\bar{m}} \sum_{i=1}^{N} t_i \tag{3.58}$$

where the time averaged mass has been left as $\bar{m}$ to allow for the possibility of adjusting the approximation to account for fuel mass flow.

Assuming that the lifetime of each stage is distributed with a normal distribution

$$L_{\mathrm{S}} \sim N(L, \sigma_L^2) \tag{3.59}$$

then the distribution of the $\Delta$V of the propulsion system will also be normally dis-

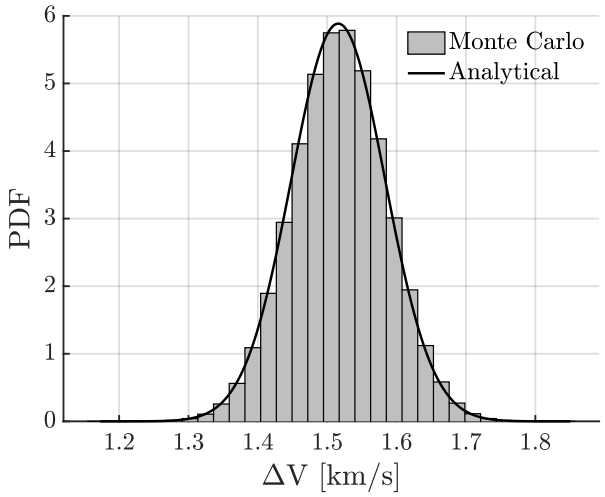


Figure 3-19: ΔV distribution for a stage-based system neglecting fuel mass flow

tributed with statistics

$$\mu = \frac{F}{\bar{m}} NL \tag{3.60}$$

$$\sigma = \frac{F}{\bar{m}} \sqrt{N} \sigma_L \tag{3.61}$$

Figure 3-19 shows a comparison of the analytical calculation of the ΔV distribution for a five stage, minimum performance, iEPS-based propulsion system on a 3U CubeSat versus a Monte Carlo analysis of the true distribution when neglecting fuel mass flow. The statistics of the stage lifetime were assumed to have a mean of the minimum performance expected iEPS lifetime and standard deviation of 50 hours. We can see that the analytical distribution is a good fit for the underlying distribution found through Monte Carlo analysis. Figure 3-20 shows the same situation but when accounting for fuel mass flow. The analytical approximation of the distribution still acts as a fairly good fit for the Monte Carlo analysis but has a slight negative shift of the mean and a slightly smaller standard deviation. As fuel mass flow becomes more and more negligible, the analytical solution will better fit the Monte Carlo analysis.

With the analytical approximation of the ΔV distribution, the probability of mission success can be approximated. Assuming that a 99.9% probability of mission success is desired, the cutoff ΔV can be calculated as three standard deviations away

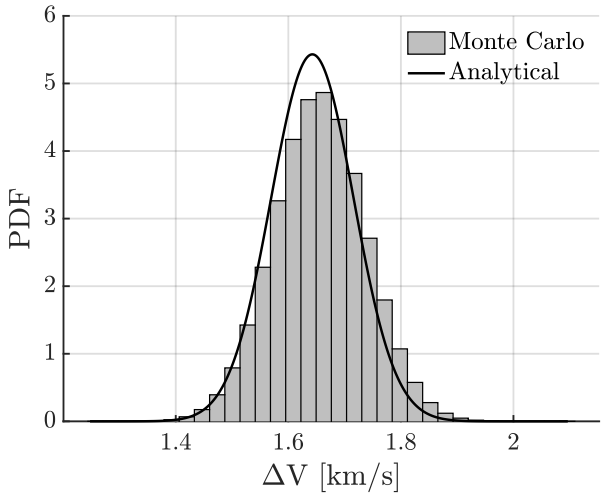


Figure 3-20: $\Delta$V distribution for a stage-based system accounting for fuel mass flow

from the mean.

$$\Delta \mathrm{V}^* = \frac{F}{\bar{m}} \left( NL - 3\sqrt{N}\sigma_L \right) \tag{3.62}$$

For any missions with $\Delta \mathrm{V} \leq \Delta \mathrm{V}^*$ the mission will have a 99.9% probability of success.

The approximation of $\Delta$V distributions can also be used to help determine when to eject a partially degraded stage. It is possible during the course of a mission, particularly with an array of electrospray thrusters, that instead of an entire stage dying, its thrust is simply reduced by some factor. For electrospray propulsion system considered here which has 32 thruster heads on a single stage, this situation would be representative of a few thruster heads having lower lifetimes than the rest of the stage. Alternatively, it might represent component failure in the electronics or a stage that starts with an abnormally low thrust.

In all representations, we consider the case that during the course of the mission, the thrust of a particular stage $n$ suddenly drops from its nominal thrust, $F$, to a degraded thrust $\eta F$, $\eta \in (0, 1)$, at some time $t_n^-$ into its firing time. From a $\Delta$V perspective it is never advantageous to eject a partially degraded stage - the stage still has the capability to provide $\Delta$V to the mission. However, from a time perspective a partially degraded stage should be ejected immediately as lower thrusts corresponds

to longer firing times for a given mission. To resolve this dispute, we view the problem instead from the perspective of mission success probability: how long do we need to keep the partially degraded stage to guarantee 99.9% probability of mission success? Such a solution balances the need to provide enough $\Delta$V to complete the mission with the desire to not operate with reduced thrust.

Assuming that the thrust reduction occurs on stage $n$ then we know the $\Delta$V produced by stages 1 to $n-1$, $\Delta V_{1:n-1}$, is

$$\Delta V_{1:n-1} = F \sum_{i=1}^{n-1} \frac{t_i}{m_0 - (i-1)m_S} \tag{3.63}$$

which is a known value and does not require approximation. Given that the thrust reduction occurs some time, $t_n^-$, into the firing time of stage $n$ then the $\Delta$V produced by stage $n$ prior to the failure, $\Delta V_n^-$, is

$$\Delta V_n^- = \frac{F\ t_n^-}{m_0 - (n-1)m_S} \tag{3.64}$$

and is known. The $\Delta$V for the remaining stages in the system, $\Delta V_{n+1:N}$, is unknown and is a random variable. However, the cutoff $\Delta V^*$ from Equation 3.62 can be used to determine what the minimum value of $\Delta V_{n+1:N}$ will be in 99.9% of scenarios. Therefore, in the "worst-case" scenario, we know that $\Delta V_{n+1:N}$ is given by

$$\Delta V_{n+1:N} = \frac{F}{\bar{m}_{n+1:N}} \left( (N-n)L - 3\sqrt{N-n}\ \sigma_L \right) \tag{3.65}$$

where the time averaged spacecraft mass averaged over the remaining stages is

$$\bar{m}_{n+1:N} = m_0 - \frac{1}{2}(N+n-1)m_S \tag{3.66}$$

when fuel mass is neglected and is

$$\bar{m}_{n+1:N} = m_0 - \frac{1}{2}(N+n-1)m_S - \frac{1}{2}(N-n)\frac{FL}{c} \tag{3.67}$$

when fuel mass is accounted for. Therefore, given a desired $\Delta V$, $\Delta V_d$, the $\Delta V$ that the reduced thrust stage needs to produce, $\Delta V_n^+$, in order to guarantee 99.9% probability of mission success is

$$\Delta V_n^+ = \Delta V_d - \Delta V_{1:n-1} - \Delta V_n^- - \Delta V_{n+1:N} \tag{3.68}$$

which can be used to calculate the required firing time as

$$t_n^+ = \frac{m_0 - (n-1)m_S}{\eta F} \Delta V_n^+ \tag{3.69}$$

There are three regimes of value that $t_n^+$ can take. If $t_n^+ \leq 0$, then stage $n$ can safely be ejected. If $0 < t_n^+ \leq t^*$, where $t^*$ is a reasonably low firing time that we can expect the reduced thrust stage to be capable of firing for, then the stage can be kept and we can still expect a mission success probability of 99.9%. However, if $t_n^+ > t^*$, then it's unlikely that the reduced thrust stage will be able to produce $\Delta V_n^+$ and the mission success probability will be lower than 99.9%. The exact calculation of $t^*$ will be highly dependent on the system as it will have to take into account coupling between the failure already observed on the stage and potential future failures as well as the potential that further discrete drops in thrust may occur on the same stage. However, this analysis provides the framework for potential autonomous decision making regarding when to eject partially failed stages on spacecraft equipped with stage-based propulsion systems.

For an example scenario, a five stage propulsion system with minimum performance iEPS characteristics on a 3U CubeSat is desired to produce 1,250 m/s of $\Delta V$. It is assumed that the lifetime of each stage is distributed with the mean at the expected minimum lifetime of iEPS thrusters and standard deviation of 50 hours. The first stage in the system is allowed to fire for 100 hours at nominal thrust levels before experiencing a partial failure which causes a thrust reduction of 25%. Two situations are analyzed through Monte Carlo analysis with 1e6 samples each: the first stage is ejected immediately after experiencing the partial failure (immediate eject) and the first stage is fired at its reduced thrust level for a firing time based on Equation 3.69

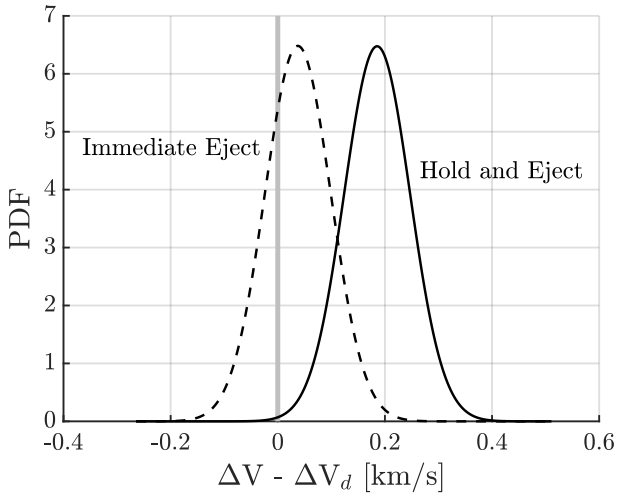


Figure 3-21: Effect of holding partially failed stage before ejecting on ΔV distribution of the entire propulsion system

before ejection (hold and eject).

Figure 3-21 shows the resulting propulsion system ΔV distributions of both situations. We can see clearly that in the immediate eject situation the mission does not have a 99.9% probability of success and a substantial portion of the distribution is below $\Delta V_d$. In fact, the numerical estimate of success probability is only 72.8%. However, in the hold and eject situation, the distribution is shifted such that the vast majority of the distribution is greater than $\Delta V_d$. Numerically, the probability of success is estimated at 99.9%. In this scenario, to achieve 99.9% probability of success, the first stage was required to fire for 342 hours at reduced thrust level. This brings the total firing time of the first stage to 442 hours which, based on the statistics of the stage lifetimes, has a 84% chance of occurring.

### 3.2.7 Application to Escape Trajectories

To specialize the analytical methods developed above to escape trajectories, we first need to estimate the required ΔV to achieve escape. In Section 3.1 we settled on using a continuous thrust angular pointing control law for the escape spiral. Good analytical approximations for the state of the spacecraft during the escape trajectory with such a control law can be developed. Appendix A derives such an approximation

based on the change in specific energy of the orbit due to the applied propulsive acceleration. Here, we will extend the approximation to estimate the $\Delta$V required to achieve escape.

The specific energy of the orbit, $\epsilon$, is given by

$$\epsilon = \frac{1}{2}v_r^2 + \frac{1}{2}v_\theta^2 - \frac{\mu}{r} \tag{3.70}$$

where $v_r$ is the radial velocity, $v_\theta$ is the velocity in the angular direction, $\mu$ is the gravitational parameter of Earth, and $r$ is the radial position. Continuing the circular orbit approximation from the derivation in Appendix A then the specific energy can be approximated as

$$\epsilon = \frac{1}{2}v_r^2 - \frac{1}{2}v_\theta^2 \tag{3.71}$$

Therefore, we know that at escape when $\epsilon = 0$, $v_r = v_\theta$.

Using the approximations for $v_r$ and $v_\theta$ in Equations A.14 and A.15 respectively, then the escape condition is

$$\frac{2r_0 a_\mathrm{p}/v_0}{\left(1 - \frac{a_\mathrm{p}}{v_0}t_\mathrm{esc}\right)^3} = v_0\left(1 - \frac{a_\mathrm{p}}{v_0}t_\mathrm{esc}\right) \tag{3.72}$$

where $r_0$ is the initial orbital radius, $a_\mathrm{p}$ is the propulsive acceleration, $v_0$ is the initial orbit velocity, and $t_\mathrm{esc}$ is the time at which escape is achieved. The equation can be rearranged to solve for the escape time as

$$t_\mathrm{esc} = \frac{v_0}{a_\mathrm{p}}\left[1 - (2\gamma)^{1/4}\right] \tag{3.73}$$

where $\gamma$ is the ratio of the propulsive acceleration, $a_p$, to the gravitational acceleration at the start of the trajectory, $\mu/r_0^2$. While the approximation for the escape time is quite good, it can be improved based on numerical results. Solving for the scalar

Table 3.1: Escape time scalar factor for various acceleration ratios

| $\gamma$ | Angular Pointing | Velocity Pointing |
|---|---|---|
| 1e-2 | 0.7551 | 0.8053 |
| 1e-3 | 0.7554 | 0.8081 |
| 1e-4 | 0.7555 | 0.8082 |
| 1e-5 | 0.7555 | 0.8082 |

factor, $2^{1/4}$, and assigning the variable $S$, we have

$$S = \frac{1 - \frac{a_\mathrm{p}}{v_0} t_\mathrm{esc}}{\gamma^{1/4}} \tag{3.74}$$

Table 3.1 shows the scalar factor for various acceleration ratios based on numerical propagation of the escape trajectories for both angular pointing and velocity pointing control laws. We can see that in both cases, the scalar factor is fairly constant and converges to a value as $\gamma$ is decreased. For reference, a minimum performance iEPS based system on a 3U CubeSat starting in geostationary orbit has a $\gamma$ of 7e-4. Based on the numerical results, a better approximation for the escape time is

$$t_\mathrm{esc} = \frac{v_0}{a_\mathrm{p}} \left[1 - S\gamma^{1/4}\right] \tag{3.75}$$

where $S = 0.7555$ for an angular pointing control law and $S = 0.8082$ for a velocity pointing control law. The required $\Delta$V for escape can then be calculated as

$$\Delta \mathrm{V}_\mathrm{esc} = a_\mathrm{p} t_\mathrm{esc} = v_0 \left[1 - S\gamma^{1/4}\right] \tag{3.76}$$

With an analytical estimate for $\Delta \mathrm{V}_\mathrm{esc}$ we can now use the analytical approximations developed previously to evaluate a stage-based electrospray propulsion system for a 3U CubeSat to achieve escape from geostationary orbit.

A minimum performance iEPS based system starting in geostationary orbit will have an acceleration ratio, $\gamma$, of 7e-4 which gives a required $\Delta$V to achieve escape of approximately 2.7 km/s. Using Equation 3.35, 7.5 stages will be required to produce that $\Delta$V which means the propulsion system will consist of 8 stages. Therefore, the

Table 3.2: Performance of stage-based propulsion system for escape for minimum and target iEPS performance metrics

| | Minimum | Target |
|---|---|---|
| $\Delta$V | 2.7 km/s | 2.5 km/s |
| Stages | 7.5 | 1.05 |
| Mass | 1.9 kg | 1.3 kg |
| Volume | 1.9U | 1.2U |
| Escape time | 157 days | 44 days |

propulsion system will have a mass of 1.9 kg and a volume of 1.9U leaving 2.1 kg and 1.1U for the payload allowing for a small, but feasible, mission. If target performance values for the iEPS system can be achieved, then the acceleration ratio increases to 3e-3. This slightly drops the required $\Delta$V for escape to 2.5 km/s. However, the improvements in thrust and lifetime for the target performance metrics mean only 1.05 stages are required for the mission. This means that the propulsion system will consist of 2 stages but the second stage will only be used lightly during the escape providing significant extra $\Delta$V capability for an extended mission. The 2 stage propulsion system has a mass of 1.3 kg and a volume of 1.2U leaving 2.7 kg and 1.8U for the payload.

## 3.3 Optimization of Stage-Based Systems

In Section 3.1 we considered two methods of optimization for escape trajectories: different control laws and adding coast arcs. Neither form of optimization proved significant. In particular, the optimization with coast arcs aimed to examine the tradeoff between payload mass and escape time by potentially sacrificing escape time to improve the payload mass delivered to escape but showed that only marginal improvements in payload mass were possible for significant increases in escape time.

The use of a stage-based propulsion system provides a new avenue for optimization. For a given stage-based system we can optimize the firing time of each stage in order to minimize the total firing time for a mission. Since a stage-based system drops dry mass throughout the trajectory we will find that backloading the firing time and using

the first stage as little as possible can reduce the total time of the mission - potentially by a few days for high $\Delta$V missions like escape. However, this form of optimization comes at the cost of sacrificing robustness by ejecting a functioning stage early on in the mission.

### 3.3.1 Optimization of Stage Timings

In the standard implementation of a stage-based propulsion system we use each stage until the end of its life before ejecting it and using the next stage. If the propulsion system has been sized correctly, then the firing time of the last stage in the stack will be some fraction of its maximum lifetime. However, this is quite likely not the optimal distribution of firing time to each stage if we are trying to minimize total mission time. Intuitively, if each stage has the same thrust and we want to minimize the total firing time to achieve a certain $\Delta$V, then we would want to concentrate our firing time where the mass of the spacecraft is lowest. In this case we would backload all of the firing time and attempt to use the earlier stages as little as possible.

We can formalize this problem as an optimization for an $N$ stage system. The objective is to minimize the total firing time of the propulsion system

$$\min_{t_i} f = \sum_{i=1}^{N} t_i \tag{3.77}$$

subject to the constraints that the system must produce a desired $\Delta$V

$$F \sum_{i=1}^{N} \frac{t_i}{m_0 - (i-1)m_{\mathrm{S}}} = \Delta\mathrm{V} \tag{3.78}$$

and that the firing time of each stage must be less than or equal to its lifetime

$$t_i \leq L, \quad \forall i \in [1, N] \tag{3.79}$$

We can see that this problem is actually a linear program - the objective and constraint are all linear functions of the decision variables $t_i$. Therefore, we can

leverage known qualities of linear programs to solve this problem. Specifically, for a linear program with $D$ decision variables the optimal solution exists at a corner point, where a corner point is defined as the intersection of $D$ constraints. For our problem since we have $N$ stages and therefore $N$ decision variables, we know that exactly $N$ of the constraints will be satisfied. Since we have $N+1$ constraints, then only one of the constraints will be inactive.

The $\Delta$V constraint has to be active for this to be a meaningful problem to solve. Therefore, the firing time of $N-1$ of the stages is exactly the lifetime of the stage and the firing time of one of the stages is free. Assume that the firing time of stage $n \in [1, N]$ is free. Then we can analytically solve the optimization problem by forming the Lagrangian

$$L = \sum_{i=1}^{N} t_i + \sum_{i=1}^{N} \lambda_i (t_i - L) + \lambda_{N+1} \left( F \sum_{i=1}^{N} \frac{t_i}{m_0 - (i-1)m_{\mathrm{S}}} - \Delta \mathrm{V} \right) \tag{3.80}$$

where $\lambda_n = 0$ as the inequality constraint on stage $n$ is inactive. Taking the partial derivative of the Lagrangian with respect to each decision variable we get

$$\frac{\partial L}{\partial t_i} = 1 + \lambda_i + \frac{\lambda_{N+1} F}{m_0 - (i-1)m_{\mathrm{S}}} = 0 \tag{3.81}$$

Since we know that $\lambda_n = 0$ then

$$\frac{\partial L}{\partial t_n} = 1 + \frac{\lambda_{N+1} F}{m_0 - (n-1)m_{\mathrm{S}}} = 0 \tag{3.82}$$

which allows us to solve for $\lambda_{N+1}$

$$\lambda_{N+1} = -\frac{m_0 - (n-1)m_{\mathrm{S}}}{F} \tag{3.83}$$

then for any stage $j \neq n$ the partial derivative becomes

$$\frac{\partial L}{\partial t_j} = 1 + \lambda_j - \frac{m_0 - (n-1)m_{\mathrm{S}}}{m_0 - (j-1)m_{\mathrm{S}}} = 0 \tag{3.84}$$

solving for $\lambda_j$

$$\lambda_j = \frac{m_0 - (n-1)m_S}{m_0 - (j-1)m_S} - 1 \tag{3.85}$$

Dual feasibility from the Karush-Kuhn-Tucker conditions for optimality requires that the Lagrange multipliers for active inequality constraints be greater than zero. Applying this condition to Equation 3.85 then we know that

$$\frac{m_0 - (n-1)m_S}{m_0 - (j-1)m_S} > 1, \quad \forall j \neq n \tag{3.86}$$

This condition can only be satisfied if $n < j$. Therefore, we know that for the stage firing times to be optimal $n = 1$ which means that the first stage is fired as little as possible in order to meet the $\Delta$V requirement.

We can verify this result numerically by solving the problem with a linear programming solver. For the propulsion system the characteristics are those of the minimum performance case for the iEPS system on a 3U CubeSat. The required number of stages is determined using Equation 3.36 for a 2 km/s $\Delta$V mission. Figure 3-22 shows the optimal firing time for each stage where the firing time is normalized by the maximum lifetime. We can see that for all stages other than the first, the firing time is equal to the stage lifetime. For the first stage, the firing time is reduced to the minimum value possible such that the $\Delta$V constraint is met.

### Optimality of the Solution

While backloading the firing time and minimizing usage of the first stage is optimal, such a strategy is implicitly discarding energy that could be used to propel the spacecraft. Therefore, it is natural to ask how much the firing time is reduced by optimally distributing the firing time of each stage versus taking the more conservative approach and using each successive stage up to its lifetime limit. The incremental advantage of reducing the firing time of the first stage and increasing the firing time of the last

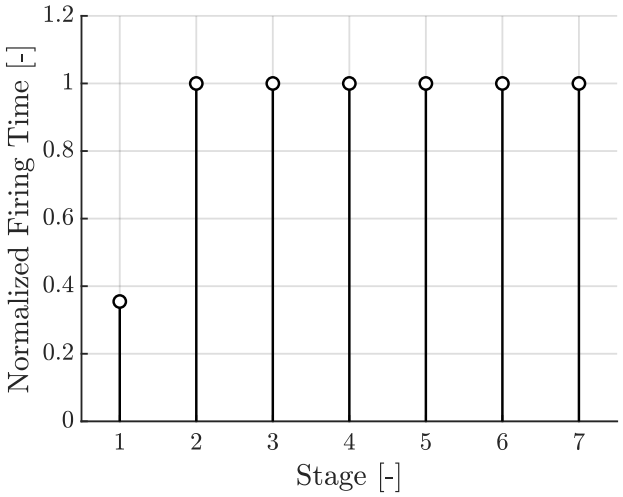


Figure 3-22: Optimal firing time distribution to each stage

stage can be seen directly from the Lagrange multiplier for the last stage

$$\lambda_N = \frac{m_0}{m_0 - (N-1)m_{\mathrm{S}}} - 1 \tag{3.87}$$

The Lagrange multiplier explicitly gives the sensitivity of the cost, the total firing time, to changes in the lifetime of the last stage

$$\frac{\partial f}{\partial t_N} = -\lambda_N \tag{3.88}$$

As the problem is linear, we know that finite changes in the firing time will directly correspond to finite changes in the total firing time

$$\frac{\Delta f}{\Delta t_N} = -\lambda_N \tag{3.89}$$

For our 3U CubeSat with a minimum performance iEPS propulsion system providing 2 km/s of $\Delta$V, $\lambda_N = 0.18$. For every hour of firing time that is shifted from the first stage to the last stage, the total firing time of the propulsion system is reduced by 0.18 hours. Given that each stage has a maximum lifetime of 500 hours in the minimum performance case, this corresponds to a maximum savings of 90 hours of firing time - a fairly modest improvement given that the total firing time for the mission is

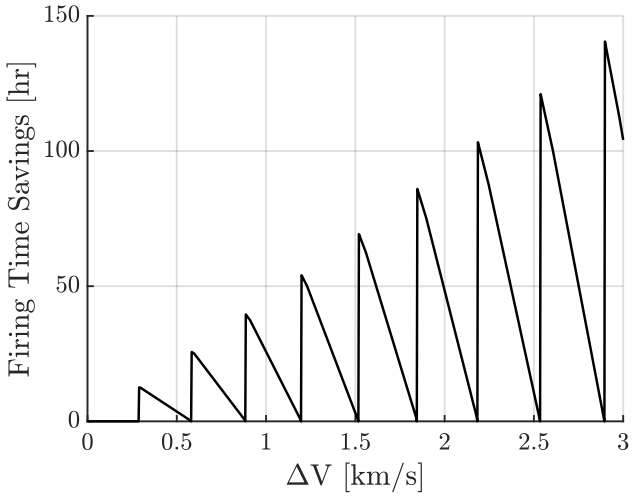


Figure 3-23: Firing time savings from optimal firing time distribution

approximately 3200 hours. Figure 3-23 shows the firing time savings from optimizing the firing time distribution to each stage over the standard firing time distribution for a minimum performance iEPS based propulsion system on a 3U CubeSat. We can see a growing sawtooth pattern where each tooth corresponds to a discrete number of stages. The amplitude of each tooth grows as more stages are added which is expected since more stages means a larger mass differential between the first and last stage and therefore a larger $\lambda_N$.

In practice, designing a stage-based propulsion system based around optimizing the firing time distribution is not recommended. Only minor reductions in the total firing time of the propulsion system are observed at the cost of actively throwing away a functioning stage early on in the mission - potentially sacrificing redundancy. However, for highly time sensitive missions, optimization of the stage timings can be used in flight to gain a few days' worth of time.

# Chapter 4

# Applications

## 4.1 Missions to Near-Earth Asteroids

Beyond escaping Earth orbit, missions to near-Earth asteroids represent the next step in terms of deep-space exploration for CubeSats and build towards more demanding missions such as missions to Mars or the Sun-Earth Lagrange points. Given the large number of potential asteroid targets, the asteroid survey needs to be filtered. The asteroids considered here are the same asteroids that are considered for asteroid retrieval/capture missions which aim to bring an asteroid from its heliocentric orbit to an orbit around Earth [18]. While the initial missions of a stage-based propulsion system equipped CubeSat would not be to bring an asteroid back to Earth, these "easily retrievable objects" were selected based on the low difference between their orbital elements and those of Earth as well as their small size. Both of these traits are applicable for a CubeSat based mission to an asteroid. The low difference in orbital elements minimizes the $\Delta$V required for rendezvous while the small size allows for the potential to land on the asteroid.

Table 4.1 shows the 12 "easily retrievable objects" as identified by [18] along with their heliocentric orbital elements and estimated diameter. The orbital elements were sourced from the JPL Small-Body Database [19] and the estimated diameter

Table 4.1: Orbital elements and estimated diameter of easily retrievable objects

| Asteroid | Semi-major Axis [AU] | Eccentricity | Inclination [°] | Diameter [m] |
|---|---|---|---|---|
| 2009 BD | 1.010 | 0.042 | 0.384 | 6.4-14.3 |
| 2006 RH120 | 1.002 | 0.351 | 1.088 | 3.3-7.5 |
| 2000 SG344 | 0.977 | 0.067 | 0.112 | 30.5-68.2 |
| 2011 UD21 | 0.979 | 0.030 | 1.062 | 5.3-11.9 |
| 2010 UE51 | 1.055 | 0.060 | 0.624 | 5.8-13.0 |
| 2010 VQ98 | 1.023 | 0.027 | 1.475 | 6.1-13.6 |
| 1991 VG | 1.032 | 0.053 | 1.430 | 5.8-13.0 |
| 2008 EA9 | 1.059 | 0.080 | 0.425 | 7.7-17.1 |
| 2007 UN12 | 1.054 | 0.060 | 0.236 | 4.8-10.8 |
| 2008 UA202 | 1.033 | 0.069 | 0.263 | 3.5-7.8 |
| 2011 MD | 1.060 | 0.041 | 2.562 | 6.7-14.9 |
| 2011 BL45 | 1.038 | 0.021 | 3.050 | 10.6-23.7 |

was calculated based on the relation between absolute magnitude and diameter [20]

$$D = 1329 \text{ km} \times 10^{-H/5} \rho_V^{-1/2} \tag{4.1}$$

where $D$ is the asteroid diameter, $H$ is the absolute magnitude, and $\rho_V$ is the albedo. The absolute magnitude was also taken from the JPL Small-Body Database while the albedo was assumed to be in the range typical of minor planets: 0.05 - 0.25. We can see that all of the asteroids surveyed have heliocentric orbital elements similar to those of Earth ($a \approx 1$, $e \approx 0$, $i \approx 0$) and their diameters are relatively small.

Table 4.2 shows the $\Delta$V and corresponding number of stages for propulsion system performance metrics ranged from minimum to target values in order to rendezvous with the surveyed near-Earth asteroids starting from geostationary orbit. Also shown are the next few closest approaches of each asteroid which can be used to guide the mission development timeline. The $\Delta$V values are calculated based on an assumed 2.67 km/s of $\Delta$V required to achieve escape from Earth plus an estimate of the required low-thrust $\Delta$V to rendezvous with the target asteroid from the JPL Small-Body Mission Design Tool [19]. The JPL Small-Body Mission Design Tool estimates the low-thrust $\Delta$V required for rendezvous disregarding phasing between the Earth and target asteroid and assuming constant acceleration throughout the transfer.

Table 4.2: Predicted ΔV, required number of stages, and available payload mass and volume for missions to near-Earth asteroids starting from geostationary orbit

| Asteroid | ΔV [km/s] | Stages (min-target) | Payload Mass [kg] | Payload Volume [U] | Next Closest Approaches |
|---|---|---|---|---|---|
| 2009 BD | 3.44 | 10-2 | 1.67-2.69 | 0.70-1.82 | 15-Mar-2022<br>01-Dec-2022<br>26-Jun-2023 |
| 2006 RH120 | 3.64 | 10-2 | 1.67-2.69 | 0.70-1.82 | 18-Aug-2028 |
| 2000 SG344 | 3.68 | 10-2 | 1.67-2.69 | 0.70-1.82 | 26-May-2026<br>16-May-2027<br>07-May-2028 |
| 2011 UD21 | 3.84 | 10-2 | 1.67-2.69 | 0.70-1.82 | 11-Oct-2039 |
| 2010 UE51 | 3.92 | 11-2 | 1.45-2.69 | 0.50-1.82 | 03-Oct-2022<br>24-Dec-2023 |
| 2010 VQ98 | 3.92 | 11-2 | 1.45-2.69 | 0.50-1.82 | 05-Jul-2038 |
| 1991 VG | 4.00 | 11-2 | 1.45-2.69 | 0.50-1.82 | 16-Oct-2037 |
| 2008 EA9 | 4.16 | 11-2 | 1.45-2.69 | 0.50-1.82 | 25-Apr-2020<br>25-Mar-2021 |
| 2007 UN12 | 4.18 | 11-2 | 1.45-2.69 | 0.50-1.82 | 04-Jul-2020<br>08-Jan-2021<br>11-Nov-2021 |
| 2008 UA202 | 4.30 | 11-2 | 1.45-2.69 | 0.50-1.82 | 05-May-2027<br>18-May-2028<br>20-Oct-2029<br>09-Nov-2030 |
| 2011 MD | 4.98 | 12-2 | 1.23-2.69 | 0.30-1.82 | 10-May-2023<br>04-Feb-2024<br>10-Aug-2024 |
| 2011 BL45 | 5.06 | 13-2 | 1.01-2.69 | 0.10-1.82 | 15-May-2028<br>02-Jul-2029<br>26-Aug-2030 |

While the $\Delta$V requirement is a rough estimate, we can see that the number of stages required for the mission is fairly stable. If the target performance metrics can be achieved then two stages are required for all of the asteroid targets surveyed. With the minimum performance metrics, then the number of stages only varies from 10 to 13 with a 1.62 km/s difference between the easiest and hardest to reach targets.

A 12 or 13 stage system is out of range of feasibility in terms of propulsion system volume as it would only leave 0.1-0.3U worth of volume for a payload. However, the easier to reach asteroids such as 2009 BD and 2010 UE51 are well within reach with payload masses of 1.67 kg and 1.45 kg and payload volumes of 0.7U and 0.5U respectively if the minimum performance metrics are used. In addition, the next closest approaches for this asteroids are mid to late 2023 which are well timed for a near-term mission.

If the target performance metrics are met then, from a payload perspective, all the surveyed asteroids are equally good targets as they all require the same number of stages. 2009 BD and 2010 UE51 still remain appealing in terms of their next closest approach date. However, 2011 MD has multiple closest approaches from mid 2023 - mid 2024 and both 2000 SG344 and 2008 UA202 offer good opportunities further out with closest approaches in mid 2026, 2027, and 2028.

## 4.2 Analytical Guidance

Approximations for the state of a spacecraft with constant, angular pointing thrust are derived in Appendix A. Figure 4-1 shows a comparison of the analytical approximation versus a numerical propagation of the dynamics for a circular orbit transfer from a medium Earth orbit (20,000 km) to geostationary orbit (42,164 km). We can see that the analytical approximation visually appears to follow the numerical propagation exactly.

Figure 4-2 shows the percent error in all four state variables in the orbital plane. We can see that for the radial position, angular position, and velocity in the angular direction the error is very small ($< 0.5\%$). The percent error in the radial velocity is

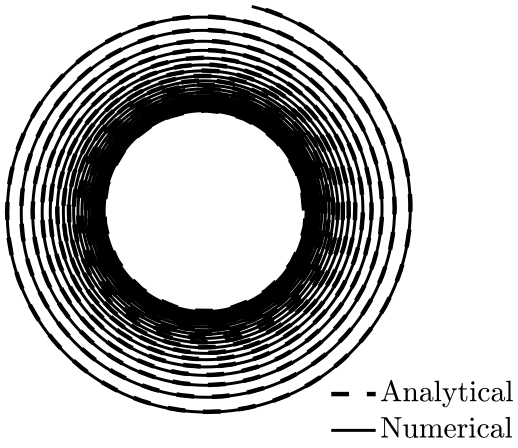


Figure 4-1: Comparison of analytical and numerical trajectories for orbit transfer

quite high, however this is due to the radial velocity being close to zero particularly at the beginning of the trajectory. As the trajectory progresses and the radial velocity increases, the percent error of the analytical approximation decreases and is $\sim$3% when the spacecraft reaches geostationary orbit.

The analytical approximation can also be extended out to escape from the central body. However, the approximation relied on the orbit being circular and as the trajectory progresses there will be more and more radial velocity causing the approximation to become inconsistent with the actual spacecraft dynamics. Figure 4-3 shows a comparison of the analytical approximation versus a numerical propagation of the dynamics from the same medium Earth orbit (20,000 km) all the way to escape from Earth. We can see that the analytical and numerical results diverge quite significantly on the last revolution of the spacecraft where the radial velocity becomes significant.

The divergence can also be seen in the error plots shown in Figure 4-4 where suddenly the percent error switches from decaying oscillations to an exponential growth. The switch to divergence is governed by the ratio of propulsive acceleration to gravitational acceleration. The "knee" in the error divergence is quite well predicted by the point when the propulsive acceleration is 10% of the instantaneous gravitational

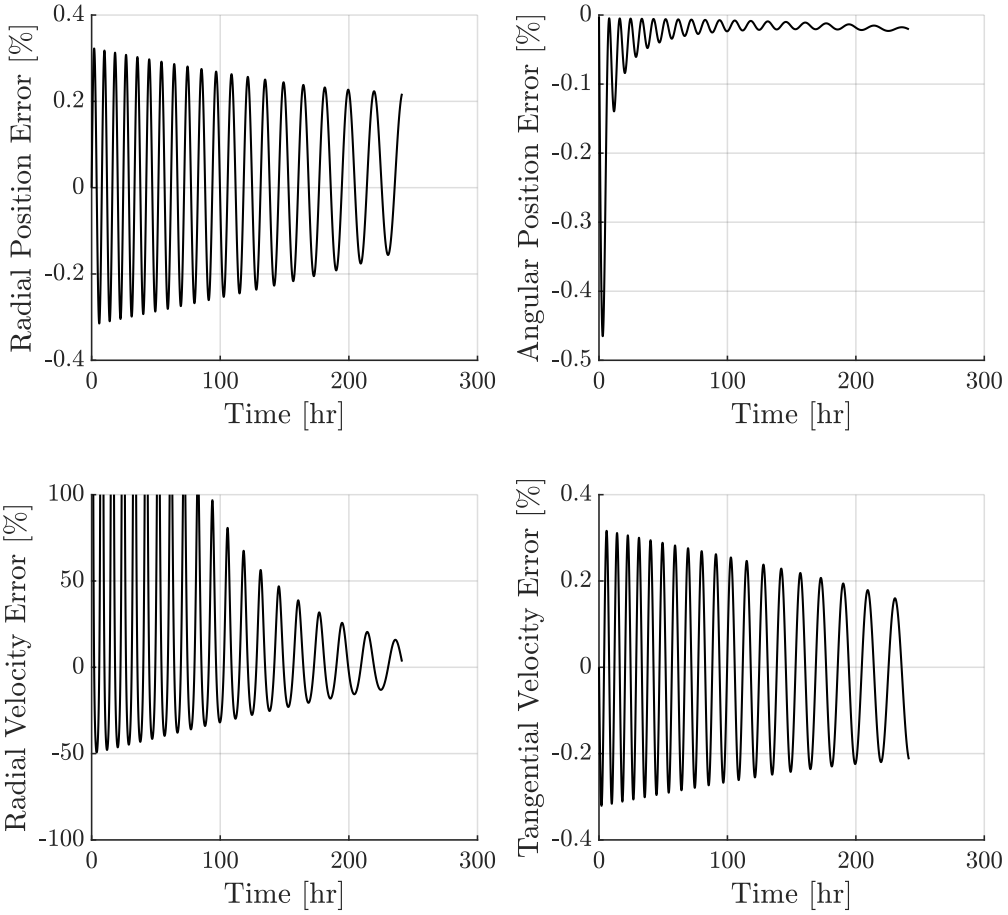


Figure 4-2: Percent error in analytical approximation relative to numerical propagation for orbit transfer

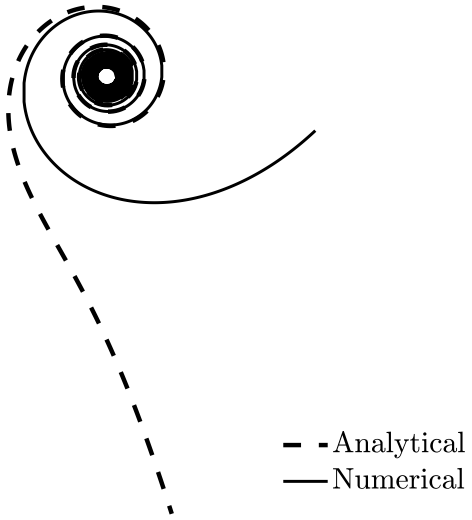


Figure 4-3: Comparison of analytical and numerical trajectories for escape

acceleration. Beyond that point, the propulsive acceleration is no longer dominated by the gravitational acceleration and the approximation that the orbit is circular no longer holds.

The slight difference between the analytical approximation and numerical propagation leads to the question of whether or not the analytical approximation can serve as a reference trajectory for guidance of a spacecraft on a circle to circle transfer or even to escape, assuming the divergence at the end of the trajectory can be overcome. Current methods for guidance of such trajectories either rely on optimization software such as GPOPS-II [14] or on feedback guidance-control laws. Solving for the trajectory with optimization software can be extremely powerful and allows for constraints to be explicitly satisfied. However, solutions can be computationally complex and susceptible to modeling errors. On the other hand, feedback guidance-control laws are computationally simple and can implicitly handle modeling errors. However, guidance-control laws control the spacecraft orbit geometry and not the spacecraft position preventing their use for rendezvous and limiting their application to orbit stabilization [21].

An analytical reference trajectory coupled with a feedback control law is a promis-

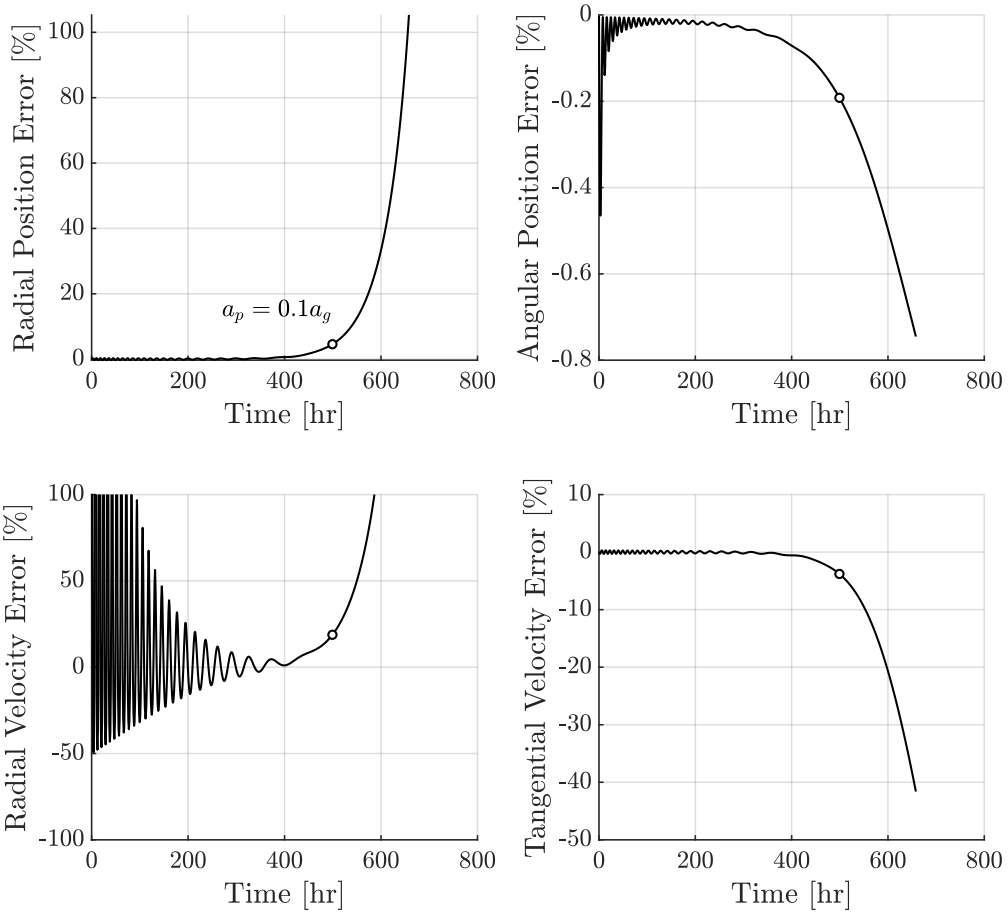


Figure 4-4: Percent error in analytical approximation relative to numerical propagation for escape

ing middle ground. The analytical reference allows for a computationally simple reference trajectory that does not require numerical propagation of the dynamics. Adding a feedback control law on the spacecraft state relative to the reference trajectory stabilizes the trajectory and helps eliminate the errors observed between the analytical approximation and numerical solution. While analytical solutions to low-thrust trajectories are certainly not a new topic [22, 23, 24], their practical application to both circle-to-circle transfer and escape trajectories combined with feedback trajectory stabilization has yet to be explored. Simple control methods such as the linear quadratic regulator with a linearized form of the dynamics serve quite well for trajectory stabilization but can struggle when thrust input is saturated. More advanced methods such as model predictive control sacrifice some of the computational simplicity but allow for the inclusion of constraints such as thrust saturation.

### 4.2.1 Closed-Loop Trajectory Control

While the analytical reference trajectory provides a close approximation of the true numerical trajectory, a feedback controller is required to stabilize the trajectory in the presence of modeling errors or to overcome the divergence between analytical and numerical solutions observed near the end of the escape trajectory. Two methods are considered here. The first is the infinite horizon linear quadratic regulator which provides a computationally simple feedback control law but can struggle when the propulsive acceleration is heavily dominated by the gravitational acceleration which occurs in low-Earth orbits since the problem formulation does not account for thrust saturation. The second control method is model predictive control with direct transcription. Model predictive control allows for specific modeling of thrust saturation constraints and is capable of controlling the spacecraft in low-Earth orbit.

**Infinite Horizon Linear Quadratic Regulator**

Given a linear system in state-space form

$$\dot{x} = Ax + Bu \tag{4.2}$$

the infinite horizon linear quadratic regulator (LQR) problem is to find the control input, $u$, to minimize the quadratic cost function

$$\min_u J = \int_{t_0}^{\infty} \left[ x^{\mathrm{T}} Q x + u^{\mathrm{T}} R u \right] dt \tag{4.3}$$

where $Q$ and $R$ are weighting matrices for state error and control effort respectively. The problem can be solved analytically using optimal control with calculus of variations [16] and the resulting controller is a linear feedback controller

$$u = -Kx \tag{4.4}$$

where the control gain, $K$, is defined as

$$K = R^{-1} B^{\mathrm{T}} P \tag{4.5}$$

and $P$ is the solution to the algebraic Riccati equation

$$PA + A^{\mathrm{T}} P + Q - PBR^{-1} B^{\mathrm{T}} P = 0 \tag{4.6}$$

To implement the controller for trajectory control, the dynamics of the spacecraft need to be linearized. Since the orbit of the spacecraft is approximately circular throughout the trajectory, the Hill-Clohessy-Wiltshire equations for linearized relative motion around a circular reference orbit are used. Prussing and Conway provide a good reference for the derivation of the Hill-Clohessy-Wiltshire equations in [25]. The equations used here are the same as in the derivation except for modifications to express the position along the direction of motion in terms of the angular position,

include mass as a variable, and include an assumed angular pointing thrust

$$A = \begin{bmatrix} 0 & 0 & 1 & 0 & 0 \\ 0 & 0 & 0 & 1/r_0 & 0 \\ 0 & 0 & 0 & 2v_0/r_0 & 0 \\ 0 & 3v_0/r_0 & -2v_0/r_0 & 0 & -F/m_0^2 \\ 0 & 0 & 0 & 0 & 0 \end{bmatrix} \tag{4.7}$$

$$B = \begin{bmatrix} 0 & 0 \\ 0 & 0 \\ 1/m_0 & 0 \\ 0 & 1/m_0 \\ 0 & -1/c \end{bmatrix} \tag{4.8}$$

where $r_0$ is the initial orbital radius, $v_0$ is the initial orbital velocity, $m_0$ is the initial mass of the spacecraft, $F$ is the angular pointing thrust for the reference trajectory, and $c$ is the exhaust velocity of the propulsion system.

The full control input to the spacecraft is then

$$u = u_0 - Kx_{\text{err}} \tag{4.9}$$

where $u_0$ is the feedforward control for the analytical reference trajectory and is

$$u_0 = \begin{bmatrix} 0 \\ F \end{bmatrix} \tag{4.10}$$

and $x_{\text{err}}$ is the error between the current state of the spacecraft and the analytical reference trajectory. The magnitude of the control input is saturated to be within the thrust limits of the propulsion system.

### Model Predictive Control with Direct Transcription

Model predictive control (MPC) with direct transcription approaches a similar problem but from the perspective of a constrained optimization over a fixed time horizon in discrete time. Appendix B shows a simple application of model predictive control for path planning in free space. The dynamics are in general a nonlinear function

$$x[n+1] = f(x[n], u[n]) \tag{4.11}$$

The goal is to find the state and control input to minimize the cost function over some time horizon which can also be a general nonlinear function

$$\min_{x,u} J = \sum_{n=0}^{N} g(x[n], u[n]) \tag{4.12}$$

subject to dynamics constraints between time points

$$x[n+1] = f(x[n], u[n]) \qquad \forall n \in \{0, N-1\} \tag{4.13}$$

and subject to any other state and control constraints. The controller then takes the resulting optimal control at the first time step, $u[0]$, applies it to the system, and shifts the horizon forward in time to solve the optimization problem again at the next time step. This receding time horizon technique allows the optimization problem to be computationally tractable but does not guarantee optimality of the solution over the whole time horizon of the problem.

For our problem we will consider a quadratic cost function

$$\min_{x,u} J = \sum_{n=1}^{N} (x[n] - x_{\text{ref}}[n])^{\text{T}} Q (x[n] - x_{\text{ref}}[n]) + u[n]^{\text{T}} R u[n] \tag{4.14}$$

subject to an initial state constraint

$$x[0] = x_0 \tag{4.15}$$

and thrust saturation constraints

$$(u[n] + u_0)^{\mathrm{T}}(u[n] + u_0) \leq F_{\max} \qquad \forall n \in \{0, N-1\} \tag{4.16}$$

where $u_0$ is the feedforward control for the analytical reference trajectory. The dynamics will be linearized dynamics around the reference trajectory and feedforward control. In continuous time the linearized error dynamics can be written as

$$\dot{x}_{\mathrm{err}} = Ax_{\mathrm{err}} + Bu \tag{4.17}$$

$$\tag{4.18}$$

where

$$A = \begin{bmatrix} 0 & 0 & 1 & 0 & 0 \\ -v_\theta/r^2 & 0 & 0 & 1/r & 0 \\ -v_\theta^2/r^2 + 2\mu/r^3 & 0 & 0 & 2v_\theta/r & 0 \\ v_r v_\theta/r^2 & 0 & -v_\theta/r & -v_r/r & -F/m^2 \\ 0 & 0 & 0 & 0 & 0 \end{bmatrix} \tag{4.19}$$

$$B = \begin{bmatrix} 0 & 0 \\ 0 & 0 \\ 1/m & 0 \\ 0 & 1/m \\ 0 & -1/c \end{bmatrix} \tag{4.20}$$

where $r$ is the radial position, $v_r$ is the radial velocity, $v_\theta$ is the velocity in the angular direction, $m$ is the spacecraft mass, $F$ is the feedforward thrust for the analytical reference trajectory, $c$ is the propulsion system exhaust velocity, and $\mu$ is the gravitational parameter of the central body. Given a time step, $dt$, the dynamics can be converted to discrete time and the dynamics constraints can be written as

$$x_{\mathrm{err}}[n+1] = A_d x_{\mathrm{err}}[n] + B_d u[n] \tag{4.21}$$

The optimization problem is then solved for the state error and control input over the time horizon using MATLAB's `fmincon` solver with sequential quadratic programming. The control applied to the spacecraft is then

$$u = u_0 + u[0] \tag{4.22}$$

which is already constrained to be within the thrust saturation limits from the constraints applied to the optimization problem.

### 4.2.2 Navigation

Navigation during the escape spiral is not strictly required for testing the analytical reference trajectory. However, since the idea behind the analytical reference trajectory is to move towards more capable autonomous spacecraft, it is worth considering how a spacecraft could autonomously navigate during an escape spiral.

Since the dynamics are nonlinear, a continuous time extended Kalman filter is used. Consider a nonlinear dynamics model

$$\dot{x}(t) = f(x(t), u(t)) + w(t) \tag{4.23}$$

$$z(t) = h(x(t)) + v(t) \tag{4.24}$$

where $x$ is the state vector, $u$ is the control vector, $z$ is the measurement vector, $w$ is the process noise, and $v$ is the measurement noise. Both the process and measurement noise are normally distributed as

$$w \sim \mathcal{N}(0, Q) \tag{4.25}$$

$$v \sim \mathcal{N}(0, R) \tag{4.26}$$

where $Q$ and $R$ are associated covariances. The goal of the extended Kalman filter is

to estimate the state of the spacecraft, $\hat{x}$, which is initialized as

$$\hat{x}(t_0) = \mathrm{E}[x(t_0)] \tag{4.27}$$

the expected value of the initial state and has covariance, $P$, given by the covariance of the initial state

$$P(t_0) = \mathrm{Var}[x(t_0)] \tag{4.28}$$

The state estimate and associated covariance are updated as

$$\dot{\hat{x}}(t) = f(\hat{x}(t), u(t)) + K(t)\left(z(t) - h(\hat{x}(t))\right) \tag{4.29}$$

$$\dot{P}(t) = F(t)P(t) + P(t)F(t)^{\mathrm{T}} - K(t)H(t)P(t) + Q(t) \tag{4.30}$$

where the estimation gain, $K(t)$, is calculated as

$$K(t) = P(t)H(t)^{\mathrm{T}}R(t)^{-1} \tag{4.31}$$

and $F(t)$ and $H(t)$ are the linearized dynamics and measurement equations at the current state estimate

$$F(t) = \left.\frac{\partial f}{\partial x}\right|_{\hat{x}(t),u(t)} \tag{4.32}$$

$$H(t) = \left.\frac{\partial h}{\partial x}\right|_{\hat{x}(t)} \tag{4.33}$$

The dynamics model is the full nonlinear two body orbital dynamics in polar

coordinates

$$f(x,u) = \begin{bmatrix} \dot{r} \\ \dot{\theta} \\ \dot{v}_r \\ \dot{v}_\theta \\ \dot{m} \end{bmatrix} = \begin{bmatrix} v_r \\ v_\theta/r \\ v_\theta^2/r - \mu/r^2 + F_r/m \\ -v_r v_\theta/r + F_\theta/m \\ -\sqrt{F_r^2 + F_\theta^2}/c \end{bmatrix} \tag{4.34}$$

Two measurements are considered based on the potential for optical based measurements. The first is a measurement of the angular diameter of Earth, $\phi_{\text{Earth}}$, which is related to the radial position of the satellite as

$$\tan\left(\frac{1}{2}\phi_{\text{Earth}}\right) = \frac{R_{\text{Earth}}}{r} \tag{4.35}$$

where $R_{\text{Earth}}$ is the physical radius of Earth. The second measurement is assumed to be a direct measurement of the angular position of the satellite which would be based on star tracker measurements of the heading of the satellite and the assumed angular pointing control law - fixing the orientation of the satellite with respect to Earth. With the two measurements, the measurement equation is

$$h(x) = \begin{bmatrix} \phi_{\text{Earth}} \\ \theta \end{bmatrix} = \begin{bmatrix} 2\tan^{-1}\left(\dfrac{R_{\text{Earth}}}{r}\right) \\ \theta \end{bmatrix} \tag{4.36}$$

### 4.2.3 Circle-Circle Transfers

Two circle-circle transfer scenarios are considered: medium Earth orbit (20,000 km) to geostationary orbit and low-Earth orbit (7,000 km) to geostationary orbit. Medium Earth orbit represents the less demanding scenario due to its lower transfer time and weaker gravitational acceleration and therefore will be analyzed first.

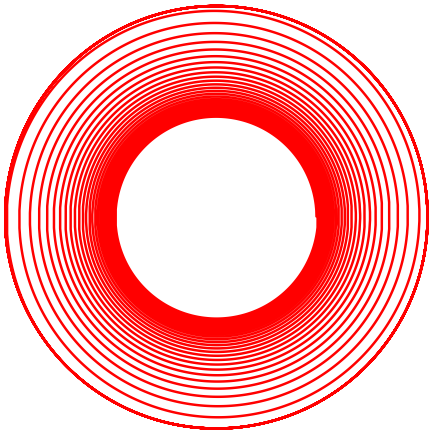

Figure 4-5: Analytical reference trajectory for transfer from a circular medium-Earth orbit to geostationary orbit

**MEO-GEO**

Figure 4-5 shows the analytical reference trajectory for transfer from a circular medium-Earth orbit to geostationary orbit with a 4 kg spacecraft with a propulsion system producing 10 times the minimum thrust of a 3U compatible iEPS based propulsion system. The analytical reference trajectory was calculated with an input thrust of 75% of the maximum thrust output of the propulsion system in order to provide margin for feedback control. Equations A.12 through A.15 are used during the transfer after which three full orbit's worth of circular reference trajectory is added to stabilize the spacecraft at geostationary orbit.

Figure 4-6 shows the true trajectory of the spacecraft compared to the reference trajectory when infinite horizon LQR is used for trajectory stabilization. Two circles show the true final position of the spacecraft (black) versus the final position of the reference trajectory (red). We can see that the true trajectory closely follows the analytical reference trajectory and that the final spacecraft position is very close to the final reference position with a 1.7 degree difference in the final angular positions.

Figure 4-7 shows the control thrust in both the angular and radial directions normalized by the maximum thrust output of the propulsion system. We can see that initially, the controller is stressed as it attempts to lock onto the analytical

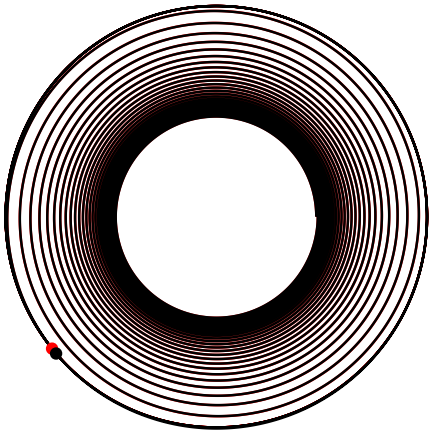

Figure 4-6: LQR feedback controlled trajectory for transfer from a circular medium-Earth orbit to geostationary orbit

reference trajectory since the analytical reference trajectory starts with a non-zero radial velocity. From ∼20 hours to ∼320 hours into the trajectory, the spacecraft has locked into the analytical reference trajectory and the main control input is the feedforward angular thrust. At ∼320 hours the spacecraft reaches geostationary orbit and the controller is again stressed as it attempts to attenuate the radial velocity it built up during the transfer. After about ∼30 hours (1.25 orbits) the spacecraft has stabilized to the geostationary orbit and the control thrust is close to zero.

For the model predictive control implementation the time horizon is set to be half the period of the current orbit of the spacecraft. Time steps are evenly spaced across the time horizon and the corresponding optimization problem is solved for the optimal control input at the current time. The orbit of the spacecraft is them propagated forward for one time step with the control thrust held constant at which point the process repeats. Once the spacecraft reaches geostationary orbit, the time horizon is shrunk to 1/5 of the orbital period in order to provide finer control during the stabilization period.

Figure 4-8 shows the true trajectory of the spacecraft compared to the reference trajectory when model predictive control is used for trajectory stabilization. The two circles that show the final positions of the true and reference trajectories overlap

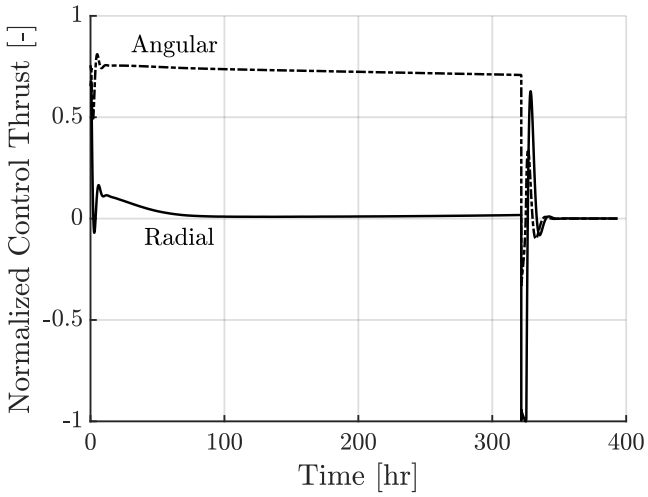


Figure 4-7: Control thrust for LQR feedback controlled trajectory for transfer from a circular medium-Earth orbit to geostationary orbit

with no visually discernible difference. The difference in the final angular position of the two trajectories is only 0.048 degrees - better than when using LQR for feedback control. The control thrust in both the angular and radial directions, again normalized by the maximum thrust output of the propulsion system, is shown in Figure 4-9. Compared to the LQR solution in Figure 4-7 we can see that the controller is able to lock onto the analytical trajectory faster, with no lingering feedback control thrust in the radial direction. This is due to the ability of model predictive control to explicitly include thrust saturation constraints when calculating the thrust output at each time step and to "see" ahead in the trajectory. Once the spacecraft reaches geostationary orbit, the control thrust for LQR and MPC look quite similar.

**LEO-GEO**

Figure 4-10 shows the analytical reference trajectory for transfer from a circular low-Earth orbit to geostationary orbit with a 4 kg spacecraft with a propulsion system producing 10 times the minimum thrust of a 3U compatible iEPS based propulsion system. As before, the analytical reference trajectory was calculated with an input thrust of 75% of the maximum thrust output of the propulsion system in order to provide margin for feedback control. Equations A.12 through A.15 are used during

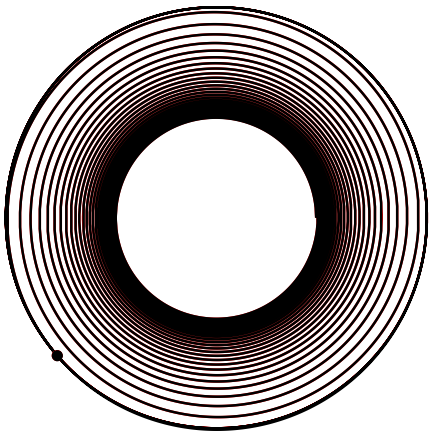

Figure 4-8: MPC feedback controlled trajectory for transfer from a circular medium-Earth orbit to geostationary orbit

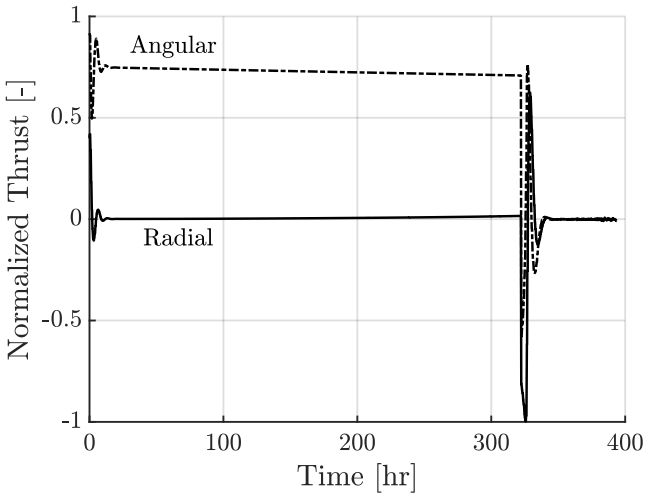


Figure 4-9: Control thrust for MPC feedback controlled trajectory for transfer from a circular medium-Earth orbit to geostationary orbit

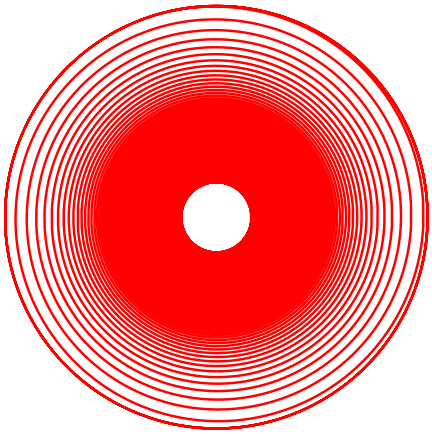

Figure 4-10: Analytical reference trajectory for transfer from a circular low-Earth orbit to geostationary orbit

the transfer after which three full orbit's worth of circular reference trajectory is added to stabilize the spacecraft at geostationary orbit.

Figure 4-11 shows the true trajectory of the spacecraft compared to the reference trajectory when infinite horizon LQR is used for trajectory stabilization. The two circles show the true final position of the spacecraft (black) versus the final position of the reference trajectory (red). Instead of the spacecraft following the reference trajectory, the LQR feedback control drives the spacecraft inward towards Earth causing it to crash into the surface. Figure 4-12 shows the true radial position versus the reference radial position. The spacecraft initially follows the reference radial position but quickly ends up going inwards towards the Earth rather than following the reference.

Figure 4-13 shows the control thrust during the trajectory prior to the spacecraft crashing into the Earth normalized by the maximum thrust output of the propulsion system. We can see that the angular thrust goes negative, opposite what is expected. This creates an unstable feedback loop where the spacecraft is in a lower orbit than the reference trajectory causing it to move ahead of the reference in terms of angular position. This ends up feeding back into the controller causing the angular control thrust to be pushed negative as the spacecraft attempts to slow down and return

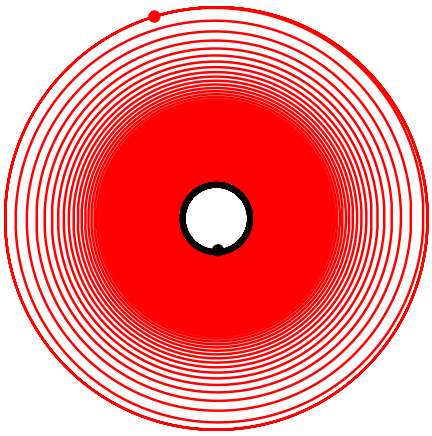

Figure 4-11: LQR feedback controlled trajectory for transfer from a circular low-Earth orbit to geostationary orbit

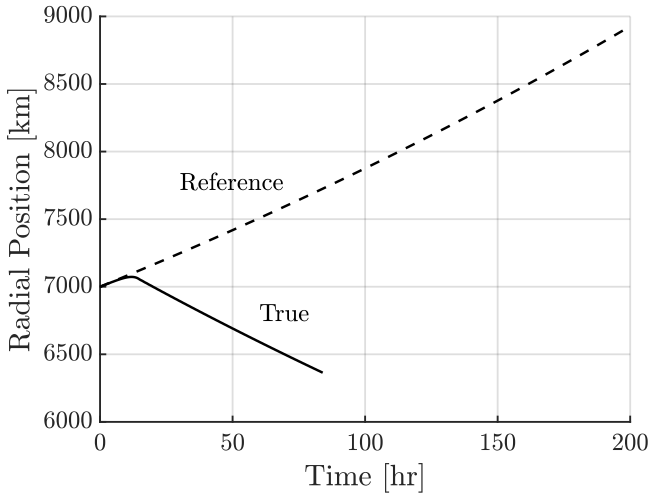


Figure 4-12: Radial position of the spacecraft when using LQR feedback control starting from a circular low-Earth orbit

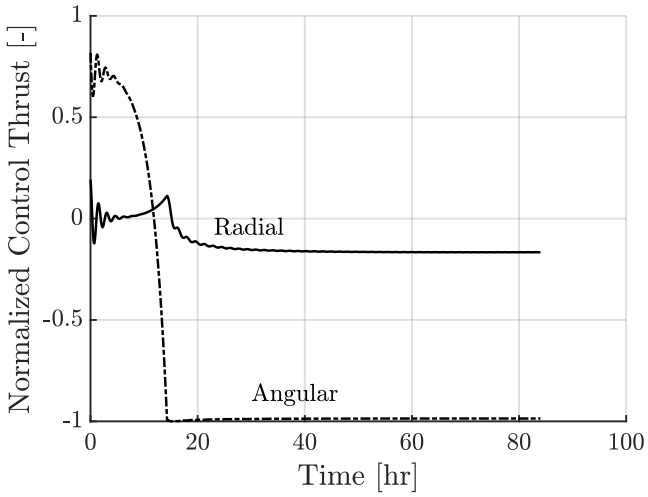


Figure 4-13: Control thrust for LQR feedback controlled trajectory for transfer from a circular low-Earth orbit to geostationary orbit

to the reference trajectory, lowering the spacecraft orbit, and repeating the cycle. It is predicted that this behavior is caused by the low control authority that the spacecraft has in low-Earth orbit relative to the local gravitational acceleration. Since the spacecraft is unable to latch onto the reference trajectory, it ends up in a lower radius orbit and starts the cycle of unstable feedback control. However, it is expected that the spacecraft should be able to at least stay with the reference trajectory since the reference trajectory is an approximation of the true spacecraft dynamics if thrust is applied in the positive angular direction.

Model predictive control can be used to fix this problem. In this case, the time horizon for the optimization was set to be four full orbits ahead of the current spacecraft position. This allows the controller to "see" ahead in the trajectory and not enter into the unstable feedback control cycle. Figure 4-14 shows the true trajectory of the spacecraft compared to the reference trajectory when model predictive control is used for trajectory stabilization. We can see that the spacecraft is able to follow the reference trajectory and the final positions of the true and reference trajectories (represented by the black and red circles respectively) are quite close with an angular position difference of only 0.20 degrees.

Figure 4-15 shows the control thrusts in the angular and radial direction normal-

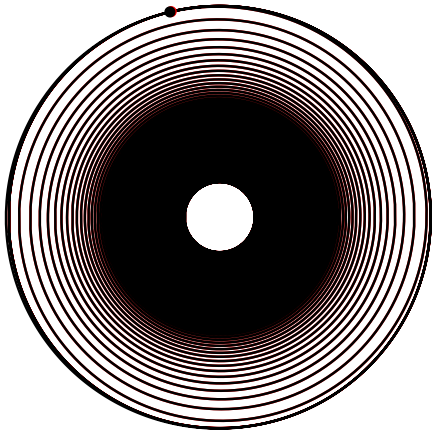

Figure 4-14: MPC feedback controlled trajectory for transfer from a circular low-Earth orbit to geostationary orbit

ized by the maximum thrust output of the propulsion system during the trajectory for the MPC feedback controller. As opposed to the LQR feedback controller shown in Figure 4-13 the MPC controller keeps a positive angular thrust, as this allows the spacecraft to roughly follow the reference trajectory, and makes small corrections in order to latch onto the trajectory. As with the medium-Earth orbit to geostationary orbit case, once the spacecraft locks onto the reference trajectory the main control thrust is the feedforward thrust of the analytical reference.

### 4.2.4 Escape Trajectory

Using the analytical reference trajectory for escape represents both a less demanding scenario, as the gravitational acceleration is lower, and a more demanding scenario, as the reference trajectory becomes inconsistent with the dynamics of the system. The inconsistencies between the dynamics of the system and the trajectory can be fixed by redefining what the feedforward control should be. Given the velocity dynamics

$$\dot{v}_r = v_\theta^2/r - \mu/r^2 + F_r/m \tag{4.37}$$

$$\dot{v}_\theta = -v_r v_\theta/r + F_\theta/m \tag{4.38}$$

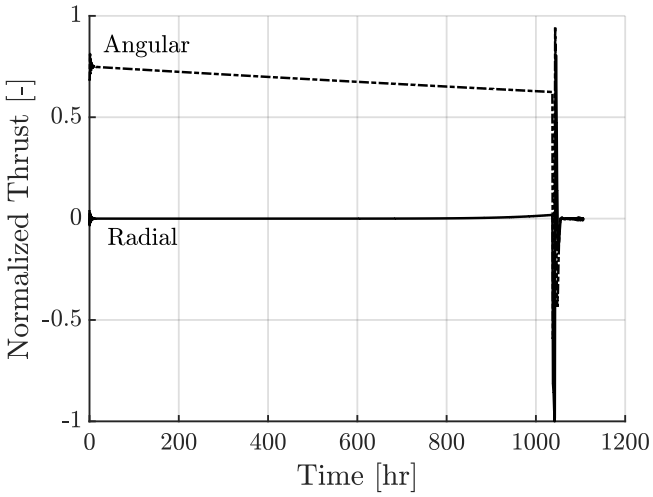


Figure 4-15: Control thrust for MPC feedback controlled trajectory for transfer from a circular low-Earth orbit to geostationary orbit

we can calculate the actual velocity derivatives based on the analytical equations for $v_r$ and $v_\theta$ to get

$$\dot{v}_r = \frac{6r_0 a_\mathrm{p}^2/v_0^2}{\left(1 - \frac{a_\mathrm{p}}{v_0}t\right)^4} \tag{4.39}$$

$$\dot{v}_\theta = -a_\mathrm{p} \tag{4.40}$$

and then solve for the required $F_r$ and $F_\theta$ to make the spacecraft exactly follow the reference trajectory

$$F_r = m(\dot{v}_r + \mu/r^2 - v_\theta^2/r) \tag{4.41}$$

$$F_\theta = m(\dot{v}_\theta + v_r v_\theta/r) \tag{4.42}$$

Plugging in Equations 4.39 and 4.40 along with Equations A.12 through A.15 we get

$$F_r = m\frac{6r_0 a_\mathrm{p}^2/v_0^2}{\left(1 - \frac{a_\mathrm{p}}{v_0}t\right)^4} \tag{4.43}$$

$$F_\theta = m\ a_\mathrm{p} \tag{4.44}$$

which differs from the original feedforward control by introducing a radial thrust.

This correction to the feedforward thrust input serves two purposes. Firstly, it makes the trajectory and dynamics of the spacecraft consistent with each other which improves the performance of any feedback controller layered over the feedforward guidance. Second, it allows us to properly size the reference trajectory for a given propulsion system. Given a maximum thrust the propulsion system can produce, the feedforward acceleration, $a_p$, can be selected such that at the end of the trajectory, the required thrust from the feedforward thrust input is within what the propulsion system can provide.

Figure 4-16 shows the magnitude of the feedforward thrust normalized by the maximum thrust of the propulsion system versus time normalized by the escape time for a minimum performance iEPS based propulsion system on a 3U CubeSat starting from geostationary orbit. It is assumed that the acceleration for the reference trajectory, $a_\mathrm{p}$ is calculated as

$$a_\mathrm{p} = \frac{F}{m_0} \tag{4.45}$$

where $F$ is the maximum thrust of the propulsion system and $m_0$ is the initial spacecraft mass. Initially the thrust is within the capabilities of the propulsion system as the mass of the spacecraft decreases and the thrust required to maintain the feedforward acceleration decreases correspondingly. However, towards the end of the trajectory, the feedforward acceleration in the radial direction increases significantly and the thrust required to maintain the total acceleration goes beyond the capabilities of the propulsion system. In order to fix this problem, the acceleration for the reference trajectory has to be reduced such that at the end of the trajectory the thrust magnitude is lower than the maximum thrust of the propulsion system.

Formally, the problem can be posed as solving for a thrust reduction factor, $C$, such that the feedforward acceleration is calculated as

$$a_\mathrm{p} = C\frac{F}{m_0} \tag{4.46}$$

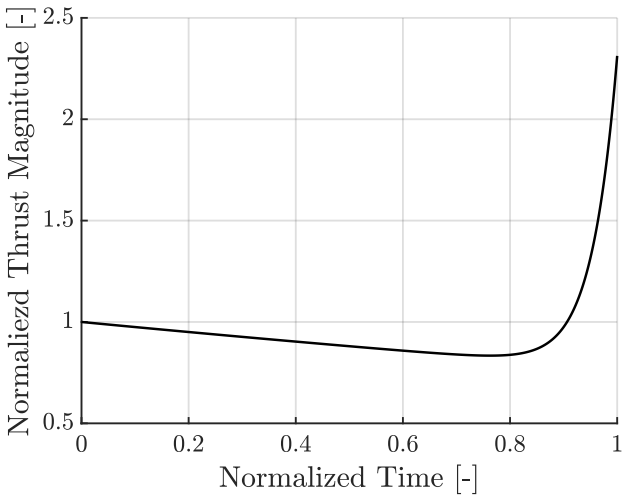


Figure 4-16: Feedforward thrust normalized by maximum thrust of the propulsion system versus time normalized by the escape time

and then calculating the escape time with Equation 3.73 as

$$t_{\text{esc}} = \frac{v_0}{a_{\text{p}}} \left[ 1 - (2\epsilon)^{1/4} \right] \tag{4.47}$$

where $\epsilon$ is the ratio of the propulsive acceleration to gravitational acceleration at the initial orbit conditions. No numerical correction for the scalar factor $2^{1/4}$ is used in this escape time calculation as the reference trajectory is no longer an approximation of the escape trajectory. The mass at the end of the trajectory, $m_{\text{f}}$, can be calculated by integrating

$$\dot{m} = -\frac{\sqrt{F_r + F_\theta}}{c} \tag{4.48}$$

up to the escape time. Which can then be used to calculate the thrust magnitude at the end of the trajectory from

$$F_{r,\text{f}} = m_{\text{f}} \frac{6 r_0 a_{\text{p}}^2 / v_0^2}{\left( 1 - \frac{a_{\text{p}}}{v_0} t_{\text{esc}} \right)^4} \tag{4.49}$$

$$F_{\theta,\text{f}} = m_{\text{f}} a_{\text{p}} \tag{4.50}$$

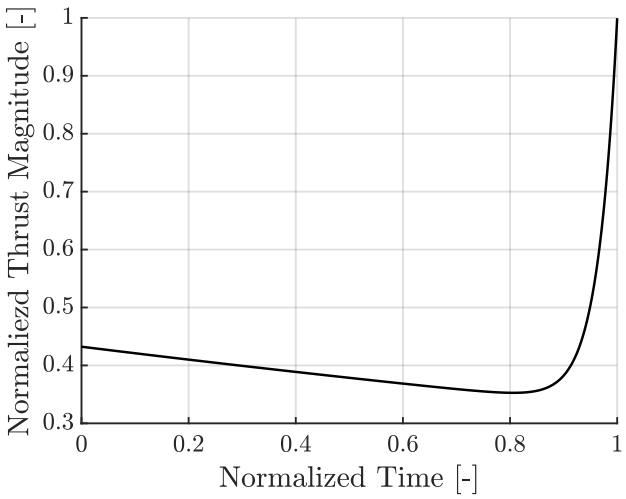


Figure 4-17: Feedforward thrust normalized by maximum thrust of the propulsion system versus time normalized by the escape time when reduced for feasibility

The solver is then tasked with maximizing $C$ such that

$$F_{r,\mathrm{f}}^2 + F_{\theta,\mathrm{f}}^2 \leq F^2 \tag{4.51}$$

For a minimum performance iEPS based propulsion system on a 3U CubeSat starting from geostationary orbit the thrust reduction factor is 0.4323. Figure 4-17 shows the magnitude of the feedforward thrust normalized by the maximum thrust of the propulsion system when the acceleration for the reference trajectory is reduced based on Equation 4.46. We can see that the thrust is equal to the maximum thrust of the propulsion system right when escape is achieved. However, the thrust throughout the majority of the trajectory is reduced significantly from its maximum value thereby increasing the time to achieve escape.

Figure 4-18 shows the analytical reference trajectory for escape from Earth starting from geostationary orbit where the acceleration for the reference trajectory is reduced by 0.4323. The reference trajectory takes far longer due to the reduced acceleration requiring 10,040 hours to achieve escape compared to the 4,300 hours of the un-reduced escape trajectory. However, the reduced reference acceleration allows the spacecraft to exactly follow the reference trajectory. Figure 4-19 shows a linear

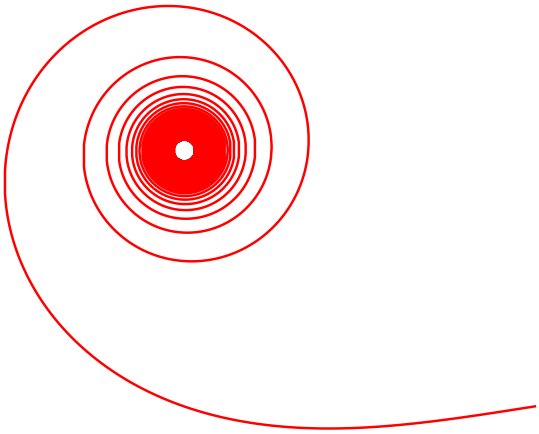

Figure 4-18: Analytical reference trajectory for escape from Earth starting from geostationary orbit with reduced reference acceleration

quadratic regulator controlled trajectory for the reduced acceleration reference trajectory. A black circle at the end of the trajectory represents the true final position of the spacecraft while a red circle represents the final position of the reference trajectory. We can see that the true trajectory exactly follows the reference trajectory so much that the red circle is not visible as it exactly lines up with the true final position of the spacecraft.

Figure 4-20 shows the control thrust for the LQR feedback controlled trajectory in the first 100 hours of the trajectory and for the full escape trajectory. For the first 20 hours of the trajectory, the controller is stressed as it fixes the difference in radial velocity between the true trajectory and analytical reference. After 20 hours, the spacecraft locks onto the analytical reference and follows the reference acceleration for the remainder of the escape trajectory. Figure 4-21 shows the control thrust magnitude normalized by the maximum thrust of the propulsion system versus time normalized by the escape time. We can see that the thrust is reduced for the majority of the trajectory such that, at the end of the trajectory, the control thrust is exactly the maximum thrust output of the propulsion system.

If the reference trajectory acceleration is not reduced appropriately, then the spacecraft cannot physically follow the reference trajectory. Figure 4-22 shows the

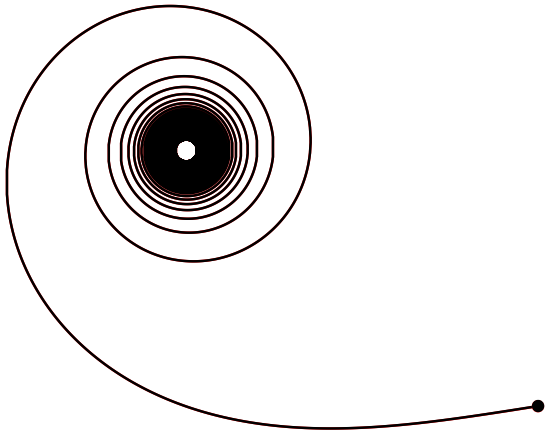

Figure 4-19: LQR feedback controlled trajectory for escape from Earth starting from geostationary orbit with reduced reference acceleration

LQR feedback controlled trajectory for escape when the thrust reduction factor is 0.8 rather than the required 0.4323. We can see that the spacecraft is able to follow the reference trajectory for the majority of the escape, but the true trajectory begins to diverge from the reference trajectory just before escape is achieved.

Figure 4-23 shows the corresponding control thrust magnitude normalized by the maximum thrust of the propulsion system versus time normalized by the escape time. We can see two differences from the control thrust magnitude in the fully reduced trajectory in Figure 4-21. Firstly, the thrust is saturated at the beginning of the trajectory as the controller attempts to drive the spacecraft to the reference trajectory. Second, the thrust is saturated at the end of the trajectory as the magnitude of the feedforward control thrust is greater than the maximum thrust output of the propulsion system. This prevents the spacecraft from being able to follow the reference trajectory.

While the partially reduced reference acceleration causes the spacecraft to be unable to follow the reference trajectory just before escape is achieved, the time to achieve escape is reduced from 10,040 hours to 5,537 hours. Therefore, a tradeoff exists. Either the analytical reference can be exactly consistent with the feasible dynamics of the spacecraft with a significant hit to the escape time, or the escape

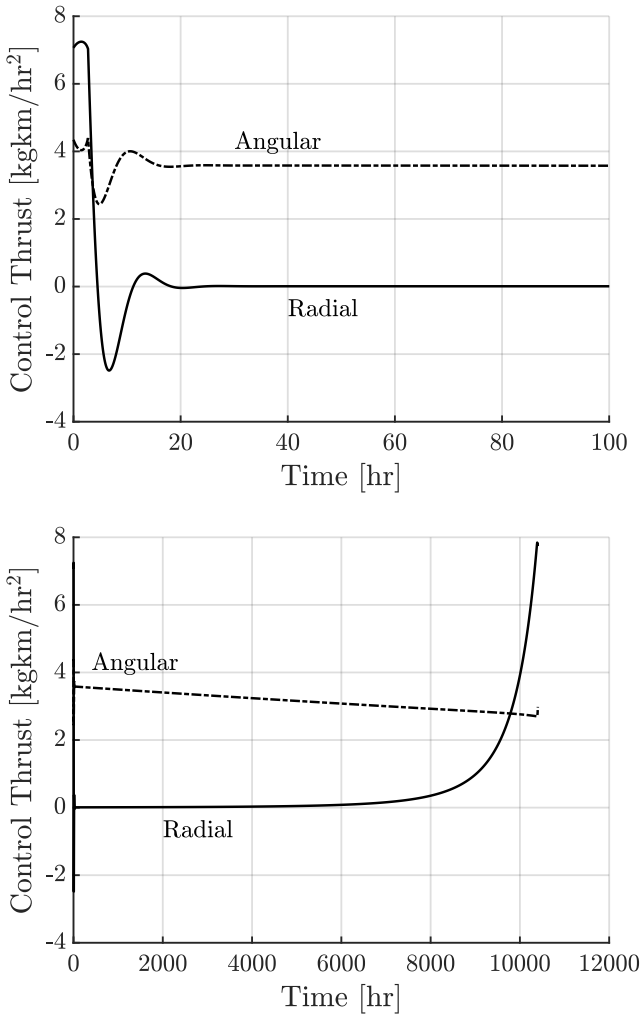


Figure 4-20: Control thrust for LQR feedback controlled trajectory for escape from Earth starting from geostationary orbit with reduced reference acceleration

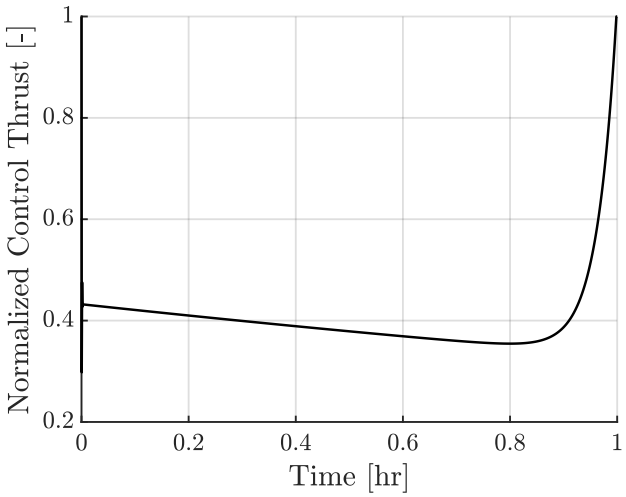


Figure 4-21: Control thrust magnitude normalized by the maximum thrust of the propulsion system for LQR feedback controlled trajectory for escape from Earth starting from geostationary orbit with reduced reference acceleration

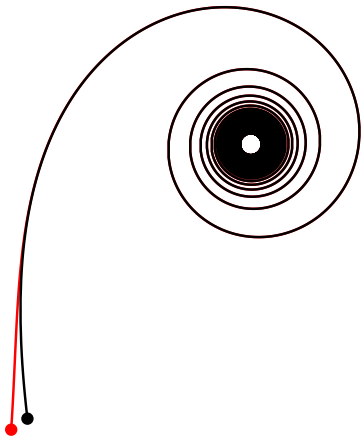

Figure 4-22: LQR feedback controlled trajectory for escape from Earth starting from geostationary orbit with partially reduced reference acceleration

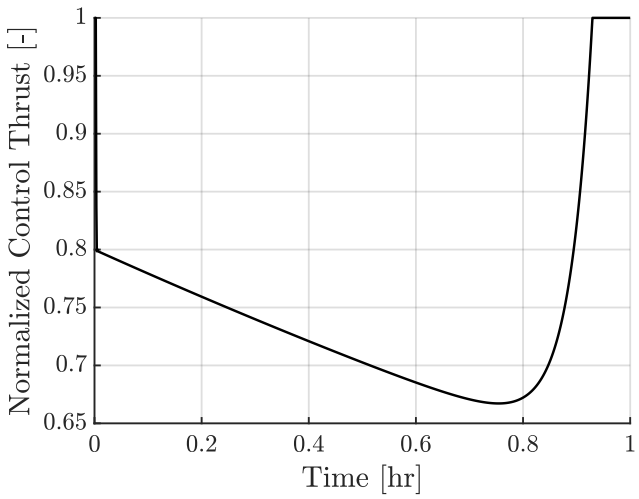


Figure 4-23: Control thrust magnitude normalized by maximum thrust of the propulsion system for LQR feedback controlled trajectory for escape from Earth starting from geostationary orbit with partially reduced reference acceleration

time can be reduced with the consequence that the analytical reference is dynamically infeasible for the spacecraft to achieve which causes a small difference between the true and reference trajectory right as escape is achieved.

### Impact of Staging

Returning to Equations 4.49 and 4.50 we know that the magnitude of the feedforward thrust at the end of the trajectory is

$$F_{\mathrm{f}} = m_{\mathrm{f}} \sqrt{a_{\mathrm{p}}^2 + \frac{36 r_0^2 a_{\mathrm{p}}^4 / v_0^4}{\left(1 - \frac{a_{\mathrm{p}}}{v_0} t_{\mathrm{esc}}\right)^8}} = m_{\mathrm{f}} a_{\mathrm{f}} \tag{4.52}$$

where $a_{\mathrm{f}}$ is the magnitude of the reference acceleration at the end of the trajectory. Given $a_{\mathrm{p}}$, the final magnitude of the reference acceleration is set. Therefore, to reduce the magnitude of the final feedforward thrust and keep the feedforward thrust below the maximum thrust output of the propulsion system, the final mass of the spacecraft needs to be reduced. Using a stage-based propulsion system drops dry mass throughout the trajectory and inherently reduces the final mass. Running the same calculation of the thrust reduction factor in Equation 4.46, the thrust reduction

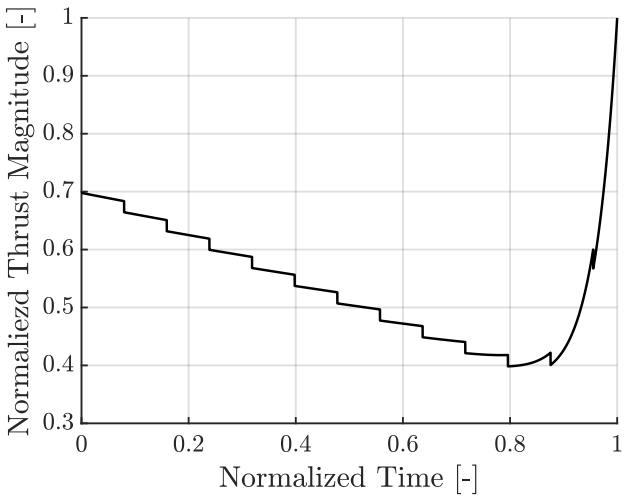


Figure 4-24: Feedforward thrust normalized by the maximum thrust of the propulsion system versus time normalized by the escape time when reduced for feasibility and using a stage-based system

factor for a stage-based minimum performance iEPS based system on a 3U CubeSat starting from geostationary orbit is 0.6978. Figure 4-24 shows the feedforward thrust normalized by the maximum thrust of the propulsion system versus time normalized by the escape time when reduced for feasibility and using a stage-based system. We can see discrete drops in required thrust every time a stage is ejected from the spacecraft due to the drop in spacecraft mass.

Figure 4-25 shows the LQR feedback controlled trajectory for escape from Earth starting from geostationary orbit with reduced reference acceleration and using a stage-based propulsion system. We can see that the true spacecraft trajectory exactly follows the analytical reference trajectory - the analytical reference trajectory is not visibly discernible. Compared to the unstaged trajectory, the escape time is reduced to 6,291 hours from the 10,040 hours when the only difference between the two propulsion systems is the staging. Figure 4-26 shows the control thrust normalized by the maximum thrust of the propulsion system for the LQR feedback controlled trajectory. We can see that the control thrust during the trajectory is higher than in the unstaged case in Figure 4-21 but at the end of the trajectory the control thrust magnitude is still equal to the maximum thrust output of the propulsion system.

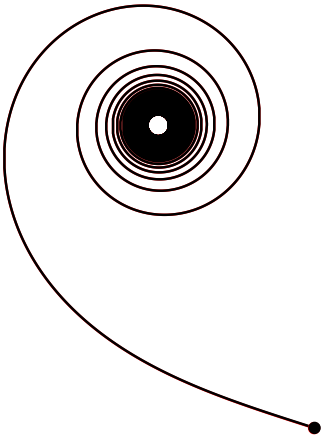

Figure 4-25: LQR feedback controlled trajectory for escape from Earth starting from geostationary orbit with reduced reference acceleration and a stage-based system

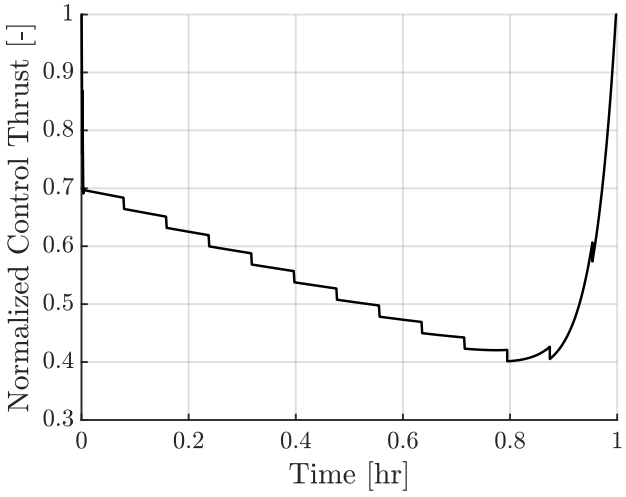


Figure 4-26: Control thrust magnitude normalized by the maximum thrust of the propulsion system for LQR feedback controlled trajectory for escape starting from geostationary orbit with reduced reference acceleration and a stage-based system

# Chapter 5

# Conclusions

Stage-based electrospray propulsion systems utilize the compactness of electrospray thrusters in order to create a high $\Delta$V propulsion system compatible with the CubeSat form factor. The lifetime limitations of electrospray thrusters, that prevented their use in a high $\Delta$V propulsion system previously, are bypassed in order to arbitrarily increase the lifetime of the propulsion system. Development of stage-based propulsion systems also has potential benefits in counteracting thruster decay, providing propulsion system redundancy, or providing new avenues for mission optimization similar to optimization of launch vehicle staging.

Mechanisms required for a stage-based propulsion system were designed, prototyped, and tested in a vacuum environment to show the mechanical feasibility of a stage-based approach. In addition, analytical analysis methods that provide tight bounds on the true solution were developed for use in preliminary mission and propulsion system design. The analysis also demonstrated that a stage-based propulsion system capable of propelling a 3U CubeSat to a near-Earth asteroid is feasible with current propulsion technology.

Analytical methodologies can also be extended to provide the framework for autonomous decision making and autonomous guidance during escape. Estimates of the mission success probability can be used to determine when to eject a stage that has suffered a partial failure in order to guarantee a specified probability of mission success. Approximations of the spacecraft dynamics during low-thrust spirals can

also be used to provide a computationally simple reference trajectory for circle-circle transfers and escape trajectories.

## 5.1 Contributions

The main contributions of this work are:

- Design of a stage-based electrospray propulsion system to enable deep-space CubeSat missions with current propulsion technology.
- Demonstration of the first stage-based electrospray propulsion system in a vacuum environment.
- Development of analytical methodologies for analysis of stage-based propulsion systems to aid in preliminary mission and propulsion system design and lay the framework for autonomous decision making.
- Analysis of analytical approximations of dynamics of low-thrust spirals combined with linear feedback control for computationally simple guidance for circle-circle transfers and escape trajectories.

## 5.2 Recommendations for Future Work

- Analysis of stage-based propulsion systems centered around different propulsion technologies such as Hall thrusters or ion engines.
- Refined mechanical design of the staging and routing mechanisms to advance the mechanisms beyond the prototype level and towards a flight ready system.
- Design of staging system that ejects only thruster heads and not fuel tanks in order to develop a system that is better suited for redundancy applications but looses potential uses in optimization.

- Random vibration testing of staging stack to verify that a stage-based propulsion system can survive the launch environment or to determine necessary modifications to improve vibration response.
- Test of beryllium-copper alloy wires or other wire materials different from stainless steel 304 as fuse wires to decrease capacitor energy required for fusing.
- Determine range of spacecraft performance metrics to analyze tradeoff between thruster lifetime and thrust to determine optimal operation point.
- Analysis of stage-based propulsion systems for optimization of mission time given a payload defined by its mass and volume and an overall limit on the spacecraft form factor.
- Simulation of spacecraft body charging and potential charging of ejected stages to ensure there are no unexpected electrostatic effects.
- Development of computationally simple trajectory design methods for trajectories beyond circle-circle transfers or escape.
- Analysis of proximity operations around an asteroid for science missions as well as trajectories of stages ejected during proximity operations to ensure no collisions between the stage and spacecraft.

# Appendix A

# Analytical Approximation for Low-Thrust Trajectories

## A.1 Motion in the Orbital Plane

Several authors present analyses to approximate low thrust transfers between two circular, coplanar orbits. Prussing and Conway [26] show an energy based argument to approximate the $\Delta$V for circle-circle transfers. The same arguments are used here to approximate the state of the spacecraft as a function of time during the transfer.

The specific energy, $\epsilon$, of an orbit is given by

$$\epsilon = \frac{1}{2}v^2 - \frac{\mu}{r} \tag{A.1}$$

Assuming that the orbit is circular then the velocity can be expressed in terms of the orbital radius as

$$v = \sqrt{\frac{\mu}{r}} \tag{A.2}$$

The specific energy can then be written only as a function of the orbital radius as

$$\epsilon = -\frac{1}{2}\frac{\mu}{r} \tag{A.3}$$

The time derivative of the specific energy, the specific power, is therefore

$$\frac{d\epsilon}{dt} = \frac{1}{2}\frac{\mu}{r^2}\frac{dr}{dt} \tag{A.4}$$

which can be related to the power input from the propulsion system

$$\frac{d\epsilon}{dt} = \vec{a}_{\mathrm{p}} \cdot \vec{v} \tag{A.5}$$

Assuming that fuel mass flow is negligible and the propulsive acceleration is aligned with the velocity of the spacecraft then

$$\frac{1}{2}\frac{\mu}{r^2}\frac{dr}{dt} = a_{\mathrm{p}}\sqrt{\frac{\mu}{r}} \tag{A.6}$$

which can be rearranged to give a differential equation for the orbital radius

$$\frac{dr}{dt} = \frac{2a_{\mathrm{p}}}{\sqrt{\mu}}r^{3/2} \tag{A.7}$$

This differential equation can be analytically integrated to give an approximation for the orbital radius as a function of time

$$r(t) = \frac{r_0}{\left(1 - \frac{a_{\mathrm{p}}}{v_0}t\right)^2} \tag{A.8}$$

where $r_0$ is the initial orbital radius and $v_0$ is the initial orbital velocity. The radial velocity is simply the derivative of the orbital radius

$$v_r(t) = \frac{dr(t)}{dt} = \frac{2r_0 a_{\mathrm{p}}/v_0}{\left(1 - \frac{a_{\mathrm{p}}}{v_0}t\right)^3} \tag{A.9}$$

The tangential velocity can be approximated through the circular orbit approximation

$$v_\theta(t) = \sqrt{\frac{\mu}{r}} = v_0\left(1 - \frac{a_{\mathrm{p}}}{v_0}t\right) \tag{A.10}$$

Lastly, the angular position can be approximated by integration

$$\theta(t) = \theta_0 + \int_0^t \frac{v_\theta}{r} dt = \theta_0 + \frac{1}{4}\frac{v_0^2}{r_0 a_\mathrm{p}} \left[ 1 - \left( 1 - \frac{a_\mathrm{p}}{v_0} t \right)^4 \right] \tag{A.11}$$

This analysis gives estimates of all four spacecraft state variables in the orbital plane during a low-thrust transfer. The equations are summarized here

$$r(t) = \frac{r_0}{\left( 1 - \frac{a_\mathrm{p}}{v_0} t \right)^2} \tag{A.12}$$

$$\theta(t) = \theta_0 + \frac{1}{4}\frac{v_0^2}{r_0 a_\mathrm{p}} \left[ 1 - \left( 1 - \frac{a_\mathrm{p}}{v_0} t \right)^4 \right] \tag{A.13}$$

$$v_r(t) = \frac{2 r_0 a_\mathrm{p} / v_0}{\left( 1 - \frac{a_\mathrm{p}}{v_0} t \right)^3} \tag{A.14}$$

$$v_\theta(t) = v_0 \left( 1 - \frac{a_\mathrm{p}}{v_0} t \right) \tag{A.15}$$

## A.2 Inclination Changes

Analytical approximations can also be developed for the inclination and right ascension of the ascending node (RAAN) to describe changes to the orbital plane. Based on the orbit geometry, the inclination, $i$, can be related to the angular momentum of the orbit through

$$\cos i = \frac{h_z}{h} \tag{A.16}$$

where $h$ is the magnitude of the angular momentum and $h_z$ is the $z$ component of the angular momentum. Taking the time derivative of both sides

$$-\sin i \frac{di}{dt} = \frac{\dot{h}_z}{h} - \frac{h_z \dot{h}}{h^2} = \frac{h\dot{h}_z - \dot{h} h_z}{h^2} \tag{A.17}$$

which can be rearranged to

$$\frac{di}{dt} = \frac{1}{\tan i}\left[\frac{\dot{h}}{h} - \frac{\dot{h}_z}{h_z}\right] \tag{A.18}$$

Assuming that the components of the propulsive acceleration applied to the spacecraft

$T$ : in the orbital plane, perpendicular to the radial vector

$N$ : perpendicular to the orbital plane

then

$$\dot{h} = rT \tag{A.19}$$

$$\dot{h}_z = rT\cos i - rN\cos\theta\sin i \tag{A.20}$$

where $r$ is the radial position and $\theta$ is the angle of the spacecraft position from RAAN. In addition, the magnitude of the angular momentum and the $z$ component of the angular momentum can be expressed in terms of orbital elements as

$$h = \left[\mu a\left(1-e^2\right)\right]^{1/2} \tag{A.21}$$

$$h_z = \left[\mu a\left(1-e^2\right)\right]^{1/2}\cos i \tag{A.22}$$

where $\mu$ is the gravitational parameter of the central body, $a$ is the semi-major axis of the orbit, and $e$ is the eccentricity of the orbit. Plugging into the inclination time derivative

$$\frac{di}{dt} = \frac{1}{\tan i}\left[\frac{rT}{\left[\mu a\left(1-e^2\right)\right]^{1/2}} - \frac{rT\cos i - rN\cos\theta\sin i}{\left[\mu a\left(1-e^2\right)\right]^{1/2}\cos i}\right] \tag{A.23}$$

which, after cancelations, can be reduced to

$$\frac{di}{dt} = \frac{r}{\left[\mu a\left(1-e^2\right)\right]^{1/2}}N\cos\theta \tag{A.24}$$

Assuming that the orbit is circular ($e = 0$, $a = r$) and the normal acceleration is applied with the profile

$$N = a_{\mathrm{N}} \cos\theta \tag{A.25}$$

then the inclination time derivative is

$$\frac{di}{dt} = \sqrt{\frac{r}{\mu}} a_{\mathrm{N}} \cos^2\theta \tag{A.26}$$

Plugging in the approximation for the radial position from Equation A.12 the inclination time derivative is

$$\frac{di}{dt} = \left[\frac{r_0}{\mu\left(1 - \frac{a_{\mathrm{p}}}{v_0}t\right)^2}\right]^{1/2} a_{\mathrm{N}} \cos^2\theta \tag{A.27}$$

which can be integrated

$$\Delta i = \int_0^t \sqrt{\frac{r_0}{\mu}} \frac{a_{\mathrm{N}}}{1 - \frac{a_{\mathrm{p}}}{v_0}t} \cos^2\theta dt \tag{A.28}$$

using a power reduction for the cosine term

$$\Delta i = \frac{1}{2}\frac{a_{\mathrm{N}}}{v_0}\int_0^t \left[\frac{1}{1 - \frac{a_{\mathrm{p}}}{v_0}t} + \frac{1}{1 - \frac{a_{\mathrm{p}}}{v_0}t}\cos 2\theta\right] dt \tag{A.29}$$

Neglecting the cosine term as we expect it to be oscillatory and average to zero then the increment in inclination is approximately

$$\Delta i \approx \frac{1}{2}\frac{a_{\mathrm{N}}}{v_0}\int_0^t \frac{1}{1 - \frac{a_{\mathrm{p}}}{v_0}t} dt = -\frac{1}{2}\frac{a_{\mathrm{N}}}{a_{\mathrm{p}}} \ln\left(1 - \frac{a_{\mathrm{p}}}{v_0}t\right)\Big|_0^t \tag{A.30}$$

which gives an analytical approximation for the inclination of the orbit over time as

$$i = \frac{1}{2}\frac{a_{\mathrm{N}}}{a_{\mathrm{p}}} \ln\left(\frac{v_0}{v_0 - a_{\mathrm{p}}t}\right) \tag{A.31}$$

# Appendix B

# Model Predictive Control Example

## B.1 Problem Formulation

For an example problem consider a triangular spacecraft in 2D free space with a goal of moving between two states in a given time with minimal control effort. Figure B-1 shows the problem with the initial state being the origin (0, 0) with a heading of 0 and the final state being the point (10, 10) also with a heading of 0. The thicker line on the spacecraft drawing represents the back of the spacecraft. We will set that the spacecraft has 60 seconds to move between the two states.

Two thrusters are mounted on the back of the spacecraft and spaced such that the combination of the two thruster can produce both a force and torque on the spacecraft. We will assume that all relevant dimensions and spacecraft properties are equal to 1 to simplify the dynamics. The dynamics are therefore

$$f = \dot{\mathbf{x}} = \begin{bmatrix} \dot{x} \\ \dot{y} \\ \dot{v}_x \\ \dot{v}_y \\ \dot{\theta} \\ \dot{\omega} \end{bmatrix} = \begin{bmatrix} v_x \\ v_y \\ (F_1 + F_2)\cos\theta \\ (F_1 + F_2)\sin\theta \\ \omega \\ F_1 - F_2 \end{bmatrix} \tag{B.1}$$

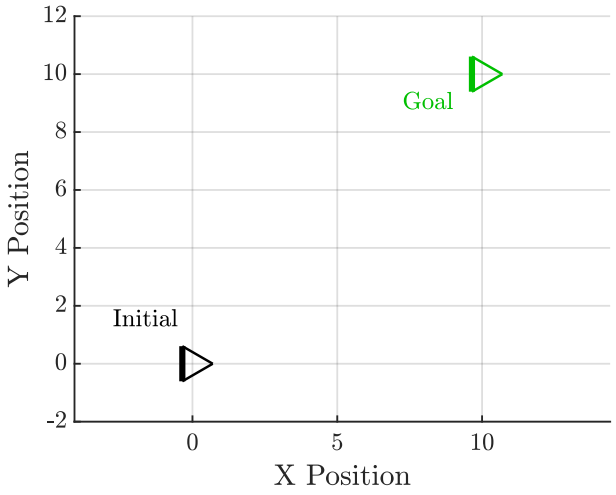


Figure B-1: Initial and goal states for spacecraft

where $x$ and $y$ are the position of the spacecraft, $v_x$ and $v_y$ are the corresponding velocities, $\theta$ is the heading, and $\omega$ is the angular velocity.

The thrusters cannot produce negative thrust nor can the spacecraft produce a pure torque. Therefore, to move from the initial state to the goal state is not as simple as pointing the spacecraft at the goal and then breaking to stop at the goal state. A more complex trajectory is required and model predictive control with direct transcription is capable of solving for it.

## B.2 Model Predictive Control Setup

Given that the goal is to minimize the total control effort, the cost function for the optimization is

$$\min_{\mathbf{x},\mathbf{u}} J = \sum_{n=0}^{N} \mathbf{u}[n]^{\mathrm{T}} \mathbf{u}[n] \tag{B.2}$$

where $\mathbf{u}$ is the control vector

$$\mathbf{u} = \begin{bmatrix} F_1 \\ F_2 \end{bmatrix} \tag{B.3}$$

and the number of discretization points, $N$, is set by the user. In this case, the total time of the trajectory is 60 seconds so picking $N = 60$ gives a time step, $dt$, of 1 second between each discretization point.

There are four constraints for this problem. The first is the dynamics constraints between each discretization point. Since the given dynamics are nonlinear and in continuous time, the discrete dynamics can be approximated with a trapezoidal integration scheme assuming a zero-order hold on the control input

$$\mathbf{x}[n+1] = \mathbf{x}[n] + \frac{1}{2}dt\left(f(\mathbf{x}[n], \mathbf{u}[n]) + f(\mathbf{x}[n+1], \mathbf{u}[n])\right) \tag{B.4}$$

where $f(\mathbf{x}, \mathbf{u})$ are the dynamics from Equation B.1. The second constraint limits the thrust of each thruster to be positive

$$\mathbf{u}[n] \geq 0 \tag{B.5}$$

The last two constraints constrain the initial and final states to the given initial and goal states

$$\mathbf{x}[0] = \mathbf{x_0} \tag{B.6}$$

$$\mathbf{x}[N] = \mathbf{x_g} \tag{B.7}$$

## B.3 Results

Given the objective function from Equation B.2 and the constraint functions from Equations B.4 through B.7 the goal of the solver is to find $\mathbf{x}[n]$ and $\mathbf{u}[n]$ for all $n \in \{0, N\}$ to minimize the objective while satisfying the constraints. Figure B-2 shows the resulting trajectory from the initial state to the goal state. We can see that the spacecraft turns around just ahead of the goal state to push itself towards the goal before turning again and braking.

Figure B-3 shows the spacecraft position and orientation as well as bars representing the thruster plumes for evenly spaced time intervals between the initial and

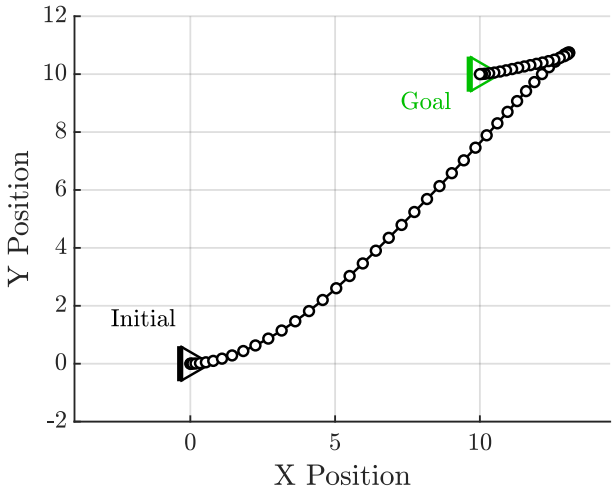


Figure B-2: Trajectory solution from model predictive control

final states. Initially, the spacecraft pushes itself towards just ahead of the the goal position and gives itself a rotation such that it can brake later on. Midway through the trajectory the spacecraft is just coasting which is to be expected for a minimum control solution. Towards the end of the trajectory, the spacecraft brakes, rotates itself back towards the goal orientation, and pushes itself towards the goal. At the very end of the trajectory the spacecraft applies one final thrust to simultaneously attenuate both its linear and angular motion and stop exactly on the goal state.

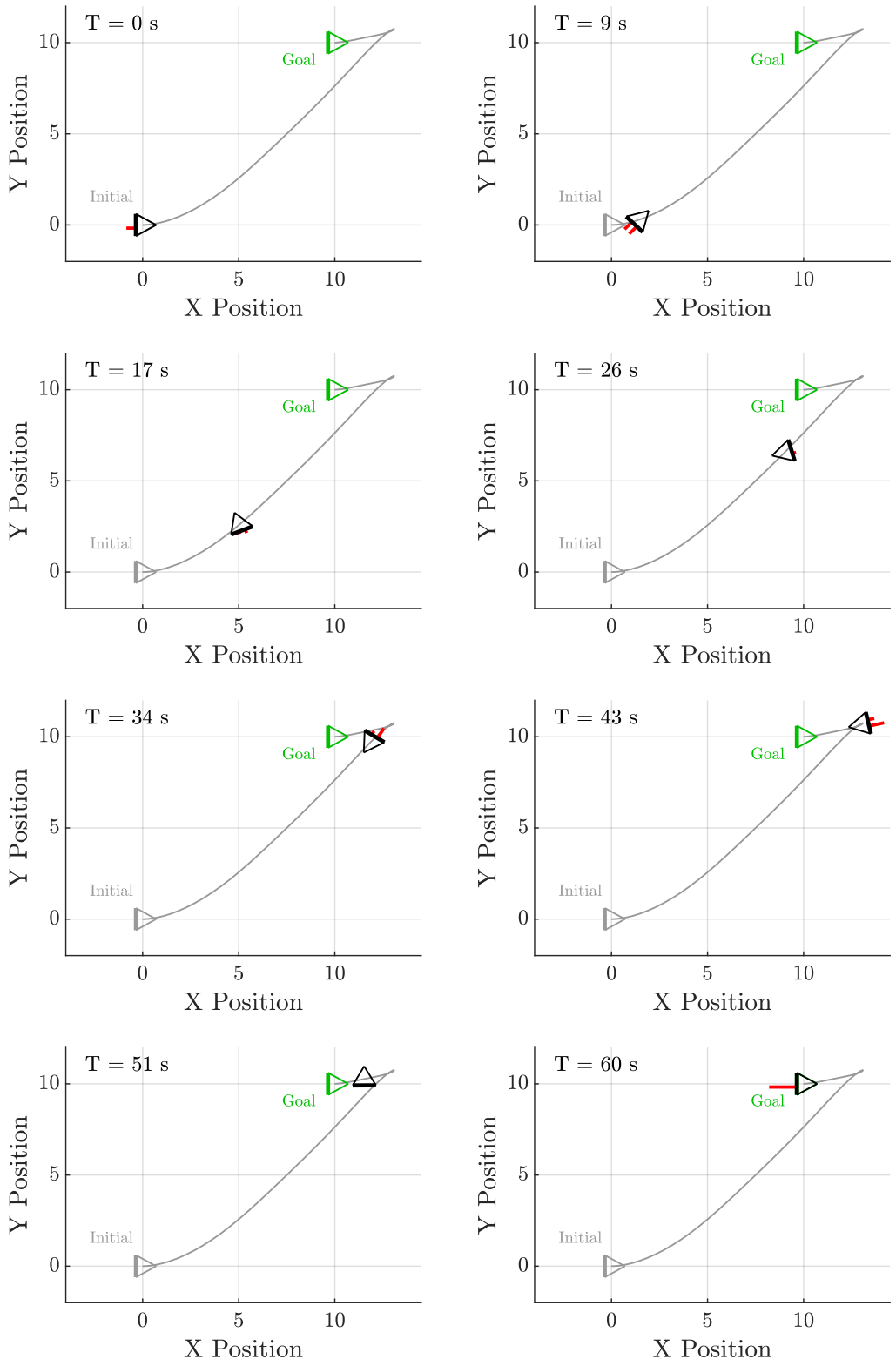


Figure B-3: Spacecraft trajectory over time with bars representing thruster plumes

# References


[1] NASA JPL. Mars Cube One (MarCO) Mission Overview. `https://www.jpl.nasa.gov/cubesat/missions/marco.php`.

[2] Chase Coffman, Manuel Martínez-Sánchez, Francisco J. Higuera, and Paulo C. Lozano. Structure of the menisci of leaky dielectric liquids during electrically-assisted evaporation of ions. *Applied Physics Letters*, 109(23), December 2016.

[3] David Krejci, Fernando Mier-Hicks, Robert Thomas, Thomas Haag, and Paulo C. Lozano. Emission Characteristics of Passively Fed Electrospray Microthrusters with Propellant Reservoirs. *Journal of Spacecraft and Rockets*, 54(2), March-April 2017.

[4] Jimmy Rojas-Herrera et al. Porous Materials for Ion-Electrospray Spacecraft Microengines. *Nanomechanics and Micromechanics*, 7(3), September 2017.

[5] Fernando Mier-Hicks and Paulo C. Lozano. Electrospray Thrusters as Precise Attitude Control Actuators for Small Satellites. *Journal of Guidance, Control, and Dynamics*, 40(3), December 2017.

[6] Marc D. Rayman et al. Dawn: A mission in development for exploration of main belt asteroids Vesta and Ceres. *Acta Astronautica*, 58(11), June 2006.

[7] Anirudh Thuppul, Peter L. Wright, and Richard E. Wirz. Lifetime Considerations and Estimation for Electrospray Thrusters. In *Proceedings of 2018 Joint Propulsion Conference*, University of California Los Angeles, Los Angeles, CA, USA, July 2018.

[8] John Ziemer et al. Colloid Microthruster Flight Performance Results from Space Technology 7 Disturbance Reduction System. In *Proceedings of the 35th International Electric Propulsion Conference*, Georgia Institute of Technology, Atlanta, GA, USA, October 2017.

[9] Peter L. Wright, Anirudh Thuppul, and Richard E. Wirz. Life-Limiting Emission Modes for Electrospray Thrusters. In *Proceedings of 2018 Joint Propulsion Conference*, University of California Los Angeles, Los Angeles, CA, USA, July 2018.

[10] David Krejci, Marco Gomez Jenkins, and Paulo C. Lozano. Staging of electric propulsion systems: Enabling an interplanetary CubeSat. *Acta Astronautica*, 160:175–182, July 2019.

[11] David Krejci and Paulo C. Lozano. Micro-machined ionic liquid electrospray thrusters for CubeSat applications. In *Proceedings of 35th International Electric Propulsion Conference*, Georgia Institute of Technology, Atlanta, GA, USA, October 2017.

[12] Adam Thurn et al. A Nichrome Burn Wire Release Mechanism for CubeSats. In *Proceedings of 41$^{st}$ Aerospace Mechanisms Symposium*, Jet Propulsion Laboratory, Pasadena, CA, USA, May 2012.

[13] Brett Huett and Cliff Willey. Design and Development of Miniature Mechanisms for Small Spacecraft. In *Proceedings of 14$^{th}$ AIAA/USU Conference on Small Satellites*, Utah State University, Logan, UT, USA, August 2000.

[14] Michael A. Patterson and Anil V. Rao. GPOPS-II: A MATLAB Software for Solving Multiple-Phase Optimal Control Problems Using hp-Adaptive Gaussian Quadrature Collocation Methods and Sparse Nonlinear Programming. *ACM Transactions on Mathematical Software (TOMS)*, 1(1), October 2014.

[15] Bruce A. Conway. *Spacecraft Trajectory Optimization*, chapter 2, pages 16–36. Cambridge Aerospace Series. Cambridge University Press, New York, New York, 1st edition, March 2014.

[16] Donald E. Kirk. *Optimal Control Theory*, section 5.1, pages 184–209. Dover Books on Electrical Engineering. Dover Publications, Mineola, New York, 1st edition, April 2004.

[17] Kalyanmoy Deb. *Multi-Objective Optimization using Evolutionary Algorithms*. Wiley, Hoboken, New Jersey, 1st edition, March 2009.

[18] Daniel G. Yárnoz, Joan-Pau Sanchez, and Colin R. McInnes. Easily Retrievable Objects among the NEO Population. *Celestial Mechanics and Dynamical Astronomy*, 116(4):367–388, April 2013.

[19] NASA JPL. JPL Small-Body Database Browser. `https://ssd.jpl.nasa.gov/sbdb.cgi`.

[20] Steven R. Chesley, Paul W. Chodas, Andrea Milani, Giovanni B. Valsecchi, and Donald K. Yeomans. Quantifying the Risk Posed by Potential Earth Impacts. *Icarus*, 159:423–432, 2002.

[21] Mauricio Guelman. Closed-Loop Control of Close Orbits Around Asteroids. *Journal of Guidance, Control, and Dynamics*, 38(5), May 2015.

[22] Anastassios E. Petropoulos and Jon A. Sims. A Review of Some Exact Solutions to the Planar Equations of Motion of a Thrusting Spacecraft. In *2nd International Symposium on Low Thrust Trajectories*.

[23] Iman Shafieenejad and Alireza B. Novinzadeh. Analytical solutions for two-point boundary value problems: Optimal low-thrust orbit transfers. *Journal of Aerospace Engineering*, 224(7), 2010.

[24] Malcolm Macdonald. Analytical, circle-to-circle low-thrust transfer trajectories with plane change. In *AIAA Guidance, Navigation, and Control Conference*, Boston, MA, August 2013.

[25] John E. Prussing and Bruce A. Conway. *Orbital Mechanics*, section 10.3, pages 182–184. Oxford University Press, New York, New York, 2nd edition, December 2012.

[26] John E. Prussing and Bruce A. Conway. *Orbital Mechanics*, section 8.4, pages 142–143. Oxford University Press, New York, New York, 2nd edition, December 2012.